FAU Studien aus der Informatik 16

Benjamin H. Groh

IMMU-based Orientation Determination in Sports Analytics

Kinematic Analysis and Performance Interpretation

FAU UNIVERSITY PRESS

Benjamin H. Groh

IMMU-based Orientation Determination in Sports Analytics

Kinematic Analysis and Performance Interpretation

FAU Studien aus der Informatik

Band 16

Benjamin H. Groh

IMMU-based Orientation Determination in Sports Analytics

Kinematic Analysis and Performance Interpretation

Erlangen
FAU University Press
2021

Bibliografische Information der Deutschen Nationalbibliothek:
Die Deutsche Nationalbibliothek verzeichnet diese Publikation in der Deutschen Nationalbibliografie; detaillierte bibliografische Daten sind im Internet über http://dnb.d-nb.de abrufbar.

Der vollständige Inhalt des Buchs ist als PDF über den OPUS-Server der Friedrich-Alexander-Universität Erlangen-Nürnberg abrufbar:
https://opus4.kobv.de/opus4-fau/home

Bitte zitieren als
Groh, Benjamin H. 2021. *IMMU-based Orientation Determination in Sports Analytics. Kinematic Analysis and Performance Interpretation*. FAU Studien aus der Informatik Band 16. Erlangen: FAU University Press. DOI: 10.25593/978-3-96147-486-8

Verlag und Auslieferung:
FAU University Press, Universitätsstraße 4, 91054 Erlangen

Druck: docupoint GmbH

ISBN: 978-3-96147-485-1 (Druckausgabe)
eISBN: 978-3-96147-486-8 (Online-Ausgabe)
ISSN: 2509-9981
DOI: 10.25593/978-3-96147-486-8

IMMU-based Orientation Determination in Sports Analytics: Kinematic Analysis and Performance Interpretation

IMMU-basierte Orientierungsbestimmung in der Sportanalytik:
Kinematische Analyse und Bewegungsinterpretation

Der Technischen Fakultät
der Friedrich-Alexander-Universität
Erlangen-Nürnberg

zur

Erlangung des Doktorgrades Dr.-Ing.

vorgelegt von

Benjamin H. Groh
aus Leimitz

Als Dissertation genehmigt
von der Technischen Fakultät
der Friedrich-Alexander-Universität Erlangen-Nürnberg

Tag der mündlichen Prüfung:	26.04.2021
Vorsitzender des Promotionsorgans:	Prof. Dr.-Ing. habil. Andreas Paul Fröba
Gutachter:	Prof. Dr. Björn Eskofier Prof. Antonis Argyros

Abstract

Sports analytics research has had major impact on the development of innovative training methods and the broadcast of sports events. Tasks that formerly required manual interference, such as counting ball contacts, evolved over semi-automatic to completely automatic measurement and analysis methods. Often incorporated hardware for these methods are wearable inertial measurement units (IMUs) and inertial-magnetic measurement units (IMMUs). IMUs and IMMUs provide accelerometer, gyroscope and potentially, magnetometer data. These data contain information that can be extracted and processed in order to establish sports-specific features. These features could for example be the current velocity, stride length, jump duration or orientation of athletes and sports-specific objects. A research field that benefits from the establishment of aforementioned features is kinematic analysis, which is focused on the investigation of observed motion. The outcome of kinematic analysis can further be processed for the interpretation of the performed motion in the context of the corresponding sports.

This thesis provides algorithms for both kinematic analysis and subsequent performance interpretation based on unobtrusively obtained measurements and corresponding features. Its main focus is set on orientation features and the exploration of their potential for sports analytics. The proposed algorithms are described and evaluated by examples in five sports: scuba diving, rowing, ski jumping, snowboarding and skateboarding.

For the first three, kinematic analysis is performed. In scuba diving, the upper body and shank angles of divers are determined with data from IMUs attached to the divers' bodies. Furthermore, the performed fin kicks are automatically detected and segmented. In rowing, a similar detection approach is developed for the segmentation of single rowing strokes with data from one IMU attached to the boat. Subsequently, the in-stroke rotation of the rowing boat is calculated. In ski jumping, an automatic velocity and jump length determination is presented with data from IMMUs attached to both skis. The calculation is based on the continuous ski orientation.

Further processing for performance interpretation is provided by the application to snowboarding and skateboarding with one IMMU attached per board. Machine learning is incorporated for the classification of performed board sports tricks. As input for the machine learning pipeline,

mainly previously established orientation features are used. In skateboarding, the performed motion is additionally visualized by means of a 3D-graphic. Furthermore, the process of automated classification and visualization of skateboard tricks is implemented in a real-time capable system, which is then presented to the board sports community. The community perception with regard to the developed system and to technology in sports in general is analyzed with a survey.
The evaluation of proposed algorithms for kinematic analysis shows that IMU data can be applied for robust segmentation of periodic motion with segmentation recall results of 84.4 % for divers' fin kicks and between 90 % and 100 % for rowing strokes. IMU data can further be processed for an accurate orientation determination with 0° mean error and between 8° and 11° standard deviation for scuba diving related angles. The angular ranges of the in-stroke rotation calculation in rowing are comparable to literature values. In the analysis in ski jumping, the ski orientation is processed for the establishment of further kinematic features. The corresponding results show a mean error and standard deviation of $-3.0\,\% \pm 4.7\,\%$ (velocity) and $0.9\,\% \pm 3.4\,\%$ (jump length) in relation to the average velocity and jump length of all measurements of this thesis. The evaluation of the classification tasks in board sports shows accuracies between 90.3 % and 93.3 % for snowboard tricks and 89.1 % for skateboard tricks. The 3D-visualization of skateboard tricks is evaluated to an error of $2.2° \pm 1.9°$. The survey results regarding the community perception indicate the interest of athletes in technology but also the resistance to replacing subjective human opinion by automated analyses or even machine-based judgment.
This work provides contributions to sports analytics by the example of five sports with the special focus on processing orientation features with data from IMUs and IMMUs. The proposed algorithms for kinematic analysis were already partially included in the broadcast of international competitions and could furthermore directly be applied for training scenarios in order to provide continuous monitoring and analyses. The classification of board sports actions shows promising results. Based on the generalized machine learning implementation, the algorithms can easily be adapted and extended to a wide variety of applications. In future work, the methods of this thesis can be transferred to sports science in order to establish thorough investigations and innovative training methods. Furthermore, the proposed algorithms could be implemented for costumer products of daily use in sports.

Zusammenfassung

Das Forschungsgebiet der Sportanalytik hat bereits großen Einfluss auf die Entwicklung innovativer Trainingsmethoden und die mediale Übertragung von Sportveranstaltungen genommen. Tätigkeiten, die früher manuell erledigt wurden, wie z.B. das Zählen von Ballkontakten, entwickelten sich über halbautomatische, zu vollautomatischen Mess- und Analysemethoden. Oftmals werden dazu tragbare inertiale Messeinheiten (IMUs; englisch: 'inertial measurement units') und inertial-magnetische Messeinheiten (IMMUs; englisch: 'inertial-magnetic measurement units') eingesetzt. IMUs und IMMUs stellen Akzelerometer- und Gyroskopdaten, sowie ggf. Magnetometerdaten zur Verfügung. Diese Daten beinhalten Informationen, die extrahiert und zu sportspezifischen Merkmalen verarbeitet werden können. Solche Merkmale sind beispielsweise die aktuelle Geschwindigkeit, Schrittlänge, Sprungweite oder die Orientierung eines Athleten und zugehöriger Sportgeräte. Die Bestimmung dieser Merkmale ist Teil von kinematischen Analysen, welche sich mit der Untersuchung von Bewegungen befassen. Die Ergebnisse dieser Analysen können dazu genutzt werden, beobachtete Bewegungen im spezifischen Zusammenhang zur jeweiligen Sportart zu interpretieren.
In dieser Dissertation werden Algorithmen für kinematische Analysen und weiterführende Interpretationen der ausgeführten Bewegungen vorgestellt. Diese Algorithmen basieren auf Daten dezenter Messmethoden und zugehörigen Merkmalen. Der Schwerpunkt dieser Arbeit liegt auf Merkmalen, die die Orientierung betreffen und darauf, deren Potential für die Sportanalytik zu erforschen. Die vorgestellten Algorithmen werden anhand von fünf Sportarten beschrieben und evaluiert: Gerätetauchen, Rudern, Skispringen, Snowboarden und Skateboarden.
Die Durchführung kinematischer Analysen bezieht sich auf die ersten drei dieser Sportarten. Im Gerätetauchen werden die Winkelstellungen des Oberkörpers und der Unterschenkel anhand von Messungen mit IMUs am Körper von Tauchern bestimmt. Zusätzlich wird die Flossenschlagbewegung automatisiert detektiert und in einzelne Schläge segmentiert. Im Rudern wird ein ähnlicher Ansatz verfolgt, um einzelne Ruderschläge mit Daten einer am Boot angebrachten IMU zu detektieren. Anschließend wird die Bootrotation innerhalb einzelner Ruderschlagzyklen berechnet. Für die Analyse im Skispringen werden Algorithmen zur automatisierten Berechnung der Geschwindigkeit und der Sprungweite vorgestellt, die Daten von an beiden Skiern angebrachten

IMMUs verarbeiten. Die Berechnung basiert auf der kontinuierlich bestimmten Skiorientierung.
Die Bewegungsinterpretation auf Basis von kinematischen Merkmalen wird durch die Anwendung im Snowboarden und Skateboarden verdeutlicht. In beiden Sportarten werden Daten von einer am Board angebrachten IMU prozessiert. Mit Hilfe von maschinellem Lernen werden Boardsporttricks klassifiziert. Dazu werden vorwiegend zuvor berechnete Orientierungsmerkmale verwendet. Beim Einsatz im Skateboarden wird die ausgeführte Bewegung zusätzlich durch eine 3D-Animation dargestellt. Weiterhin werden die vorgestellten Algorithmen zur automatischen Trickklassifizierung und -visualisierung in ein Echtzeitsystem implementiert, welches anschließend in der Boardsportszene präsentiert wird. Die Einschätzungen der Sportler bezüglich des entwickelten Systems und des Einsatzes von Technologie im Sport im Allgemeinen wird durch eine Umfrage analysiert.
Die Evaluierung der vorgestellten Algorithmen der kinematischen Analyse zeigt, dass IMU-Daten erfolgreich für eine robuste Segmentierung von zyklischen Bewegungen genutzt werden können. Die Sensitivität für die Segmentierung von Flossenschlägen im Gerätetauchen beträgt 84.4 % und für die Segmentierung von Ruderschlägen zwischen 90 % und 100 %. Die Berechnung der Körperwinkel im Gerätetauchen wird zu einem Mittelwertfehler von 0° mit einer Standardabweichung von zwischen 8° und 11° evaluiert. Die berechnete Bootrotation innerhalb einzelner Ruderschlagzyklen führt zu Ergebnissen, die mit bisher bekannten Werten aus der Fachliteratur vergleichbar sind. Für die Anwendung im Skispringen werden Orientierungsmerkmale verwendet, um weitere kinematische Merkmale zu bestimmen. Die entsprechende Evaluierung führt zu Mittelwertfehlern und zugehörigen Standardabweichungen von $-3.0\,\% \pm 4.7\,\%$ (Geschwindigkeit) und $0.9\,\% \pm 3.4\,\%$ (Sprungweite), bezogen auf die mittlere Geschwindigkeit bzw. Sprungweite aller Messungen dieser Arbeit. Die Evaluierung der Klassifizierung von Boardsportaktionen zeigt Genauigkeiten zwischen 90.3 % und 93.3 % für Snowboardtricks und 89.1 % für Skateboardtricks. Die 3D-Visualisierung von Skateboardtricks wird mit einem Fehler von $2.2° \pm 1.9°$ evaluiert. Die Auswertung der Umfrage in der Boardsportszene zeigt das Interesse der Sportler am Einsatz von Technologie. Jedoch wird auch die Skepsis darüber deutlich, die subjektive, menschliche Einschätzung durch automatisierte Analysen oder sogar durch maschinelle Wertungsrichter zu ersetzen.
Diese Dissertation beinhaltet Beiträge zur Sportanalytik am Beispiel von fünf Sportarten und dem Schwerpunkt auf Orientierungsmerkmalen mit

Daten von IMUs und IMMUs. Die vorgestellten Algorithmen für kinematische Analyse wurden zum Teil bereits für die Fernsehübertragung von internationalen Wettkämpfen eingesetzt und könnten weiterhin auch direkt im Training verwendet werden, um kontinuierliche Messungen und Analysen zu ermöglichen. Die Klassifikation von Boardsportaktionen zeigt vielversprechende Ergebnisse. Aufgrund der generalisierten Implementierung durch maschinelles Lernen können die Algorithmen ohne großen Aufwand für eine Vielzahl von Anwendungen angepasst und erweitert werden. Die Methoden dieser Arbeit können zukünftig für sportwissenschaftliche Forschung verwendet werden, um tiefgehende sportbezogene Analysen und innovative Trainingsmethoden zu entwickeln. Weiterhin könnten die vorgestellten Algorithmen für alltäglich genutzte Produkte im Sportbereich eingesetzt werden.

Danksagung

Zunächst bedanke ich mich bei meinem Betreuer Björn Eskofier, der meine Promotion überhaupt erst möglich machte. Mein Dank richtet sich vor allem auch an alle Kolleginnen und Kollegen der ehemaligen Digital Sports Group beziehungsweise des heutigen MaD Labs und des LME, mit denen in vielen privaten und beruflichen Gesprächen interessante Forschungsideen entstanden sind. Egal, ob privat oder im Büro: Es war eine sehr geile Zeit mit euch! Besonders bedanken möchte ich mich bei Markus Streicher und Thomas Kautz. Beide unterstützten mich nicht nur bei der Anfertigung dieser Dissertation, sondern standen mir auch schon während der vorherigen Jahre meiner Promotion mit Rat und Tat zur Seite, sei es zum fachlichen Austausch, zum seelischen Support oder beim freundschaftlichen Bierkrug- und Hantelstemmen.
Weiterhin möchte ich mich bei allen von mir betreuten Studenten bedanken. Nur durch ihren ausgezeichneten Einsatz war es mir möglich, meine Promotion vielseitig zu gestalten und unterschiedliche Ideen in mehreren Sportarten zu verfolgen. Zudem bedanke ich mich bei allen Sportlern, die bereitwillig und mit viel Engagement an den durchgeführten Studien teilgenommen haben: den Tauchern von Action Sport Erlangen, den Ruderern der Rudergesellschaft Ghibellinia Waiblingen, den Skispringern und Trainern des Skiverbandes Sachsen, den Snowboardern und Trainern von Snowboard Germany und allen teilnehmenden Skateboardern aus Erlangen, Bayreuth und Leipzig sowie dem Skateshop Bretterbude in Erlangen.
Ich danke auch allen meinen Freunden, die mir in den letzten Jahren viel Geduld und Verständnis entgegen brachten und mich immer wieder motiviert haben. Mein größter Dank gilt jedoch meiner Familie: meinen Eltern Beatrix und Dieter, die mich durch ihre uneingeschränkte Unterstützung zu dem Menschen gemacht haben, der ich heute bin, meiner Schwester Stefanie, die mir immer und überall liebevoll zur Seite steht, meiner tollen Oma, meinen Paten und allen Anderen, die immer für mich da sind.

Benjamin H. Groh

Contents

List of Abbreviations

Abbreviation	Description
CV	cross-validation
DTW	dynamic time warping
GPS	global positioning system
GUI	graphical user interface
HHMM	hierarchical hidden Markov model
HMM	hidden Markov model
IMMU	inertial-magnetic measurement unit
IMU	inertial measurement unit
kNN	k-nearest neighbor
LOSO-CV	leave-one-subject-out cross-validation
LSVM	linear support vector machine
MEMS	micro electro-mechanical system
NB	naïve Bayes
RB-SVM	radial-basis kernel support vector machine
RF	random forest
RMSE	root-mean-square error
RTC	real-time clock
subDTW	subsequent dynamic time warping
SVD	singular value decomposition
SVM	support vector machine
ZVU	zero velocity update

Glossary

air trick Skateboard/snowboard term: jumping over a kicker or ramp, including *air time*.

air time General term: the time spent in the air during a jump.

catch Rowing term: placing of the blade in the water to prepare for the *drive phase*.

coxed Rowing term: boat class category; crew includes a coxswain who steers the boat; usually in four coxed (4+) and eight coxed (8+).

drive phase Rowing term: the boat is accelerated by the athlete.

goofy stance Skateboard/snowboard term: leading with the right foot in movement direction; opposite of *regular stance*.

grind trick Skateboard/snowboard term: sliding on an obstacle (often: box or rail).

heat Rowing term: qualifying race.

regular stance Skateboard/snowboard term: leading with the left foot in movement direction; opposite of *goofy stance*.

repechage Rowing term: second qualifying *heat*; alternative chance to proceed to the final.

sculling Rowing term: boat class category; rowing with two oars per athlete, one in each hand; opposite of *sweep*.

skate deck Skateboard term: one of the main components of a skateboard; flat board that the skateboarder stands on.

stance direction Skateboard/snowboard term: *regular stance*-riding athletes lead with the left foot in movement direction, *goofy stance*-riding athletes lead with the right foot.

sweep Rowing term: boat class category; rowing with one oar per athlete, held with both hands; opposite of *sculling*.

List of Figures

List of Tables

Part I

Research Background

The first part of this thesis contains the research background. In Chapter 1, the topic of sports analytics is motivated and the scope and the contributions of this work are presented with regard to state-of-the-art literature. In Chapter 2, the research background is completed by an overview of the scientific fundamentals for this thesis.

1 Introduction

This chapter introduces the topic of sports analytics with special focus on the measurement and processing of kinematic data. After the motivation of the topic, the scope of this thesis is presented, followed by an overview of the related state-of-the-art literature. Furthermore, this chapter states the contributions that are elaborated in this thesis.

1.1 Sports analytics with kinematic data

1.1.1 Motivation

The field of sports analytics has been a research area for more than 100 years [1, 2]. It covers a wide range of topics, reaching from directly visible facts (e.g., counting ball contacts during a match) and strategical game analysis (e.g., in baseball [3, 4] and football [5]) to injury prediction and prevention (e.g., in football [6] and soccer [7]). The literature shows that research topics often are focused on similar outcomes but improve in quality based on the available techniques at the time [2]. One example for this is given by the serve analysis in tennis. This has been a research topic for over 30 years but the quality of recording and evaluation tools has increased over time [8, 9, 10, 11, 12, 13].
State-of-the-art sports analytics has an impact on three major fields: professional sports, (sports) economy and (sports) science [2]. In professional sports, scouts, coaches and athletes make use of sports analytics to identify talents [14] and to improve training efficiency while decreasing the risk of injuries [15, 16, 17]. In sports economy, the broadcast of events has major influence on economical success [18]. More attractive ways of visualizing a match or an athlete's performance to spectators can lead to more enthusiasm and higher ratings [19, 20]. Sports science, leading to new insight in biomechanics, tactics and training theory, often depends on sophisticated analysis methods [21, 22].

1.1.2 Measurement methods

Various methods for the establishment of sports analytics have been implemented over the past decades and are still used nowadays. These can be divided into manual, semi-automated and automated measurement methods [2]. Manual methods would be as simple as manually

counting and analyzing ball contacts, *air time* of athletic jumps or the type of performance. Semi-automated methods describe systems that automatically collect data but still require a (technical) operator. One example is given by the jump length measurement in ski jumping competitions, where a camera operator processes video data for providing the jump length to judges and television broadcast. In contrast, automated measurement methods do not require any operator interaction and thus, provide objective results under low maintenance effort. Common automated measurement methods contain machine-based video analysis [23, 24], positioning systems (e.g., global navigation satellite system (GNSS) [25, 26, 27] or local positioning system (LPS) [28, 29, 30]) and wearable sensors [31, 32, 33].

Wearable sensors (also referred to as 'wearables') benefit from the continuous miniaturization and improvement of electronic components. They are directly attached to the athletes' bodies or integrated unobtrusively in sports equipment and clothes, which made wearable technology the most influencing fitness trend of 2016 [34]. An unobtrusive attachment or integration can be crucial for obtaining relevant data without any distraction of the athlete or interference with a competition. The advantage of wearables furthermore lies in the on-site measurement [35], even in situations when the direct line of sight to single athletes is restricted (e.g., during tackles or scrums in a rugby match [36]). Wearables in sports applications often contain inertial and magnetic sensors. Devices that only include inertial sensors (accelerometer and gyroscope) are referred to as 'inertial measurement units' (IMUs) and devices with an additional magnetometer are referred to as 'inertial-magnetic measurement units' (IMMUs), respectively. A typical use case for their application in sports is the estimation of kinematic data.

"Kinematics is the study of the geometric and time-dependent aspects of motion without analyzing the forces causing the motion" [37]. Kinematic data (in sports) are represented by various features. These kinematic features can be a body's or in general, an object's position, velocity or acceleration over time and the object's pose provided by its rotation and orientation. The orientation describes the current 3D-spatial direction in a locally or globally defined coordinate system (e.g., the geographic coordinate system earth-centered, earth-fixed (ECEF) [38]). The rotation describes the 3D-change of orientation between two states. For the sake of simplicity, the term 'orientation features' denotes both orientation and rotation features in the context of this work.

1.1.3 Processing pipeline

The traditional processing pipeline for the establishment and interpretation of kinematic features from IMU and IMMU raw measurements contains three steps: raw data preprocessing, kinematic analysis by extracting relevant features and finally, the interpretation of extracted features.

Preprocessing

During the preprocessing, the raw measurements are improved regarding their quality and if applicable, reduced in size to allow for a faster processing [39]. Typical procedures are for example raw data calibration [40], removal of data from nonessential sensor components or time intervals and data standardization for automated processing.

Kinematic analysis

From the preprocessed data, several features can be computed. In the case of kinematic analysis, these can be as simple as a velocity estimate based on acceleration integration or a rotation estimate obtained by angular rate integration. A more advanced or possibly more accurate kinematic feature extraction can include a data fusion of sensor components (e.g., orientation estimation based on accelerometer, gyroscope and magnetometer data [41]) or multiple sensor units. The data fusion can further be supported by prior knowledge of the performed motion [42].

Interpretation of kinematic features

Further processing allows for setting the extracted kinematic features into specific sports context. In certain scenarios, for example in a soccer match, the position and velocity of one single player would not reveal relevant information. However, seeing the player's position and velocity in relation to all other players in the field could lead to interesting insight in the player's intention, fitness or overall performance. Moreover, kinematic features can be processed by machine learning algorithms in order to automatically interpret the current performance of an athlete to a greater extent [43]. Sports- or action-specific models are trained with previously obtained, known data (so-called 'training data'). Based on these models, new data of the current performance can be processed in order to classify or rate them in relation to the incorporated training data.

1.2 Scope of this thesis

This thesis addresses several key aspects regarding the establishment of analysis methods for the extraction of kinematic features from IMU and IMMU raw data. The proposed methods are presented by sports applications in scuba diving, rowing and ski jumping. The scuba diving application aims on the analysis of the divers' fin kick motion and the orientation calculation of the divers' upper bodies and shanks. In the rowing application, consecutive rowing strokes are segmented and the corresponding in-stroke boat rotation is calculated. In ski jumping, the focus is set on the estimation of the ski orientation and its processing for an automated velocity and jump length calculation.
Furthermore, extracted features are processed for performance interpretation by applying machine learning algorithms for sports-specific motion classification. Example applications for the performance interpretation are proposed for snowboarding and skateboarding. For both, extracted features are processed with machine learning methods with the aim of detecting and classifying multiple snowboard and skateboard tricks. The application for skateboarding additionally covers the visualization of performed tricks and the establishment of a real-time capable system.
The consistent component in all five sports applications is the focus on orientation features, i.e., the orientation or rotation of athletes' bodies or sports-related objects. Orientation features are incorporated for both the kinematic analysis and the performance interpretation. For all applications, the requirement of unobtrusiveness is defined. Only unobtrusive measurement and analysis methods can further be used beyond the described study environment and be applied to real-world scenarios.

1.3 State of the art

This literature review provides a general state-of-the-art overview of kinematic analysis and the interpretation of kinematic data for sports and related fields. Furthermore, the sports-specific state of the art regarding the proposed applications of this thesis is elaborated.

1.3.1 Kinematic analysis

In the field of kinematic analysis for sports, Adesida et al. [35] provided a state-of-the-art literature overview with the focus on wearable tech-

nology for kinematics and kinetics applications. They concluded that there is an increased interest in wearable sensor research regarding the analysis of movement and skill levels in sports. However, they also clarified that most applications are not in a state of general usage. Chambers et al. [33] provided their findings on the impact of wearable sensors on sports motion analysis. Their systematic literature review contains publications on motion analysis in the fields of individual, team, water and snow sports. Wagner [44] published an article describing the principles for inertial sensor-based motion analysis and the role of inertial sensors in nowadays sports applications. Often investigated topics are general physical activity [45], gait and running [46], skiing [47, 48] and ski jumping [49, 50]. Besides direct calculation of kinematic features (e.g., knee angle calculation with one sensor attached to the body), the literature also contains indirect extraction methods requiring more complex processing methods. An example of this indirect calculation was published by Blank et al. [51], who proposed a table tennis ball speed and spin estimation with inertial data from a sensor attached to the racket. In addition to the wide application field of IMU- and IMMU-based kinematic analysis, wearable sensors were also applied in long-term kinematic monitoring [52] and in different environments, such as on and under water [53, 54] and in remote areas [55, 56].

1.3.2 Interpretation of kinematic data

The literature furthermore covers the processing of kinematic features for deeper interpretation in various applications. A systematic review of current trends in kinematic feature establishment and sports performance evaluation was provided by Camomilla et al. [31]. The review contains an overview of sensor-derived features and their processing for performance interpretation. There are multiple publications that directly derive performance interpretation from kinematic features. Struzik et al. [57] analyzed the effect of the orientation of ankle, knee and hip joints on the running time of sprints. McGinnis et al. [58] detected fatigue symptoms in jump performances by processing kinematic features. Seuter et al. [59] proposed a real-time feedback for daily exercises based on a 3D-visualization of the lower limb orientation. A more generalized overview of sensor-based performance monitoring was published by Sattar el al. [60]. The authors described the basic concept of the processing chain from data acquisition to filtering and interpretation. They additionally provided related publications from state-of-the-art literature.

In the field of machine learning, Cust et al. [43] published a systematic review on the automated recognition of sports-specific movements. The review provides an overview of the field of supervised machine learning with additional consideration of the comparison between IMMU and visual data, data fusion approaches and the perspective of deep learning and unsupervised learning. Further application fields for the processing of kinematic features are machine-based judgment support (e.g., the detection of illegal race walking [61]) and machine-based broadcast support (e.g., highlighting relevant scenes in soccer [62]).

1.3.3 Sports-specific applications

Scuba diving

In the literature, the majority of wearable sensor-based underwater studies focused on the performance analysis in swimming. Due to the similarity of kinematic research in swimming and scuba diving, this state-of-the-art review contains both a general overview of wearable sensor applications in swimming and more specifically, publications on kinematic analysis with the focus on orientation estimation in scuba diving. Magalhães et al. [63] and Mooney et al. [64] published detailed review articles on wearable sensor-based swimming motion analysis and elite swimming performance analysis. Guignard et al. [65] provided an overview of IMU-assessable dynamical parameters in swimming. They further described the processing chain for an appropriate underwater application on wearable devices. Mangia et al. [54] published their findings on the use of IMMUs in underwater environments and their potential for clinical and sports applications.In various studies, an IMU-based orientation calculation was part of the processing chain. The goals reached from a classification of swimming styles and patterns [66] to the tracking of the athlete's kinematics [67, 68] to a swimming phase detection [69, 70, 71]. Furthermore, the research group of Fantozzi performed an evaluation of upper body angle determination with simulated dry-land swimming scenarios [72, 73]. Although these studies all included a body angle determination, most of them focused on the processing of obtained angles for further analysis and hence, no evaluation of the angular accuracy was performed. The analyses of Magalhães et al. [73] and Fantozzi et al. [72] contained extended evaluations but were performed in a simulated instead of an underwater environment and only focused on the upper body.

Regarding kinematic analysis in scuba diving, only few approaches were published. Samimy et al. [74] analyzed scuba divers' fin swimming technique including video measurements of several body angles. However, the body angle measurements were not evaluated. Another video-based system was proposed by Steinberg et al. [75]. They developed a training system to determine the diver's performance considering swimming technique and equipment configuration. Walker and Anderson [76] analyzed the leg joint angles of the pilot of a human-powered submarine by attaching dielectric elastomer sensors to the wetsuit of the pilot. The only IMU-based investigations were published by Kuch et al. [77] and Goodfellow et al. [78]. Kuch et al. computed the diver's body orientation with one IMU attached to the air tank with the purpose of establishing an underwater navigation framework. Goodfellow et al. presented a prototype for a 3D-body angle determination with the main goal of a representative visualization of the diver's posture. They successfully tested the developed system under water but did not evaluate its accuracy.

Rowing

There is a multitude of publications regarding the analysis of rowing technique. Soper and Hume [79] provided a literature review on rowing technique from a biomechanical point of view. Smith and Loschner [80] analyzed criteria for success in competitions, mostly regarding the influence of applied forces to the boat velocity. Based on their findings, they proposed a real-time feedback system for athletes. Furthermore, they investigated asymmetric motion behavior based on applied forces [81]. They stated that this asymmetry is partially aimed on maintaining an efficient boat orientation during rowing strokes. McGregor et al. [82] published a comparison of rowing technique at different stroke rates with the focus on applied forces and body rotations. Based on these findings, Buckeridge et al. [83] stated that minor changes in rowing technique can influence the force production and required asymmetries. Kleshnev [84] analyzed the boat acceleration pattern and the temporal structure of the rowing cycle. Tessendorf et al. [85] proposed an unobtrusive detection of performed rowing stroke cycles and a corresponding calculation of the stroke rate with IMU data. The computation required data of two IMU devices, one attached to the boat and one to the oar.
Regarding kinematic analysis in particular, several methods for the orientation determination (during stroke cycles) were published for the athletes' body rotation [86, 87], the oar rotation [88, 89] and both com-

bined [90]. Although the importance of the determination of the boat rotation is known (e.g., for analyzing the motion asymmetry [81] and for the boat's stability in order to reduce the athletes' motion effort [91, 92]), only a few studies focused on its measurement and analysis. Wagner et al. [93] stated the necessity of angular measurements of rowing boats for the evaluation of the stability of the motion. Furthermore, they proposed the application of gyroscopes. However, in the study of 1993, the weight of the available gyroscope hardware was specified with 1 kg and the measurement resolution was considerable low compared to state-of-the-art hardware. In 2000, Loschner et al. [94] conducted a similar experiment and determined the 3D-rotation of single *scull* boats. Later on, Gravenhorst et al. [91] proposed the first known gyroscope data processing with lightweight sensor hardware mounted inside the boat. They determined the angular velocity for the pitch motion but did not present corresponding angles. Serveto et al. [90] established a 3D-model of the boat-oar-rower system and compared the calculated pitch angle of the boat to measurements with accelerometers.

Ski jumping

The field of wearable sensor analysis in ski jumping was widely covered by Chardonnens et al., whose research covered topics reaching from the orientation calculation of body segment to the segmentation of jump phases and the determination of applied forces. In [95], they focused on the stable flight phase and analyzed body segment orientations and aerodynamic forces in relation to the achieved jump length. An approach for jump phase segmentation was proposed in [96]. It was based on sensor data from IMUs attached to both body and skis and evaluated against a camera-based motion capture system. In [50], they presented their method for IMU-based orientation calculation of the skis and lower body segments. In contrast to previous work, they incorporated biomechanical constraints to reduce drift effects. In a follow-up work, another accuracy influencing factor was addressed: the erroneous alignment during sensor attachment [97]. Furthermore, they determined ski jumping dynamics during take-off and stable flight, compared them with literature values and analyzed the results against the achieved jump length.
Similar research was published by Bächlin et al. [98]. They estimated applied forces during the jump and the flight time based on acceleration sensors. Furthermore, Logar and Munih [99] determined both jump kinematics and dynamics and determined the ground reaction force during

inrun and take-off. Fang et al. [100] proposed an IMMU-based attitude estimation of skis with the focus on the processing of uncalibrated measurements. They applied their approach to both simulated and real ski jumping data.
A different aspect was analyzed by Brock et al., who aimed towards an automated motion evaluation system. First, they established an algorithm for IMMU-based determination of body orientation, joint position and angles [49]. They also included magnetometer measurements in their work and presented a compensation method for magnetic disturbances. Subsequently, they incorporated machine learning algorithms to classify jump performances for an automated scoring system in [101]. In a follow-up work [102], they extended the feature vector of their classification by additional kinematic features.

Snowboarding

The literature contains several publications on snowboard motion analysis. Harding et al. [103] determined the *air time* during half-pipe tricks and calculated the rotation during the *air time* by gyroscope signal integration. Their algorithm could classify recorded tricks into four rotation ranges. Furthermore, they analyzed the possible impact of an automated classification system for competition and training scenarios and the corresponding community perception [104]. Spelmezan et al. [105, 106] developed a feedback system for snowboard beginners, which contained force-sensitive resistors and inertial sensors. Its aim was to determine and analyze the athlete's weight distribution and body posture (e.g., bending of knees). A similar approach was published by Holleczek et al. [107]. They processed accelerometer and pressure sensor data to distinguish between simple riding modes (e.g., frontside, backside). They extended their prototype by a turn detection and an action detection (i.e., detection if the athlete is active or inactive) based on global positioning system (GPS) and IMU data [108]. Their evaluation resulted in accuracies of up to 88.6 % for turn detection and up to 88.2 % (with GPS: 90.5 %) for action detection. They furthermore proposed the integration of textile pressure sensors [109]. Krüger et al. [110, 111] combined a full-body IMU system with insole measurements in order to analyze biomechanical aspects of freestyle snowboarding. Lee et al. [112] published an algorithm for automated jump detection in skiing and snowboarding with a combination of IMU and barometric sensor data. Moeyersons et al. [113] developed a biofeedback device based on four pressure sensors in the snowboard

boots. The system provided vibrational and optical feedback to beginners if turns were performed with incorrect weight shift.

Skateboarding

The literature shows the research interest in skateboard motion analysis. Anlauff et al. [114] proposed the first known real-time capable prototype of a skateboard trick classification. The prototype ran on a smartphone and could distinguish between two different tricks with an accuracy of more than 90 %. An extension of their basic classification approach was published by Reynell and Thinyane [115]. They included a GPS sensor and a map visualization with the board's position and current motion based on accelerometer data. Pijnappel and Mueller [116] developed another visualization method. They presented the skateboard's trajectory using infrared emitters on the board with a corresponding infrared-sensitive camera. They furthermore conducted a survey amongst skateboarders to gather insight on the community perception about key features for trick representation. Another trick representation was introduced by Ghosh et al. [117]. They proposed MusiSkate, their prototype for audio feedback to performed skateboard actions. In addition, Park et al. [118] provided feedback on the pressure distribution of the board's surface. They attached a pressure sensor matrix beneath the grip tape and used it to measure and visualize the pressure distribution during skateboard rides. Corrêa et al. [119] presented a trick classification algorithm with an artificial neural network. They generated a large number of artificial acceleration data of skateboard tricks and classified them into five trick classes with an accuracy of up to 98.7 %. Abdullah et al. [120] proposed an approach for the classification of five tricks. They used IMU data of one athlete and evaluated multiple classifiers, leading to accuracies of up to 95.0 %.

1.4 Contributions

The literature review revealed that kinematic analysis and further processing of kinematic features for performance interpretation were proposed in a variety of sports for various application fields. Although orientation features were partially included in related publications, their importance and potential was not fully explored for both the kinematic analysis and the performance interpretation. The aim of this thesis is to combine the extraction of kinematic features and the subsequent interpretation in the

field of sports with the focus on orientation features. Suitable methods for these tasks are introduced and demonstrated by the application to five sports. For each application, sports-specific contributions are achieved. An overview of the most relevant contributions is given in the following paragraphs.

Scuba diving: Fin kick and body pose analysis

Kinematic analysis in scuba diving is often restricted to areas that can be visually observed. This limitation can be overcome by including wearables. Despite the manifold research interest in wearable technology, there is no known publication that established and evaluated a wearable sensor-based orientation calculation with respect to the required accuracy for analyzing underwater kinematics. In this thesis, methods for kinematic analysis in scuba diving are proposed. Multiple IMUs are attached to the bodies of divers. In an underwater environment, the motion of the divers is monitored by a fin kick detection algorithm. The corresponding shank orientation during fin kicks and several body poses are calculated based on IMU data and evaluated with an underwater camera system. The proposed methods can be incorporated into sports science research for optimizing the fin swimming and scuba diving motion. The described content and corresponding findings were published in [P1].

Rowing: Stroke detection and in-stroke boat rotation determination

The in-stroke boat rotation in rowing has significant impact on the velocity and the overall rowing performance. However, state-of-the-art analysis methods mostly rely on visual assessment and semi-automated rotation estimation that do not allow for a continuous analysis during training or competition. In the literature, there is no approach for the combination of an automated stroke detection and the subsequent analysis of the boat rotation, which would be necessary for a continuous in-stroke rotation calculation. In this thesis, automated methods for kinematic analysis of the in-stroke boat rotation are proposed. Two aspects are covered: an automated detection of performed rowing strokes and the determination of the in-stroke rotation of the rowing boat. Based on the attachment of one IMU per boat, measurements are obtained for both professional and amateur rowing scenarios. Rowing strokes are detected automatically with a stroke segmentation algorithm. The stroke timing is then applied to extract the rowing boat rotation during single strokes. The resulting in-

stroke rotation angles are evaluated against known literature values. The proposed methods can be applied to support training scenarios and competition broadcast. The described content and corresponding findings were published in [P2] and [P3].

Ski jumping: Ski orientation calculation with further processing for velocity and jump length determination

Ski jumping kinematics is traditionally determined with manual or semi-automated visual measurement methods. Although the advancing development of wearable systems provides possibilities for automated analyses, the application to ski jumping training and competitions remains challenging. In order not to distract the athletes, unobtrusive measurement methods without any interference with the jump procedure are required. In state-of-the-art publications, there are approaches for estimating ski jumping kinematics with inertial- and inertial-magnetic sensors. However, most of them either focused on biomechanical research or on feedback systems and thereby require full body measurements. These cannot be incorporated in standard training sessions and competitions without limitations or even disturbances of the athletes' routine. In this thesis, automated kinematic analysis methods are proposed. Measurements are unobtrusively obtained from IMMUs that are only attached to the athletes' skis. An automated jump phase segmentation is introduced and incorporated into the calculation of the ski orientation in all phases. The ski orientation is further processed in order to determine the continuous ski velocity and jump length. The jump phase segmentation and the calculation of the velocity and jump length are evaluated against multiple ground truth systems. The proposed algorithms were partially incorporated for broadcast of competitions and are furthermore capable of supporting training scenarios in an unobtrusive and affordable way. The described content and corresponding findings were published in [P4] and [P5].

Snowboarding: Slopestyle trick classification

In standard snowboard training sessions, the performance of athletes is monitored directly by a coach or is video recorded for manual analysis. Employing wearables could simplify the performance analysis and potentially improve the training quality for amateur and professional athletes. An automated wearable system could furthermore be incorporated into the broadcast of snowboard events. The literature covers wearable sensor-

based data processing approaches for the analysis of the biomechanics in snowboarding, algorithms for rotation and riding style classification and their application towards feedback systems. However, none of the existing approaches contains an actual trick classification that is applicable to a variety of movements of multiple tricks categories. Furthermore, previously published classification algorithms mostly relied on simple decision-making based on single assumptions instead of considering multiple features and advanced machine learning algorithms. In this thesis, machine learning algorithms are employed for the classification of snowboard tricks of different slopestyle trick categories. IMU data from one sensor per board are obtained and processed. The data are analyzed for trick events and further processed for kinematic feature extraction. Based on calculated orientation features, automatically detected trick events are classified into the corresponding trick category and subsequently into the actual trick class. Multiple classifiers are first used to establish suitable classification models and then evaluated for both the category and the trick classification. The outcome of this work does not only present a classification approach that is extendable to further snowboard scenarios and can be applied for training or broadcast purposes but additionally confirms the potential of defined orientation features for machine learning applications. The described content and corresponding findings were published in [P6].

Skateboarding: Trick classification, visualization and corresponding community perception

With the recent development of skateboarding becoming an Olympic sport, unobtrusive methods for automated trick classification and corresponding motion visualization can not only be used for daily training sessions of amateur athletes but also support professional competitions. The literature shows the research interest in both the classification and the visualization of skateboard tricks. Regarding the trick classification, several approaches were proposed but none of them included real skateboard data of a large variety of different tricks. The published visualization approaches represent the subjective and creative character of skateboarding but do not cover the actual 3D-trick motion. In this thesis, the processing pipeline contains both an automated trick classification and visualization. IMMU data from one sensor per skateboard are processed for kinematic feature extraction and trick classification. Based on mostly orientation features, detected trick actions are classified for the

actual trick class. Multiple classifiers are first used to establish suitable classification models and then evaluated for their accuracy. In addition to the trick classification, the performed motion is visualized by means of a 3D-representation of the board rotation. The classification and visualization algorithms are implemented in a real-time prototype, which is then presented to the board sports community. The corresponding community perception on the prototype and the influence of technology in sports are analyzed with a specifically designed survey. The proposed methods can be used for skateboard sessions of amateurs and professional athletes and potentially, for broadcast support of competitions. The described content and corresponding findings were published in [P7], [P8] and [P9].

1.5 Outline

This dissertation is structured as follows. In Chapter 2, the scientific fundamentals for the implemented technologies and algorithms of this thesis are presented. In Chapters 3 to 5, these fundamentals are applied to sports-specific kinematic analysis in scuba diving, rowing and ski jumping. Further processing of kinematic features for performance interpretation is demonstrated in Chapters 6 and 7 by the application in snowboarding and skateboarding. Chapter 8 contains an overall discussion with a reflection of strength and limitations of the proposed methods and provides prospects of future research. The conclusion in Chapter 9 finalizes this thesis.

2 Fundamentals

This chapter describes the fundamental measurement hardware and data processing methods for this thesis. This includes the IMU and IMMU hardware components, rotation and orientation representation and machine learning algorithms.

2.1 Inertial-magnetic measurement units

Inertial sensing makes use of the physical principle of inertia. In the context of this work, the measurement devices for inertial sensing are referred to as 'IMU' and devices with additional magnetic sensing as 'IMMU'. Both are mostly based on micro electro-mechanical system (MEMS) technology.

2.1.1 Sensing components

Inertial sensing: accelerometer and gyroscope

Inertial sensors contain two sensing components: accelerometer and gyroscope. Both are often based on the principle of a spring-mass-damper system (see Fig. 1). The accelerometer measures the linear acceleration per sensor axis. The gyroscope provides the angular velocity per sensor axis. In a tri-axial sensor unit, both contain measurements on three axes.

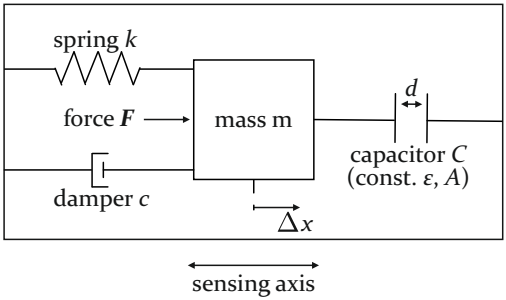

Figure 1: Sketch of a spring-mass-damper system in MEMS accelerometers.

When the spring-mass-damper system is accelerated by external influence, a force $\boldsymbol{F}$ is applied to the mass m. The external influence can be a linear acceleration of the entire system (principle of accelerometer) or result from an angular rotation of the system (principle of gyroscope) that induces Coriolis acceleration [121]. In both cases, the force is directly proportional to the applied acceleration $\boldsymbol{a}$ by Newton's second law of motion:

$$\boldsymbol{F} = m \cdot \boldsymbol{a}. \tag{1}$$

The force $\boldsymbol{F}$ that is applied to the mass m leads to a displacement Δx. Taking the spring constant k and the damping coefficient c into account, the second-order differential equation

$$\boldsymbol{F} = m \cdot \Delta\ddot{x} + c \cdot \Delta\dot{x} + k \cdot \Delta x \tag{2}$$

represents the correlation between the applied force $\boldsymbol{F}$ and the displacement Δx.
The displacement Δx can be determined based on the piezoelectric, the piezoresistive or the capacitive effect. In reference to the primarily employed sensor hardware of this thesis, the capacitive effect is described exemplarily. Assuming a constant voltage U at the capacitor C, the displacement Δx leads to a change in the capacitor's charge ΔQ:

$$\Delta Q(\Delta x) = Q_{\Delta x} - Q_0 = \epsilon \cdot A \cdot U \cdot \left(\frac{1}{d - \Delta x} - \frac{1}{d}\right), \tag{3}$$

with ϵ denoting the permittivity between the conductive plates with the surface area A.
Whereas the resulting linear acceleration $\boldsymbol{a}$ directly represents the required measurement of a one-axis accelerometer, the angular rotation $\boldsymbol{\omega}$ of a gyroscope is obtained with an extended spring-mass-damper model (see Fig. 2).
The commonly used type of gyroscope in MEMS is the vibratory gyroscope. Its functionality is based on a mass m that oscillates with the velocity $\boldsymbol{v}$ in the direction of the drive axis y. When an external rotation with angular rate $\boldsymbol{\omega}$ is applied to an axis orthogonally to the drive axis, the Coriolis acceleration $\boldsymbol{a}_C$ can be measured in the direction of the sensing axis, leading to the displacement Δx [121]. The correlation between the

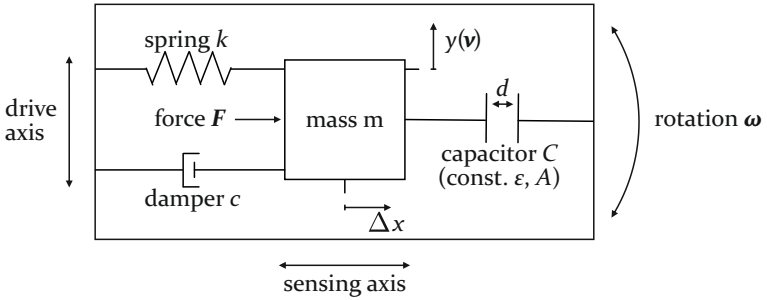

Figure 2: Sketch of an extended spring-mass-damper system in MEMS vibratory gyroscopes.

Coriolis acceleration $\boldsymbol{a}_{\mathrm{C}}$, the corresponding Coriolis force $\boldsymbol{F}_{\mathrm{C}}$ and the angular rate $\boldsymbol{\omega}$ is given by

$$\boldsymbol{F}_{\mathrm{C}} = m \cdot \boldsymbol{a}_{\mathrm{C}} = -2 \cdot m \cdot \boldsymbol{\omega} \times \boldsymbol{v}. \tag{4}$$

Magnetic sensing

Magnetometers measure the magnetic flux. Common MEMS magnetometer principles are based on the Lorentz force, anisotropic magnetoresistance (AMR) and the Hall effect [122]. In reference to the primarily employed sensor hardware of this thesis, the Hall effect-based magnetometer is described exemplarily (see Fig. 3).
An electric current I is sent through a conductor plate with known thickness d. When a magnetic field with flux density B is applied orthogonally to the conductor plate, the electric charges on the plate experience a Lorentz force $\boldsymbol{F}_{\mathrm{L}}$, which is perpendicular to both the current flow and the magnetic field. The Lorentz force induces a current flow on the conductor plate, which is perpendicular to the original flow, and results in the Hall voltage U_{H}:

$$U_{\mathrm{H}} = R_{\mathrm{H}} \cdot \frac{I \cdot B}{d}, \tag{5}$$

with R_{H} denoting the conductor plate's material-specific Hall coefficient [123, 124].

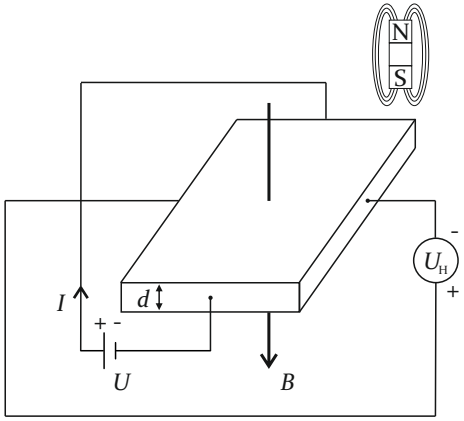

Figure 3: Sketch of the principle of Hall effect-based magnetic flux measurement in MEMS magnetometers.

2.1.2 Advantages and limitations

The advantages of IMMUs are given by their small size, low weight and unobtrusive attachment possibilities. In addition, off-the-shelf products are often available at a low price. IMMUs can be used for outdoor applications that could not be observed by other means of measurements, such as camera-based methods. Furthermore, they can be incorporated into devices of daily use, such as smartphones, smartwatches or instrumented textiles.
However, inertial and magnetic MEMS sensors suffer from specific limitations: deterministic and random measurement errors, the accumulation of errors for certain processing scenarios and the sensitivity to temperature fluctuations and to changes in the surrounding magnetic field. These limitations lead to the following challenges for the use of inertial and magnetic sensors.

Challenges with inertial sensing

Due to their low-cost and small size setup, MEMS IMUs suffer from deterministic and random errors [125, 126]. Deterministic errors include sensor bias, scale factor and orientation error, including possible axes non-orthogonality. Random errors are the drift of these parameters over time.

In addition, MEMS IMUs are influenced by changes in temperature [127]. Especially for outdoor scenarios with considerable temperature fluctuations, this influence has to be considered. In the scope of this thesis, two winter sports applications are analyzed. Both require accurate measurements despite possibly changing temperature. In this context, an evaluation of the temperature influence on the used sensor hardware's accuracy was performed in a climate chamber. The evaluation and corresponding results are provided in Section 5.2.2.
Although small errors in the measurements could possibly be neglected in applications that only require low accuracy (e.g., for the recognition of motion and resting states), the error accumulates in applications with integration of raw measurements. Integration is performed for the establishment of velocity or position estimates (single and double integration of the acceleration) and for rotation estimation (single integration of the angular velocity). Hence, a frequent calibration, preferable at the same temperature as during the data acquisition, is required for accurate results.
Another challenge is the interpretation of inertial data regarding the relative character of the sensing process. The accelerometer and gyroscope only provide measurements in the sensor frame (i.e., relatively to the sensor's coordinate system) instead of in any external frame. As a result, a predefined matching between the sensor's measurement frame with an external frame (e.g., body frame or global frame) is necessary for most applications. In this work, the matching between measurement frame and external frame will be referred to as 'alignment'.

Challenges of magnetic sensing

Besides the deterministic errors that are similar to inertial sensing, the main cause of influence for magnetic sensing is given by changes of the magnetic state of the environment. These lead to hard and soft iron modifications of the sensor output [128]. Hard iron distortions are the result of materials that produce a constant magnetic field and hence, are measured additively to the earth's magnetic field. They can simply be modeled as measurement bias, as long as the magnetic sensor keeps a constant distance and orientation to the material. Soft iron distortions are more complicated to model as they are produced by materials that influence the existing magnetic field. Their influence results in deformation and rotation of the original field and can be minimized by suitable calibration methods.

2.1.3 In-field calibration and alignment

In order to take up these challenges, a sensor calibration and a coordinate system alignment are required. Due to the application-oriented character of this work, only in-field methods, which do not require stationary and cost-intensive lab equipment, are introduced.

Sensor calibration

Whereas random errors can only be modeled stochastically, the deterministic errors can be avoided by an accurate calibration procedure. For the calibration of the accelerometer and gyroscope, the main parameters are the bias vector $\boldsymbol{b}$, scale factor matrix $\boldsymbol{K}$ and orientation matrix $\boldsymbol{R}$ [40]. The influence of these deterministic errors is exemplarily shown in Fig. 4.

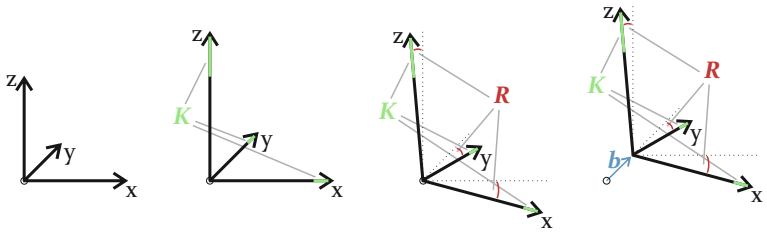

Figure 4: Sketch of the deterministic error influence on inertial-magnetic measurements.

By defined resting states and rotations about single axes, these parameters can be determined in any in-field environment. In addition, a gyroscope zero velocity update (ZVU) can be applied by zeroing the gyroscope readings in resting states in order to correct the gyroscope's bias [129]. Although the standard calibration procedure is usually only performed before or after an acquisition, a ZVU can be performed in all resting states, even during data recording.
In the case of this work, a stable calibration cube of sufficient size for a simultaneous calibration of multiple sensors was built and used for calibration. The cube was placed on a rotary table with adjustable stand. The main purpose of this structure was to ensure a stable in-field outdoor calibration for applications with uneven ground (e.g., at ski jumping

venues on snow-covered mountains). The described calibration setup, including multiple IMMUs attached to the cube, is visualized in Fig. 5.

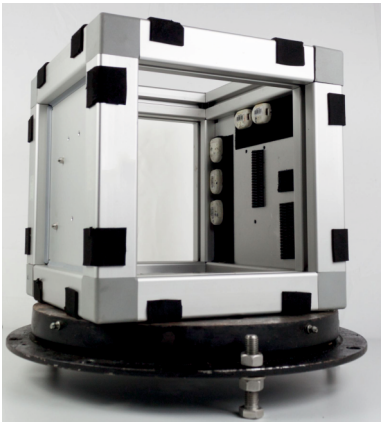

Figure 5: Calibration cube with multiple IMMUs. The placement on a rotary table ensures a stable in-field calibration. © 2017 ACM, printed with permission [P5].

The calibration of the magnetometer is performed to determine the measurement bias $\boldsymbol{b}$, scale factor matrix $\boldsymbol{K}$ and orientation matrix $\boldsymbol{R}$ (see Fig. 4) and the hard iron distortion, which additionally adds a bias to the measurements. Assuming an ideally calibrated magnetometer that rotates in 3D-space, while being at an unaltered 3D-position, all measurements could be visualized on the surface of a sphere. In contrast, the visualization of uncalibrated measurements results in a deformation to an ellipsoid. Thus, the magnetometer can be calibrated by resolving the described deformation. Most calibration methods perform ellipsoid-fitting methods [130, 131]. With a sufficient number of measurements, while the magnetometer is pointing in diverse orientations, a system of calibration equations can be solved for obtaining the corresponding calibration values.

Alignment from measurement to external frame

The alignment from the sensor's internal measurement frame to any external frame is required in order to apply the inertial-magnetic measurements to any other system. In the case of this work, the sensor hardware was attached to athletes or sports equipment, so that the external system can throughout be seen as the body frame of either an athlete

or certain sports equipment. Both the body frame of an athlete and the measurement frame of an attached sensor device are exemplarily shown in Fig. 6.
For an exact alignment between measurement frame $\boldsymbol{f}_{\mathrm{m}}$ and body frame $\boldsymbol{f}_{\mathrm{b}}$, a rotation matrix $\boldsymbol{C}_{\mathrm{m}}^{\mathrm{b}}$ has to be found in order to rotate the measurement frame to the body frame. Basically, this rotation matrix can be computed based on i known states $\boldsymbol{s}_i$ (with a minimum of $i = 2$) that are defined in both frames. For in-field sports applications, these states could for example be given by an athlete standing and lying in a resting position that is oriented perpendicular or parallel to the earth's gravity vector. In the exemplary sketch in Fig. 6, the expected measurement in the body frame $\boldsymbol{f}_{\mathrm{b}}$ would represent the gravity vector on the z-axis (athlete standing perpendicular to the gravity vector) and the x-axis (athlete lying parallel to the gravity vector), respectively. However, the actual measurement in the sensor's measurement frame represents the gravity vector differently. By comparing the actual measured states $\boldsymbol{s}_{i,\mathrm{meas}}$ in the measurement frame to the expected states $\boldsymbol{s}_{i,\mathrm{body}}$ in the body frame, the rotation for the required alignment can be computed.
The problem statement describing the aforementioned scenario is generally known as 'Wahba's problem' [132, 133]. It's goal is to define the rotation between two coordinate systems (or 'frames') based on multiple observations in both systems. In the literature, several solutions were proposed [134]. The most popular ones were Davenport's eigenvector solution [135], also known as 'q-method', and Markley's singular value decomposition (SVD) method [136]. In this work, a SVD was applied for all sensor alignment tasks.

2.1.4 Available sensor hardware

For the data acquisition of this thesis, two IMMUs were incorporated: the miPod and the Shimmer3. Furthermore, an Analog Devices accelerometer was used. The sensor hardware is introduced in this section and then referred to throughout this work.

miPod

The miPod hardware contains an Invensense MPU-9150 inertial-magnetic sensor chip and a Bosch BMP180 barometric pressure sensor [137]. The inertial-magnetic sensor chip provides 16-bit three-axes accelerometer, 16-bit three-axes gyroscope and 13-bit three-axes magnetometer mea-

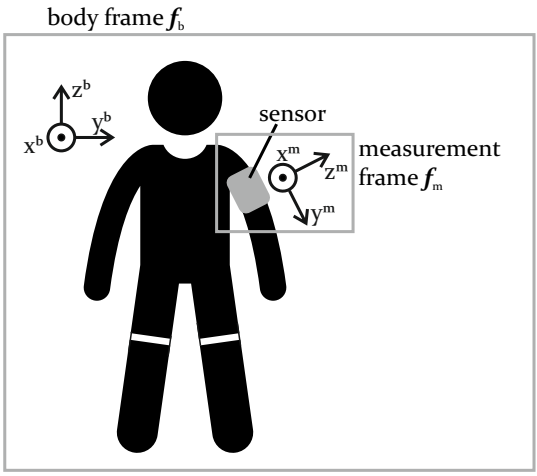

Figure 6: Sketch of the external body frame of an athlete and the internal measurement frame of an attached sensor. Source: 'Athlete' icon (modified) by Gan Khoon Lay from https://thenounproject.com.

surements [138]. The ranges can be configured between ± 2 g and ± 16 g (accelerometer), between $\pm 250 \frac{°}{s}$ and $\pm 2000 \frac{°}{s}$ (gyroscope) and up to $\pm 1200\,\mu$T (magnetometer). In addition, the miPod contains a temperature sensor and a real-time clock (RTC). The miPod runs on a low-power 32-bit ARM Cortex-M3 microcontroller. Data are stored internally on a flash memory with a capacity of 1 GB. The complete unit's weight is 8 g and its dimensions are 35 mm × 25 mm × 8 mm (see Fig. 7), which allows for a wide variety of application in the field of sports.

Shimmer3

The Shimmer3 hardware combines an STMicro LSM303DLHC accelerometer and magnetometer with an Invensense MPU-9150 gyroscope [139]. All components measure on three axes with a resolution of 16 bit per axis. The ranges can be set between ± 2 g and ± 16 g (accelerometer), between $\pm 250 \frac{°}{s}$ and $\pm 2000 \frac{°}{s}$ (gyroscope) and between $\pm 130\,\mu$T and $\pm 810\,\mu$T (magnetometer). The IMMU runs on a 16-bit TI MSP430 microcontroller. Its weight is 24 g and its dimensions are 51 mm × 34 mm × 14 mm (see Fig. 8). The main advantage of the Shimmer3 over the miPod system is that data can not only be stored internally on a microSD card but can also

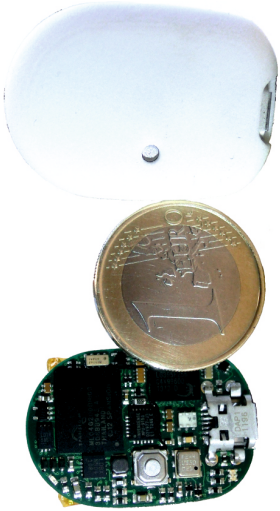

Figure 7: miPod inertial-magnetic measurement unit.

be transmitted in real-time via Bluetooth. However, there is no built-in temperature sensor and no RTC in the Shimmer3.

Figure 8: Shimmer3 inertial-magnetic measurement unit. © 2019 Shimmer, printed with permission.

Analog Devices ADXL330

The Analog Devices ADXL330 provides acceleration sensing on three axes [140]. It measures with a resolution of 10 bit per axis and a range of ± 3 g.

2.2 Rotation sequences and orientation estimation

Measurements of IMU and IMMU devices can be processed to estimate rotation sequences and the devices' current (relative) orientations in 3D-space. By attaching the devices to a body or object, the body's or object's rotation and orientation can be estimated, respectively.

2.2.1 Representation of rotation and orientation

Euler angle representation

There are several methods to represent orientation estimates. The most descriptive representation in Euclidian space is given by Euler angles yaw (z-axis), pitch (y-axis) and roll (x-axis), which are generally denoted by ϕ, θ and ψ. Their limitation lies in the ambiguity of rotation descriptions depending on the order of performed rotation about each axis. An example of a rotation sequence is given by $\boldsymbol{R}_{\mathrm{x}(\psi)\mathrm{y}(\theta)\mathrm{z}(\phi)}$, describing a rotation about the z-axis, followed by a rotation about the y-axis and a rotation about the x-axis. In total, there are six different rotation sequences, which, depending on the rotation magnitude, all lead to (slightly) varying results. Furthermore, Euler angle-based rotations contain the risk of a gimbal lock state, i.e., a state in which two rotation axes are aligned parallel to each other [141]. This effect leads to the loss of the system's ability to fully rotate in 3D-space.

Rotation matrix representation

In contrast to three consecutive rotations about three axes, a rotation matrix describes one simultaneously performed rotation about all axes and thus, provides an unambiguous rotation representation. Still, if a rotation matrix is established from given Euler angles, the order of the

sequence has to be defined. The rotation matrix for the aforementioned example $\boldsymbol{R}_{\mathrm{x}(\psi)\mathrm{y}(\theta)\mathrm{z}(\phi)}$ is described by

$$\boldsymbol{R}_{\mathrm{x}(\psi)\mathrm{y}(\theta)\mathrm{z}(\phi)} = \begin{bmatrix} c(\psi)\,c(\theta) & c(\psi)\,s(\theta)\,s(\phi) - s(\psi)\,c(\phi) & c(\psi)\,s(\theta\,c(\phi) + s(\psi)\,s(\phi) \\ s(\psi)\,c(\theta) & s(\psi)\,s(\theta)\,s(\phi) + c(\psi)\,c(\phi) & s(\psi)\,s(\theta)\,c(\phi) - c(\psi)\,s(\phi) \\ -s(\theta) & c(\theta\,s(\phi) & c(\theta)\,c(\phi) \end{bmatrix}, \tag{6}$$

with $c()$: cos and $s()$: sin.
With their unique rotation representation, rotation matrices overcome the ambiguity issue of Euler angles and in addition, do not suffer from the gimbal lock problem. However, they have limitations regarding increased storage requirements (in 3D-space: nine components instead of three) and higher computational costs of matrix operations. Both have to be considered for embedded and real-time applications.

Quaternion representation

Another rotation representation is provided by quaternions. A quaternion $\boldsymbol{q}$ is defined by a scalar part q_0 and a vector part $\boldsymbol{q_v}$:

$$\boldsymbol{q} = q_0 + \boldsymbol{q_v} = q_0 + q_1\boldsymbol{i} + q_2\boldsymbol{j} + q_3\boldsymbol{k}, \tag{7}$$

with $\boldsymbol{i} = [1\ 0\ 0]^\mathsf{T}$, $\boldsymbol{j} = [0\ 1\ 0]^\mathsf{T}$ and $\boldsymbol{k} = [0\ 0\ 1]^\mathsf{T}$ [142].
Alternatively, the quaternion $\boldsymbol{q}$ can be represented by a 4-tuple:

$$\boldsymbol{q} = \begin{bmatrix} q_0 \\ \boldsymbol{q_v} \end{bmatrix} = \begin{bmatrix} q_0 \\ q_1 \\ q_2 \\ q_3 \end{bmatrix}. \tag{8}$$

Following the Euler-Rodrigues rotation representation [143], any rotation

with a magnitude Ω and a rotation vector $\boldsymbol{v}$ (see Fig. 9) can be represented by a quaternion $\boldsymbol{q}$ with

$$\boldsymbol{q} = \begin{bmatrix} \cos(\frac{\Omega}{2}) \\ v_x \cdot \sin(\frac{\Omega}{2}) \\ v_y \cdot \sin(\frac{\Omega}{2}) \\ v_z \cdot \sin(\frac{\Omega}{2}) \end{bmatrix}. \tag{9}$$

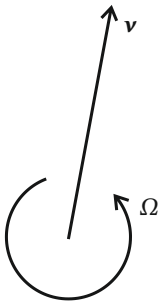

Figure 9: Sketch of the quaternion-based rotation representation. Each quaternion $\boldsymbol{q}$ represents a rotation with magnitude Ω about a rotation vector $\boldsymbol{v}$.

Quaternions combine the advantages of both aforementioned representation forms by providing unambiguity in combination with low storage and processing costs. A typical application for quaternion-based processing is the combination of two rotations. Instead of computing the time-consuming multiplication of two 3×3-matrices, two rotations can be combined by the multiplication of corresponding quaternions $\boldsymbol{q}$ and $\boldsymbol{r}$ with

$$\boldsymbol{q} \cdot \boldsymbol{r} = q_0 \cdot r_0 - \boldsymbol{q_v} \cdot \boldsymbol{r_v} + q_0 \cdot \boldsymbol{r_v} + r_0 \cdot \boldsymbol{q_v} + \boldsymbol{q_v} \times \boldsymbol{r_v} \text{ [143]}. \tag{10}$$

Disadvantages of the quaternion representation are the increased interpretation effort and the lack of direct visualization per dimension. While simple rotations can often be interpreted intuitively in Euler angle and rotation matrix representation, the quaternion representation, with its scalar and vector parts, is more complex to interpret. Based on this com-

plex representation in 3D-space, the visualization of partial rotations in each dimension is not directly possible without prior preprocessing.

2.2.2 Principles for IMMU-based rotation estimation

The IMMU components can be used for the estimation of performed rotations and the current orientation of the device. However, the achieved accuracies vary, depending on the limitations stated in Section 2.1.2. Whereas the gyroscope is basically used to determine the rotation based on the measured angular velocity, the accelerometer and magnetometer are used to determine the static orientation with measurements of the gravity and earth's magnetic field.

Gyroscope-based rotation estimation

Gyroscope-based integration of the measured angular rate $\boldsymbol{\omega}$ with given sampling frequency f leads to an estimation of the relative rotation angles from start to end of the rotation process (t_0 to t), i.e., the resulting Euler angles at t represent the rotation in reference to the initial orientation at t_0:

$$\begin{aligned} \Delta\phi &= \frac{1}{f} \cdot \int_{t_0}^{t} \omega_z(t)\, dt \\ \Delta\theta &= \frac{1}{f} \cdot \int_{t_0}^{t} \omega_y(t)\, dt \\ \Delta\psi &= \frac{1}{f} \cdot \int_{t_0}^{t} \omega_x(t)\, dt. \end{aligned} \tag{11}$$

This axis-wise integration can be used for simple rotations, such as a rotation about mainly one axis. However, for rotations about two or all sensor axes at the same time, computation errors are induced due to the ambiguity of the rotation sequences (see limitations of Euler angle representation in Section 2.2.1).
An alternative integration is possible with quaternion-based representation. Assuming a linear rotation between sampling steps (requires sufficiently high sampling frequency f), the rotation about all three axes is directly converted to a quaternion for each sampling step t. Following

Eq. 9, the quaternion $\boldsymbol{q}_t$ is calculated with the corresponding magnitude Ω and rotation vector $\boldsymbol{v}$:

$$\begin{aligned} \Omega &= \frac{1}{f} \cdot \left|\left|\boldsymbol{\omega}_t\right|\right|_2 \\ \boldsymbol{v} &= \frac{\boldsymbol{\omega}_t}{\left|\left|\boldsymbol{\omega}_t\right|\right|_2}. \end{aligned} \tag{12}$$

The quaternion $\boldsymbol{q}_t$ represents the unambiguous rotation sequence for the corresponding sampling step at time t. The overall rotation over time is obtained by multiplication of consecutive quaternions.
Although a short-term integration can lead to sufficiently accurate estimates, a long-term integration of the angular rate causes a continuous drift. The error accumulates over time and increases even faster for insufficiently calibrated sensor hardware.

Accelerometer-based orientation estimation

In contrast to the gyroscope-based rotation estimation during motion, the accelerometer measurements are mostly processed for resting states. By measuring the acceleration during resting states, only the earth's gravity influences the measurement. Thus, for resting states, the direction of the gravity vector can be processed for orientation determination. However, this process suffers from two major limitations: the existence of resting states and the interpretation of ambiguous estimates. First, resting states have to be detected reliably in order not to process motion acceleration for orientation estimation. Second, the resulting calculation is ambiguous in 3D-space due to the fact that a rotation about the gravity vector (i.e., parallel to the earth's surface) between two measurements, would not change the acceleration measurement of the gravity vector. Thus, the combination with other measurement methods is required for most applications.

Magnetometer-based orientation estimation

The magnetometer's orientation estimation is based on the earth's magnetic field. While the accelerometer measurements can be used to determine the sensor's orientation relative to the earth's gravity vector, the magnetometer measurements can be used to determine the orientation relative to the earth's magnetic field vector. Thus, the magnetometer suffers from a similar limitation: rotations about the magnetic field

vector are not visible in the magnetometer signal and a combination with other measurement methods is required. In theory, the combination of accelerometer and magnetometer is sufficient to obtain the 3D-spatial orientation in static scenarios. In practice, insufficiently calibrated sensor components and changing environmental influence can corrupt the estimation.

2.2.3 Data fusion

In order to overcome the limitations of estimates based on single sensor components, a sensor data fusion is necessary for a robust orientation estimation in 3D-space [144]. Well-known fusion approaches for this task can be separated in Bayes filter (e.g., Kalman filter and particle filter) and complementary filter (e.g., Madgwick's filter).

Bayes filter

A Bayes filter basically provides the estimation of the posterior probability density function of a state vector $\boldsymbol{x}_t$ based on the prior state $\boldsymbol{x}_{t-1}$ and additional observations $\boldsymbol{z}_t$ [145]. In the case of orientation estimation, $\boldsymbol{x}_t$ contains a representation of the currently estimated orientation (e.g., by Euler angles or a quaternion) and possibly further information, such as the angular rate.
The standard application of a recursive Bayes filter contains two steps. In a first step (prediction step), the state $\boldsymbol{x}_t$ is predicted with a (non-)linear function f:

$$\boldsymbol{x}_t = f(\boldsymbol{x}_{t-1}, \boldsymbol{w}_{t-1}), \tag{13}$$

with $\boldsymbol{w}_t$ denoting process noise. In a second step (update step), $\boldsymbol{x}_t$ is updated based on the observations, i.e., based on all measured sensor data $\boldsymbol{z}_t$:

$$\boldsymbol{z}_t = f(\boldsymbol{x}_t, \boldsymbol{v}_t), \tag{14}$$

with $\boldsymbol{v}_t$ denoting measurement noise.
A widely used recursive Bayes filter approach is the Kalman filter [146, 147], which directly represents the Bayes filter description for linear variables with normally distributed probability density. Its extensions for non-linear systems are the extended Kalman filter [147] and the unscented Kalman filter [148].
Another application of recursive Bayes filter is the particle filter [149, 150]. It follows the same procedure as Kalman filters but its probability density

is represented by multiple particles of which each of them represents a possible state $\boldsymbol{x}_t$. The advantage of the particle filter lies in its straightforward implementation of non-linear and non-Gaussian conditions, however, at the cost of increased computational effort.

Complementary filter

The basic idea of complementary filtering is the (weighted) combination of two or more input values. In the case of orientation estimation, the filter output $\boldsymbol{x}_t$ could simply represent the current orientation estimate Ω_t. In an example with two sensor measurements as input values, the filter output would be computed based on the estimates $\Omega_{1,t}$ (sensor 1) and $\Omega_{2,t}$ (sensor 2) with the weight parameter $p \in [0;1]$:

$$\Omega_t = p \cdot \Omega_{1,t} + (1 - p) \cdot \Omega_{2,t}. \tag{15}$$

Madgwick et al. [41] proposed an orientation estimation approach with accelerometer, gyroscope and optionally, magnetometer data. The quaternion $\boldsymbol{q}_t$ represents the currently estimated orientation. The change of orientation per sampling step is represented by the quaternion derivative $\dot{\boldsymbol{q}}_t$. For the gyroscope, the angular rate measurement $\boldsymbol{\omega}_t$ is directly transformed to $\dot{\boldsymbol{q}}_{\boldsymbol{\omega},t}$ (see Eq. 9 and 12). The measurement of accelerometer and magnetometer are first preprocessed. For the gravity and the earth's magnetic field, there is no single orientation solution possible in 3D-space. Instead, the ambiguity of the sensor output is optimized with a gradient descent algorithm in order to obtain $\dot{\boldsymbol{q}}_{\nabla,t}$, containing the estimated change of orientation from accelerometer and magnetometer measurements. The resulting change of orientation $\dot{\boldsymbol{q}}_t$ is calculated by a complementation of both the gyroscope-based estimate and the gradient descent algorithm with an adjustable weight parameter β:

$$\dot{\boldsymbol{q}}_t = \dot{\boldsymbol{q}}_{\boldsymbol{\omega},t} - \beta \cdot \dot{\boldsymbol{q}}_{\nabla,t}. \tag{16}$$

The resulting orientation $\boldsymbol{q}_t$ is calculated by the subsequent integration of $\dot{\boldsymbol{q}}_t$:

$$\boldsymbol{q}_t = \boldsymbol{q}_{t-1} + \dot{\boldsymbol{q}}_t \cdot \Delta t. \tag{17}$$

The parameter β describes the gyroscope measurement error, represented by the magnitude of the quaternion derivate. It is often defined by the maximum gyroscope error per measurement axis $\omega_{\text{max},\{x,y,z\}}$ and can be simplified for equal errors per axis to

$$\beta = \sqrt{\frac{3}{4}} \cdot \omega_{\text{max}} \text{ [41]}. \tag{18}$$

2.3 Machine learning

The interpretation of acquired data often focuses on the analysis of recurring events. In sports, these events can be shots, jumps, strokes or any other activity that is of value for the analysis. All events contain patterns providing information about the event, e.g., about the quality of a performed tennis stroke. In order to detect and assess these events and automatically interpret existing patterns, machine learning methods can be applied to the obtained signals.
Typical machine learning applications consist of two main stages: the training and the classification. In the training stage, a suitable classification model is established and optimized on existing training data. In the classification stage, unknown data are processed and classified based on the previously trained model.
This section provides an overview of the most relevant aspects of machine learning methodology for this thesis. Detailed scientific background on the machine learning pipeline and corresponding techniques is beyond the scope of this thesis but can be found in the literature [151, 152].

2.3.1 Machine learning pipeline

The typical processing pipeline for machine learning contains preprocessing, event detection, feature extraction, possibly a feature selection and finally, the classification (see Fig. 10). The additional training procedure is used initially to establish a suitable classification model with selected features based on existing training data.

Preprocessing

The first step of the pipeline consists of signal preprocessing. Its goal is to prepare signals for standardized treatment. Typical methods include the handling of missing data, noise removal and outlier detection [153].

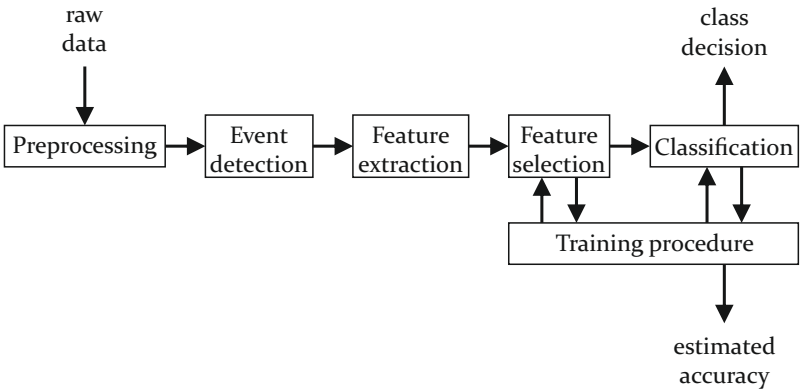

Figure 10: Typical machine learning pipeline, including the training procedure for the feature selection and the classification model.

Furthermore, an application-specific standardization can be required. Many signals resemble each other and contain similar information but cannot be processed equally. In the example of a tennis stroke analysis, these resembling signals could be IMU readings corresponding to forehand tennis strokes performed by a left-handed and a right-handed athlete. If an analysis is focused on the stroke quality only, the handedness of the athlete does not influence the resulting quality. However, although both the left-handed and the right-handed signals contain the required information, both motions vary greatly in the movement direction and cannot be compared directly. Thus, the aim of the standardization is to adapt input signals to the same base. This can include transforming signals to the same coordinate system, calibrate them for the removal of unwanted offsets or simply convert them to the same unit.

Event detection

For most applications, an event detection is necessary. In the example of the tennis stroke analysis, only the signal segment containing the actual stroke scenario is of interest for classification and hence, has to be separated before further processing. Depending on the computational power and real-time requirements, continuous signals can either be analyzed step-wise for each sampling step or with a moving-window approach, including an overlap to avoid missing relevant data.

The actual detection is closely tied to the performed action. For sports applications, impacts like shots, strokes or jumps are typically represented by peaks in the acceleration signal [62, 154, 155]. If accompanied by strong rotations (e.g., during a tennis stroke), these impacts also induce detectable peaks in the gyroscope signal. In contrast to emerging peaks, events can also be detected by the absence of distinct signal characteristics. During athletic jumps with considerable *air time*, IMU signals are characterized by a lower noise level due to missing ground contact and lower gravity measurements during the free-fall period of the jump [156]. Whenever a specified detection algorithm identifies a signal area of interest, the containing signal segment (and possibly a short period of time before and after the detected area) is defined as event and provided for further processing. Events that are falsely detected and do not contain any relevant information (false positives) have to be considered later in the processing chain and should be recognized and filtered out in the classification process.

Feature extraction

All detected events are provided for further analysis. The corresponding signal segments contain a specified time interval of possibly multi-dimensional data. For many applications, feature extraction is performed in order to minimize the computational effort and to possibly improve the classification accuracy. In this process, multiple features are defined and extracted from the multi-dimensional data [157]. Features can be defined manually or automatically. Although this work is focused exclusively on manually defined features, automatic methods, such as representation learning [158], have to be considered for a balanced overview of the topic. Features can be separated in generic features and expert features (also known as domain-specific features). Generic features do not represent the actual action but focus on standardized measures. Typical generic features cover both time-domain (e.g., mean, standard deviation, maximum amplitude) and frequency-domain (e.g., fast Fourier transform (FFT) coefficients, spectral entropy, spectral energy) [159]. In contrast to generic features, expert features are specifically designed for the performed action and required classification. For instance, in order to perform a high-quality tennis stroke, it is important not to stop the racket movement right after the ball contact but to continue the motion until the ball leaves the racket. Hence, an expert feature for later quality classification could contain the time duration between hitting the ball and

decelerating the movement. In the case of this work, chosen expert features relate to the rotation or orientation of an object, e.g., the overall rotation during the selected signal segment per sensor axis.

Feature selection

From all extracted features, some prove more relevant for the later classification process than others. Often, multiple features are redundant, do not provide relevant content or even contain misleading information. Feature selection can be employed to decrease the number of features, decrease the computational effort of the classification and in case of removing misleading feature content, even improve the classification performance. If a feature selection is included in the pipeline, the relevant features are determined in the previous training procedure. An extended overview of the feature selection process was provided by Tang et al. [160]. There are several feature selection methods. The most common ones can be categorized into filter, wrapper and embedded approaches [161].
Filter approaches are processed before the actual classification and hence, provide an advantage by being independent of the applied classifier. A ranking is computed for the interaction of a feature and the corresponding label. Only the highly ranked features are processed in the classification. Common methods for the establishment of this ranking are the Fisher score [152], mutual information [162] and ReliefF [163].
In contrast to filter approaches, wrapper approaches perform the selection in reference to the applied classifier. Multiple subsets of the full feature set are used for classification and evaluated for the corresponding accuracy. Wrapper approaches differ in the selection of appropriate subsets. Whereas some approaches simply add features to an initially empty feature list until the maximum accuracy is reached (e.g., hill-climbing), others perform an exhaustive search with all possible feature subsets, which can result in high computation times for large feature sets. The most common strategies for wrapper approaches include hill-climbing, best-first, branch-and-bound and genetic algorithms [160, 164].
Similar to wrapper approaches, embedded approaches select suitable features in reference to the applied classifier. However, they are integrated in the fitting process of the classifier and hence, do not require to run the full process of fitting and testing multiple times and thereby produce less computational effort. Typical embedded feature selection approaches are provided by decision trees [161] and by using the weight vector of support vector machines (SVMs) [165].

Classifiers

The establishment of a suitable classification model is based on one or the combination of multiple classifiers, which relate the values of (selected) features to the corresponding class. The class decision is based on a previous training with a defined training data set, which will be explained in more detail in the next section.
The following classifiers were applied for classification tasks of this work.

k-Nearest neighbor (kNN) is a non-parametric classifier that makes its class decision based on the labels of the k-nearest neighbor samples in the training data set. The k nearest neighbors are found by their distance in feature space. The distance from the current sample to the k nearest neighbor samples is calculated with a distance function d (e.g., Chebyshev or Euclidean). The class majority of the k neighbor samples leads to the classification decision of the current sample. A more complex version of the algorithm is given by the weighted kNN, which allows for a higher weight assignment to features that are more relevant for the classification than others. More detailed background on kNN can be found in [166].

Naïve Bayes (NB) is a probabilistic classifier based on Bayes' theorem. Prior probabilities and dependencies between the class labels and feature values in the training data set are processed for the class decision of the current sample. The probability $P(\mathrm{A} \mid \mathrm{B})$ of belonging to class A with given feature values B is then computed with $P(\mathrm{B} \mid \mathrm{A})$ (the probability of feature values B with given class A) and the single probabilities $P(\mathrm{A})$ and $P(\mathrm{B})$:

$$P(\mathrm{A} \mid \mathrm{B}) = \frac{P(\mathrm{B} \mid \mathrm{A}) \cdot P(\mathrm{A})}{P(\mathrm{B})}. \tag{19}$$

NB is based on the assumption that all features are independent of each other. More detailed background on NB can be found in [167].

Decision tree is a non-metric classifier that allows for including nominal data. Its representation of the training data set can be visualized in a flowchart-similar structure. Feature-based decisions (e.g., exceeding a certain threshold) are represented as nodes of the tree, starting with the first feature as the root node. Decisions for a nominal feature value or a selected range of feature values lead from one node to the next node in connecting branches. After several decisions, the resulting class label is reached in the leaf node. However, each decision in the tree's generation

process could possibly lead to inefficient structures, which decreases the resulting accuracy. Furthermore, a limited depth of the tree is essential in order to avoid overfitting. More detailed background on decision trees can be found in [168]. The following two decision tree implementations were applied in this thesis.

(I) **C4.5** is a specific decision tree classifier that provides a method for tree generation without the limitation of including inefficient structures. The information gain is calculated and considered for each level of the tree and the corresponding features. The root, as well as all further nodes, is occupied by features that lead to the most effective structure. Furthermore, C4.5 applies pruning after the tree's generation, i.e., it optimizes the size of the tree by cutting off irrelevant branches. More detailed background on C4.5 can be found in [169].

(II) **Random forest (RF)** is a further method for handling decision tree limitations. A multitude of randomly selected decision trees is created. By the random selection of root and nodes, the forest can be assumed to contain both accurate but also poorly performing decision trees. By combing the outcome of all trees, the resulting model represents a well performing classifier. More detailed background on RF can be found in [170].

Support vector machine (SVM) is a non-probabilistic and linear classifier that relies on support vectors. These support vectors divide the training data set in corresponding classes. Optimized support vectors define a hyper plane separating the classes in a way that the space between the classes is maximized. The margin for the class separation is influenced by the parameter C, which defines the cost of misclassification. More detailed background on SVMs can be found in [171, 172]. The following two SVM implementations were applied in this thesis.

(I) **Linear support vector machine (LSVM)** is a SVM approach for linear class separation. In 2D, the constructed hyper plane could simply be visualized as a line that divides the classes. Its advantage is the low computational effort. Its disadvantage is the application to non-linear class distributions. For non-linear problems, non-linear kernel functions are incorporated.

(II) **Radial-basis kernel support vector machine (RB-SVM)** is a SVM approach that incorporates a non-linear kernel function,

more specifically, a radial-basis kernel. Based on the selected kernel function, the sample distribution is extended to a multi-dimensional feature space. In a sufficiently high-dimensional representation, the hyper plane divides the classes of the non-linear problem, however, on the cost of potentially highly increased computational effort. The radial-basis kernel function contains the adjustable kernel parameter γ.

2.3.2 Training stage

The described machine learning pipeline requires an initial training procedure for the establishment of the classification model. In the context of this work, only supervised learning methods are employed, i.e., all existing data are inspected manually and the class definition and the corresponding labeling process occur supervised. An overview of supervised and unsupervised learning methods can be found in the literature [152].

Procedure

The full training procedure contains three steps: training, validation and test. In the training step, a classification model that relates the feature values to the corresponding labels is established. In the validation step, the model is validated with so far unseen data and the parameters of the model are optimized. Furthermore, an important task of the validation step is to avoid overfitting that occurs if the model is fitted to tightly to the training data. Several repetitions and adaptations of training and validation steps are possible. In the final test step, the accuracy of the established model is validated with an independent test data set that did not influence the design of the model.

Classes and data labeling

In the labeling process, the available training data are manually assigned to one of the existing classes. In the case of the forehand tennis stroke quality analysis, these classes could for example be 'good', 'okay' and 'bad'. The labeling process is typically performed manually by either analyzing the performance directly (e.g., a tennis coach rates the stroke execution quality) or by relating to the corresponding outcome (e.g., 'good': the ball reaching the intended location on the opponent's field, 'okay': the ball reaching the field but in a different location or 'bad': the ball did not reach the field at all). The latter could also be determined automatically,

e.g., by incorporating a video system that detects if the ball reached the field or not.

Data sets

The full data set, containing detected events and corresponding labels, are separated into three sets: training, validation and test. Often, the separation between training and validation occurs indirectly within the classifier's internal optimization procedure and hence, the data input only has to be separated into fitting (training and validation) and test set. Common procedures for data separation with motion data of multiple athletes are k-fold cross-validation (CV) and leave-one-subject-out cross-validation (LOSO-CV).
In a k-fold CV, the full data set is randomly divided into k subsets. k-1 subsets are used for the fitting process and the one remaining subset is used for testing the established model. This process is repeated k times with a different subset used for testing in each repetition. This way, all subsets are incorporated into the fitting process and every subset is used for testing exactly once.
The LOSO-CV follows a similar procedure but instead of dividing the full data set randomly, the data are separated depending on the subjects. In the application of this thesis, the number of subjects k equals the number of participating athletes. For instance, if the full data set contains data of 20 athletes, the fitting and testing process is repeated 20 times. Each time, the data of another subject are used for testing, while the rest are used for fitting. Consequently, the model is never fitted with any data of the test subject.

Part II

Unobtrusive Kinematic Analysis

The second part of this thesis is focused on the processing of unobtrusively obtained sensor data for kinematic analysis. This process is illustrated by the examples of scuba diving in Chapter 3, rowing in Chapter 4 and ski jumping in Chapter 5. Kinematic features are mainly established by the orientation of either body parts (scuba divers' upper bodies and shanks) or the equipment that is used by athletes (rowing boats and skis). In addition, further kinematic features, such as the continuous velocity and position, are computed based on the prior orientation determination.

3 Scuba Diving: Pose Determination of Divers' Bodies and Shanks

In this chapter, methods for kinematic analysis in scuba diving are proposed. Kinematic analysis in scuba diving is often restricted to areas that can be visually observed. This limitation can be overcome by including wearables. Despite the manifold research interest in wearable technology, there is no known publication that established and evaluated a wearable sensor-based orientation calculation with respect to the required accuracy for analyzing underwater kinematics. In this thesis, a wearable approach for kinematic analysis in scuba diving is presented. Multiple IMUs are attached to the bodies of divers. In an underwater environment, the motion of the divers is monitored by a fin kick detection algorithm. The corresponding shank orientation during fin kicks and several body poses are calculated based on IMU data and evaluated with an underwater camera system. The content of this chapter was published in [P1].

3.1 Data acquisition

3.1.1 Hardware setup

The data acquisition was performed with three miPod sensor systems ([137], see Section 2.1.4). Only accelerometer and gyroscope data were required for later processing. Hence, the miPod system will also be referred to as 'inertial sensor' or 'IMU' in this chapter. All IMUs were configured to an accelerometer range of $\pm 4\,\mathrm{g}$ and a gyroscope range of $\pm 1000\,\frac{^\circ}{s}$. The sampling rate was set to 200 Hz. The three IMUs were placed into a waterproof bag and two underwater camera housings and strapped to the divers: one to the chest and two to the shanks. The sensor attachment and the defined body coordinate system are shown in Fig. 11. For the underwater environment, a stable construction was needed for the diver to hold on to for performing fin kicks without moving forward. This fixed position of the diver was necessary for the camera-based evaluation, which required a video recording of constant distance and perspective. Furthermore, the stable construction was supposed to be aligned with the ground of the pool and wide enough for the diver to lie on. These requirements were met by a wooden bench, which was placed stationary

on the ground of the pool. For more stability, additional weight of 30 kg was attached to the bench.
The camera recording was performed with an underwater camera Sealife DC1400 HD. The resolution was set to 1280 × 720 pixels at a frame rate of 30 fps. The camera was attached to a tripod, which was placed stationary in a distance of approximately 5 m to the divers' legs. It was aligned perpendicular to the shanks in a way that the image plane represented the sagittal plane of the diver (see Fig. 12).

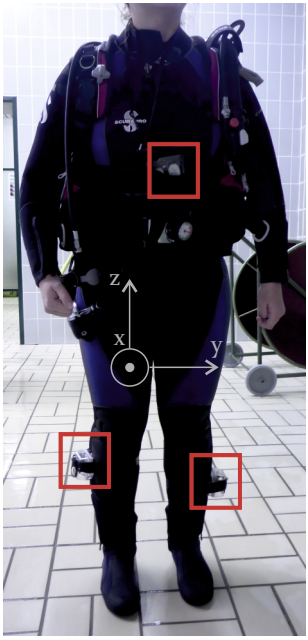

Figure 11: IMU attachment to a scuba diver and the corresponding coordinate system. One IMU was mounted to the chest in an underwater smartphone bag. Two further IMUs were attached to the shanks in waterproof camera housings. © 2015 IEEE, printed with permission [P1].

3.1.2 Study design

The study was performed with ten licensed and experienced scuba divers (six female, four male, age (years): 37 ± 9, height (cm): 172 ± 9). The subjects performed scenarios containing motion tasks and resting states. All

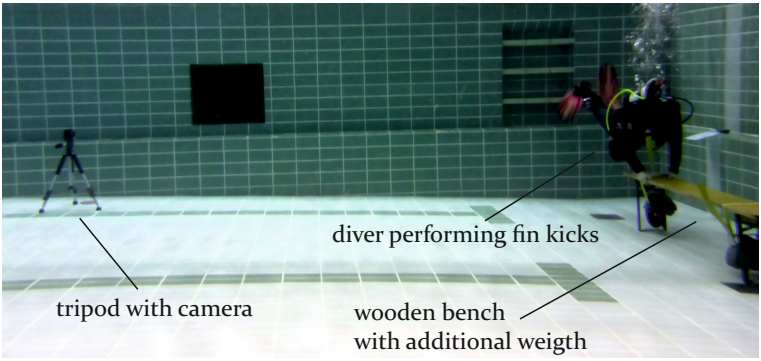

Figure 12: Overview of the underwater data acquisition. One diver is performing fin kicks on a wooden bench. A video camera was placed in a straight line to the diver's shanks with a distance of approximately 5 m. © 2015 IEEE, printed with permission, modified from [P1].

subjects were informed of diving-related risks and gave written consent to participate in the study and for the collected data to be published.
In the preparation phase of the study, each subject performed defined resting positions outside of the pool. These positions were 'standing still' and 'lying face-down' on the ground for approximately 15 s each. The corresponding IMU data were necessary for later calibration and alignment.
The main acquisition was performed under water and consisted of two aspects: the determination of the upper body orientation during resting states and the determination of the shank orientation during motion.
For the determination of upper body orientation, each subject had to rest in several positions. Depending on the subject, four to eight poses were performed, each with a duration of approximately 10 s. These poses were required to include inclination of the diver's frontal plane to represent different upper body angles in reference to the ground. Fig. 13 shows three examples of poses in resting states. For the analysis, only the data of the IMU at the chest were processed.
The shank orientation was analyzed during fin kick motion. The subjects were asked to lie face-down on the bench and hold on to it while performing fin kicks. The legs were not supposed to lie on the bench in order to freely perform the fin kick motion. Only regular fin kicks (flutter kicks) were requested in this study. Each diver performed three sequences: one slow motion interval with low amplitude, one strong motion with high

amplitude and one self-defined motion that represented the fin kicks of a typical dive. Each sequence was supposed to contain approximately 20 fin kicks. A fin kick was defined by a half motion cycle of the typical up-and-down movement. This means one kick was counted when changing from left-leg-down / right-leg-up to left-leg-up / right-leg-down.

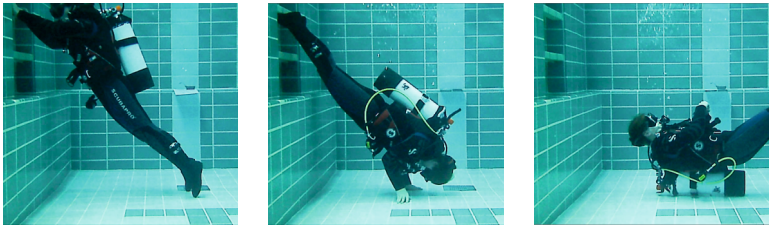

Figure 13: Examples of resting poses for the determination of the upper body orientation with an IMU attached to the chest. © 2015 IEEE, printed with permission [P1].

3.2 Calibration and alignment

The obtained sensor data were calibrated following the algorithm of Ferraris et al. [40] (see Section 2.1.3), approximately two hours prior to the data acquisition. In addition, the resting state data of the preparation phase of the study were used for a ZVU, a few minutes before the athlete started the dive.

The alignment from measurement to body frame (see Section 2.1.3) was performed with the data of the preparation phase. Two vector pairs were defined for the two states 'standing still' and 'lying face-down'. Both pairs contained measured data (sensor's measurement frame) and expected data (body frame). Due to the resting states in both cases, the acceleration data of the gravity measurements were used to establish the rotation matrix for the required alignment. Subsequently, all further sensor measurements were rotated to the diver's body frame. The body frame was defined to represent the diver's body by the sagittal axis x, the frontal axis y and the longitudinal axis z (see Fig. 11).

3.3 Upper body analysis

3.3.1 Orientation calculation

The orientation of the upper body was established for all resting poses. Only the acceleration measurements were used in consideration that the measured acceleration ideally only represented the gravity. The measurements were averaged over the duration of each resting state to the acceleration vector $\boldsymbol{a}$. The scuba divers were asked to select poses that only vary by a rotation about their frontal axis (y-axis, see Fig. 11). The inclination angle θ_{body} of the upper body could then be calculated by processing the x- and z-components of the acceleration vector with

$$\theta_{\text{body}} = \arctan\left(\frac{a_z}{a_x}\right). \tag{20}$$

3.3.2 Evaluation

The calculated angles were compared to the camera-based ground truth. In total, 33 resting poses were analyzed. The corresponding intervals in the acceleration data and the video signal were selected based on notes taken during the study, the video recording and a manual signal analysis. The resting state interval duration varied between 0.5 s and 8.0 s based on the divers' varying ability for holding a stable position under water. For each interval, one video frame was selected manually and analyzed with Kinovea video processing software [173]. Two vectors per pose were manually defined in the software and Kinovea provided the corresponding inclination angle. Example images of the evaluation are provided in Fig. 14.

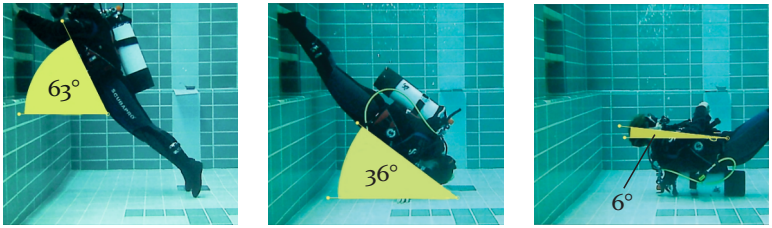

Figure 14: Evaluation of the upper body inclination in reference to the ground. The analysis is shown for three different example poses with Kinovea video software. © 2015 IEEE, printed with permission [P1].

3.4 Fin kick analysis

For the fin kick analysis, the recorded data during fin kick intervals were processed. First, these intervals were segmented with a two-step approach. Second, the absolute shank angles in reference to the ground at the turning points between up- and down movements were computed with the acceleration signal, similar to the upper body orientation analysis. Third, the relative angle covered during each fin kick was calculated with the gyroscope data.

3.4.1 Automated kick detection

Fin kick definition

The detection of single kicks was performed automatically by segmenting the continuous IMU signal. Both legs were analyzed individually. Fin kicks were defined by the motion turning points, i.e., from the lowest (t_{down}) to the highest point (t_{up}) of the shank movement and vise versa (see Fig. 15). The gyroscope's y-axis signal was chosen for processing because the main part of the motion during fin kicks was executed about the diver's frontal axis. In the signal, the required turning points t_{down} and t_{up} are represented by the zero-crossings (see Fig. 16). These are located between the signal's minima and maxima, which represent the highest negative and positive angular velocities between the turning points.

Signal analysis

Due to the expected similarity of all fin kicks in the angular rotation, the template-based matching algorithm dynamic time warping (DTW) [174] was used for the recognition of the fin kick motion pattern. The algorithm's extension for continuous recognition of the pattern, subsequent dynamic time warping (subDTW) [175], was applied in order to detect the template not only once but multiple times in the signal. For reasons of robustness, the signal was not segmented at the physical turning points but at the minima of the signal (see Fig. 17, upper plot). Subsequently, all detected intervals were analyzed for zero-crossings. The interval between the zero-crossings represent the upward (positive rotation) and downward motion (negative rotation) (see Fig. 17, lower plot). For reasons of simplicity, the subDTW template for all participants' fin kicks was defined by manually selecting one random kick (signal minimum to subsequent signal minimum) of the first subject.

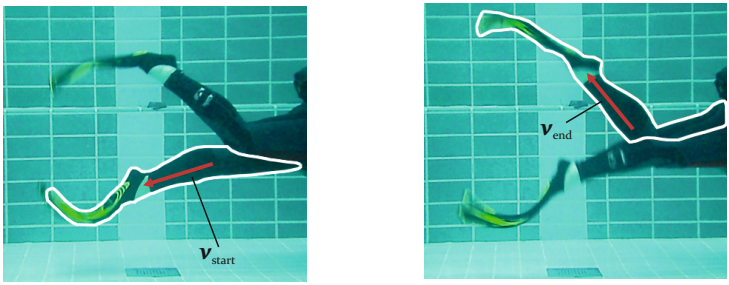

(a) left leg at t_{down} (b) left leg at t_{up}

Figure 15: Fin kick motion and corresponding orientation vectors. The indicated vectors represent the shank's orientation at the turning points. The exemplary fin kick motion starts with the left leg down at t_{down} and ends with the left leg up at t_{up}. © 2015 IEEE, printed with permission, modified from [P1].

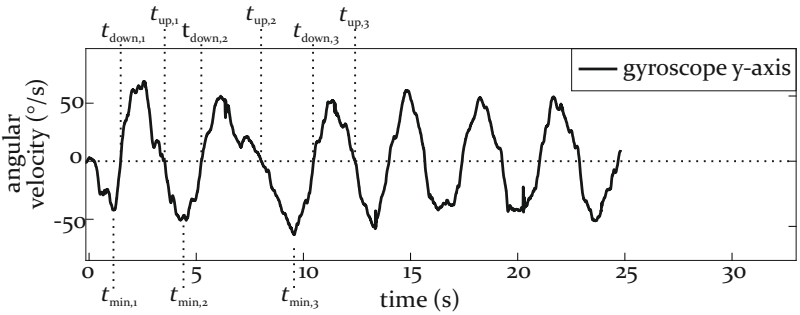

Figure 16: Analysis of the gyroscope y-axis (diver's frontal axis) during fin kicks. The time steps t_{down} and t_{up} indicate the turning point of the physical shank motion. © 2015 IEEE, printed with permission, modified from [P1].

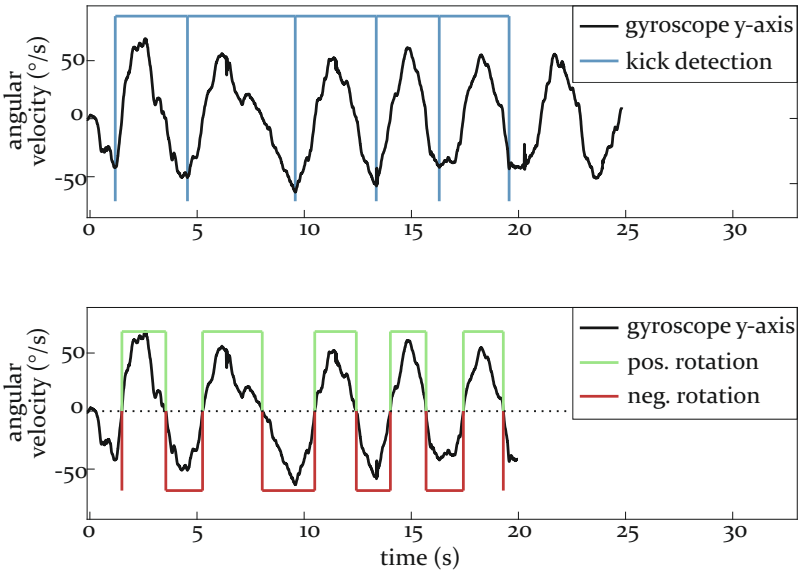

Figure 17: Two-step signal processing approach for the automated fin kick detection. First, the local minima were found with a subDTW-based algorithm. Then, the turning points between the kicks were determined by the zero-crossings of the signal. © 2015 IEEE, printed with permission, modified from [P1].

3.4.2 Shank orientation

Accelerometer-based absolute angle

The absolute shank angles relative to the ground were calculated for all previously determined turning points. During these turning points, a resting state instant was assumed. Hence, the absolute inclination angle $\theta_{\text{shank,abs}}$ was calculated based on the gravity measurement with Eq. 20, as previously described for the upper body analysis in Section 3.3.

Gyroscope-based relative angle

In contrast to the absolute angle calculation, the gyroscope-based approach provided the covered angle between start and end of a fin kick. For the computation, two vectors were defined: $\boldsymbol{v}_{\text{start}}$ and $\boldsymbol{v}_{\text{end}}$. The vectors represented the shank orientation before and after the fin kick performance

(see Fig. 15). The goal was to determine the angle between both vectors for each kick. For matters of simplicity, $\boldsymbol{v}_{\text{start}}$ was defined to

$$\boldsymbol{v}_{\text{start}} = \begin{pmatrix} 1 \\ 0 \\ 0 \end{pmatrix}. \tag{21}$$

A rotation matrix $\boldsymbol{R}^{\text{end}}_{\text{start}}$ was computed with the three-axes gyroscope data and a quaternion-based integration approach, as described in Section 2.2.2. The second vector $\boldsymbol{v}_{\text{end}}$ was then established by rotating $\boldsymbol{v}_{\text{start}}$ according to $\boldsymbol{R}^{\text{end}}_{\text{start}}$, with

$$\boldsymbol{v}_{\text{end}} = \boldsymbol{R}^{\text{end}}_{\text{start}} \cdot \boldsymbol{v}_{\text{start}}. \tag{22}$$

For the subsequent camera-based evaluation, the relative angle between both vectors from the camera's perspective was required. Hence, the resulting vector $\boldsymbol{v}_{\text{end}}$ was projected onto the sagittal plane, i.e., the x-z-plane of the diver's coordinate system. The relative angle $\theta_{\text{shank,rel}}$ was computed with the corresponding x- and z-components of $\boldsymbol{v}_{\text{end}}$:

$$\theta_{\text{shank, rel}} = \arctan\left(\frac{v_{\text{end,z}}}{v_{\text{end,x}}}\right). \tag{23}$$

3.4.3 Evaluation

The first part of the evaluation focused on the automated detection of the fin kicks. All kicks were manually labeled in the gyroscope signal. However, not all performed kicks could be included in the evaluation due to incorrectly performance (e.g., other fin kicks than the required typical flutter kick movement). After excluding the incorrect performances, a total number of 630 fin kicks were used in the evaluation. By separation of left and right leg, 1260 kicks could be analyzed. A kick was rated as successfully detected if the segmentation was performed within a five sample range (0.025 s) around the manually labeled turning points.
In the second part, the determined absolute and relative shank angles $\theta_{\text{shank, abs}}$ and $\theta_{\text{shank, rel}}$ were evaluated. Both methods were compared to the camera-based ground truth angles with ($\theta_{\text{gt}} - \theta_{\text{IMU}}$), which were established by manual analysis with the Kinovea video software. This was performed separately for left and right leg and for the three different

intervals: slow motion with low amplitude, strong motion with high amplitude and self-defined style.

3.5 Results

3.5.1 Upper body analysis

The evaluation of the upper body angle θ_{body} for the resting poses revealed a mean error of 0° with a standard deviation of 11°.

3.5.2 Fin kick analysis

The automated fin kick detection algorithm successfully identified 1063 of the 1260 analyzed kicks. There was no false positive match. This results in a precision of 100.0 % and a recall of 84.4 %.
The shank angle determination was evaluated for the accelerometer-based absolute and the gyroscope-based relative calculation. The results for both methods are summarized in Tab. 1 separately for left and right leg and for the three fin kick interval styles. Averaged over both legs and all intervals, the evaluation showed an error of $0° \pm 11°$ for the accelerometer-based absolute and $0° \pm 8°$ for the gyroscope-based relative angle.

3.6 Discussion

3.6.1 Discussion of results

The subDTW-based segmentation algorithm shows promising results regarding the precision of 100.0 %, considering that the template was selected randomly only once for all subjects. Subject-specific templates could potentially increase the achieved recall due to less false negative detection. Furthermore, the template could be averaged over several kicks instead of selecting one single kick randomly.
The orientation evaluation led to a similar accuracy for the upper body and the fin kick analysis, with both the accelerometer- and the gyroscope-based method. The mean error was evaluated to be 0° in all cases with a standard deviation between 8° and 11°. These results show that there was no systematic error in the measurement process. However, the standard deviation of up to 11° is considerable high. A possible reason could be an unstable calibration due to the temperature change from the dry to the underwater environment. In addition, the manually labeled ground truth

Table 1: Results of the shank orientation evaluation. The absolute and relative shank angles were compared to the video-based ground truth. The results are summarized by the mean error and standard deviation. © 2015 IEEE, printed with permission, modified from [P1].

	absolute angle (°) mean ± std		**relative angle** (°) mean ± std	
	left	**right**	**left**	**right**
low kicks	1 ± 8	0 ± 8	1 ± 5	1 ± 8
high kicks	−2 ± 10	−1 ± 17	0 ± 9	−1 ± 13
self-defined kicks	−1 ± 8	1 ± 11	1 ± 5	0 ± 5
	−1 ± 9	**0 ± 13**	**0 ± 7**	**0 ± 9**
	0 ± 11		**0 ± 8**	

could influence the accuracy. The camera's low image quality of single frames (see Fig. 14) and the ambiguity of manually selecting frames for the evaluation in the video analysis tool possibly led to minor deviations in the ground truth orientation.

3.6.2 Impact and application

The proposed algorithms for rotation and orientation determination were successfully demonstrated by measuring the upper body and shank angles. Moreover, more extended full-body analyses are feasible with only minor adaptations. The resulting system could then be used for further research and development, such as a sports science-related analysis of scuba diving, the underwater localization of divers and the development and enhancement of scuba diving gear.
The focus of a sports science-related analysis could consider several joint angles, hence, the pose of the diver, and incorporate additional kinematic features (e.g., the velocity). In addition to the diver's kinematics, further input, such as biomedical data (e.g., electrocardiography (ECG) measurements [176, 177]), depth and water specification could be considered. The combination of these parameters could be processed to optimize the diver's pose and velocity depending on biomedical and environment factors. Further studies could deal with the water flow characteristics depending on the shank and fin orientation. The application of underwater localization can benefit from the orientation data by combining already available range or distance information with the diver's orienta-

tion (as shown in [77]) and can additionally be improved by the knowledge of the diver's motion behavior. Such a localization system could then be developed as a customer product for the localization of fellow divers in the same group. Further development and enhancement could result from the aforementioned sports science analysis. Based on the measured kinematics, current environment and also the diver's habits and motion behavior, adaptable and personalized items, such as customized fins or wet suits, could be designed.

3.6.3 Possible improvements

Before reaching these goals, several modifications and improvements have to be considered. Improvements regarding ongoing research could contain a more reliable ground truth and a temperature-compensated calibration. The ground truth data of this study were based on a manual labeling process in 2D-space. A reliable 3D-motion capture system could be incorporated instead. Furthermore, the change of temperature between the dry environment during calibration and the underwater environment during application has to be considered (see Sections 2.1.2 and 5.2.2).
For follow-up studies and gear development, the hardware components have to be easily applicable. Whereas the described underwater installation showed robust results in this study, the hardware preparation would be too complex for an application of daily use. Furthermore, the current system stores the data on the IMU hardware for further processing, which does not meet the requirements for a real-time application. As a result, further hardware simplification is necessary, either by developing a scuba diving-fitted underwater system or by incorporating available waterproof IMU solutions, including an underwater data transmission.

4 Rowing: Stroke Detection and In-Stroke Boat Rotation Determination

In this chapter, automated methods for kinematic analysis of the in-stroke boat rotation are proposed. The in-stroke boat rotation in rowing has significant impact on the velocity and the overall rowing performance. However, current analysis methods mostly rely on visual assessment and semi-automated rotation estimation that do not allow for a continuous analysis during training or competition. In the literature, there is no approach for the combination of an automated stroke detection and the subsequent analysis of the boat rotation, which would be necessary for a continuous in-stroke rotation calculation. In this thesis, two aspects are covered: an automated detection of performed rowing strokes and the determination of the in-stroke rotation of the rowing boat. Based on the attachment of one IMU per boat, measurements are obtained for both professional and amateur rowing scenarios. Rowing strokes are detected automatically with a stroke segmentation algorithm. The stroke timing is then applied to extract the rowing boat rotation during single strokes. The resulting in-stroke rotation angles are evaluated against known literature values. The content of this chapter was published in [P2] and [P3].

4.1 Data acquisition

The study was divided into two parts: with data from professional athletes during a rowing competition and with data from amateur athletes during training scenarios. The hardware setup and study design differ for both parts regarding the data contents and aims. A summary is provided in Tab. 2.

4.1.1 Hardware setup

Study part 1: professional data

The sensor hardware was integrated in the on-board tracking device, which is obligatory for all boats in most professional (international) rowing competitions. The tracking device was attached to the bow of the boat

Table 2: Overview of data acquisition components with the hardware setup and aim of each study part.

study part	hardware	aim
study part 1: professional data	Analog Devices ADXL330 (accelerometer)	rowing stroke detection
study part 2: amateur data	miPod IMU (accelerometer, gyroscope)	rowing stroke detection boat rotation calculation

in a waterproof case. It contained the three-axes accelerometer ADXL330 with a range of ± 3 g and a sampling rate of 50 Hz (see Section 2.1.4).

Study part 2: amateur data

For the data acquisition during training scenarios, the miPod sensor hardware ([137], see Section 2.1.4) was employed. The miPod was used as IMU and will therefore be referred to as 'inertial sensor' or 'IMU' in this chapter. The ranges were configured to ± 8 g (accelerometer) and $\pm 1000 \frac{°}{s}$ (gyroscope). The sampling rate was set to 200 Hz. One IMU was mounted per boat. For reasons of water protection, it was placed in the cavity of the boat, in the proximity of the center (depending on the type of boat). The IMU attachment in the double *scull* is presented in Fig. 18.

4.1.2 Study design

Study part 1: professional data

The aim of the first part of the study was to implement and validate an algorithm for the detection of single rowing strokes in professional competitions.
The data acquisition took place on the regatta course of Linz-Ottensheim (as part of the Danube river), Austria, during the U23 World Championship 2013. The analysis of this study part focused on two boat classes: single *scull* (1x) and *coxed* eight (8+). These two classes were supposed to represent the extrema of all boat classes regarding size, maximum velocity and motion behavior. In order to include a wide variety of data, several races were obtained for both men and women: *heat*, *repechage*, semifinal and final. A detailed overview of all race types and the corresponding number of single rowing strokes is provided in Tab. 3.

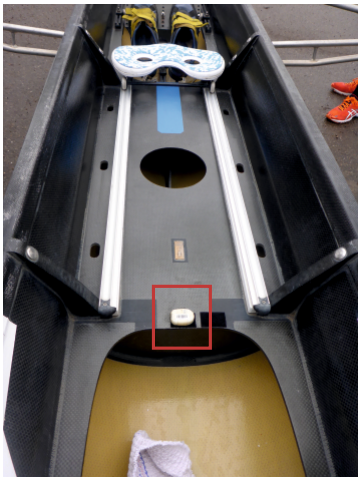

Figure 18: IMU attachment inside the boat cavity. © 2019 Springer, printed with permission [P3].

Study part 2: amateur data

The aim of the second part of the study was to evaluate if the proposed algorithm for stroke detection based on professional data also works reliably for the application to training scenarios. In addition, the extracted stroke data were further processed in order to calculate the 3D-rotation of the boat during stroke performance.
The data acquisition of the training scenarios took place in Waiblingen, Germany, on the Rems river. It contained training runs of four boat classes, including up to nine participants. The boat classes were single *scull* (1x), double *scull* (2x), quadruple *scull* (4x) and *coxed* eight (8+). For each of these classes, several intervals of rowing motion were performed. Their duration varied between 20 s and 60 s. For reasons of later comparison, four intervals per boat class were selected. The boat classes and corresponding number of total strokes for all intervals are summarized in Tab. 4.

Table 3: Analyzed race types for professional data sets (study part 1). © 2019 Springer, printed with permission, modified from [P3].

ID	boat class	race type	strokes
	single *scull*		
P1	- lightweight, women (LW1x)	*heat*	247
P2	- men (M1x)	*repechage*	246
P3	- lightweight, men (LM1x)	quarter final	221
P4	- women (W1x)	semifinal	265
P5	- lightweight, women (LW1x)	final	277
P6	- men (M1x)	final	227
	coxed eight		
P7	- men (M8+)	*heat*	223
P8	- women (W8+)	*repechage*	240
P9	- women (W8+)	final	257
P10	- men (M8+)	final	222

Table 4: Analyzed race types for amateur data sets (study part 2). © 2019 Springer, printed with permission, modified from [P3].

ID	boat class	intervals	strokes
A1	single *scull*, men (M1x)	4	48
A2	double *scull*, men (M2x)	4	54
A3	quadruple *scull*, men (M4x)	4	39
A4	*coxed* eight, mixed (M/W8+)	4	38

Before the actual acquisition, a sensor calibration was performed, including static positions on each of the six sensor sides and rotations about each of the three sensor axes. All participants were informed of sports-related risks and gave written consent to participate in the study and for the collected data to be published.

4.2 Calibration

For the acquisition with professional athletes, it was required to interference as little as possible with the competition. Therefore, a calibration of the ADXL330 accelerometer was not feasible in study part 1. For the training scenarios with amateurs in study part 2, there were less constraints

and the IMU was calibrated following the algorithm of Ferraris et al. [40] (see Section 2.1.3).

4.3 Rowing stroke detection

4.3.1 Template-based detection

The rowing stroke detection was performed with the template-based matching algorithm DTW [174]. Due to the repetitive nature of the strokes in the rowing motion, the algorithm's extension for continuous template recognition subDTW [175] was applied.
The processing of the 1D-acceleration signal of the axis in motion direction was assumed to be sufficient for a robust segmentation in single strokes, given that the rowing motion basically follows a straight line. For the template selection, one randomly chosen rowing stroke was extracted from the acceleration signal of the race data. The stroke was selected manually from the middle part of the race in order to obtain a representative template without any additional acceleration effects, which are typical for the start and end phase of a race. A stroke was defined to start at the point with the highest negative acceleration, produced by placing the blade in the water (the so-called '*catch*') before the accelerating *drive phase* begins [85]. An example of three consecutive strokes of a professional race (P5: LW1x, final) is presented in Fig. 19. The defined separation between the strokes is indicated with dotted lines. One selected template was applied to the acceleration signals of all data set. For the professional races, each signal contains between five and eight minutes of data (depending on the race). In order to allow for a possible later real-time implementation and to decrease computation time, the signal was analyzed incrementally. The complete data set of one race was subdivided into intervals of 5 s to 15 s before applying the subDTW-based algorithm to each interval. An overlap of 4 s between consecutive intervals was implemented to avoid the loss of divided strokes. After the subDTW performance, all intervals were combined to the full acceleration signal, including the determined stroke timing. For the amateur data with a duration of less than one minute per interval, no previous subdivision of the signals was necessary.
Both the template and the signal were filtered with a moving average low-pass filter with a time span of 0.4 s before applying the subDTW-based algorithm. The algorithm was further modified to the rowing-specific scenario. The internal threshold for stroke output was set to a value of 250

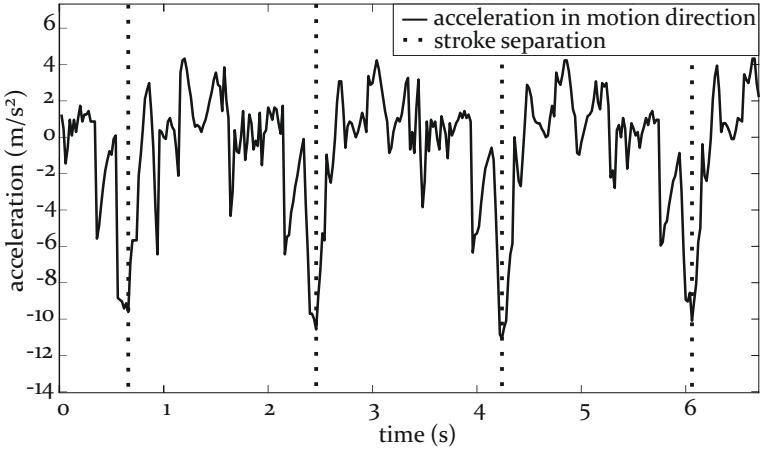

Figure 19: Example acceleration signal of three consecutive rowing strokes of race P5: LW1x, final. The defined separation between the strokes is indicated with dotted lines. © 2019 Springer, printed with permission [P3].

in order to avoid detecting irrelevant patterns. In addition, a minimum stroke duration was implemented and set to 0.8 s. All shorter detections were assumed not to be (correctly performed) rowing strokes and hence, were removed from the subDTW output.

4.3.2 Evaluation

The performance of the subDTW-based stroke detection was evaluated by manual signal analysis for both the professional and the amateur data. However, the templates were only extracted from professional data in order to further analyze the robustness of the algorithm.

Professional data

The evaluation for the application to professional data was performed with the ten available race data sets (see Tab. 3). One template was extracted from each of the races and applied to all ten data sets. The resulting precision and recall were computed for all combinations and subsequently averaged.

Amateur data

The ten previously selected templates of the professional data were applied to all amateur data sets (see Tab. 4). Precision and recall were computed for all combinations and subsequently averaged.

4.4 Rotation determination during rowing strokes

4.4.1 Quaternion-based integration

The in-stroke rotation of the boat was calculated with the 3D-gyroscope signal. The gyroscope signal was processed with a quaternion-based integration method that provided a simultaneous integration of the full 3D-signal, assuming a linear motion in between sampling steps (see Section 2.2.2). The resulting rotation for the selected interval was then transformed to Euler angle representation for evaluation.

4.4.2 Evaluation

The proposed algorithm for IMU-based rotation determination was built on the previously described stroke detection, i.e., all strokes that were detected by the algorithm were automatically processed for angular evaluation. In order to avoid processing of erroneous stroke detection results and including non-stroke events, it was relevant to perform the evaluation of the rotation determination on only correctly detected strokes. The evaluation of the stroke detection revealed that the template selection of race P9 (W8+, final) led to a precision of 100.0 % for all amateur data sets (see results in Tab. 7). Hence, the corresponding template was chosen for the evaluation.
All strokes were processed separately, combined subsequently and processed in order to obtain the resulting average range for yaw, pitch and roll angle. The average range with mean and standard deviation, as well as the minimum and maximum range, were computed individually for all included boat classes.
The evaluation was performed by comparing the resulting angular rotation ranges to known values from the literature. Loschner et al. [94] provided 3D-gyroscope-based measurements of multiple elite level athletes in single *scull* boats. Their results for the mean range and standard deviation were $0.5^\circ \pm 0.164^\circ$ (yaw, ϕ_{losch}), $0.2^\circ \pm 0.062^\circ$ (pitch, θ_{losch}) and

Table 5: Literature values for angular boat rotation ranges. © 2019 Springer, printed with permission, modified from [P3].

source	details	boat rotation ranges		
		yaw	pitch	roll
Loschner et al. [94]	gyroscope data, elite level 13 single *scull* athletes	0.5°	0.2 °	1.7°
Sinclair et al. [92]	boat displacement, adv. to elite level 11 single *scull* athlete	0.04°	0.28°	0.36°
Serveto et al. [90]	accelerometer data	–	0.73°	–

1.7° ± 0.051° (roll, ψ_{losch}). Sinclair et al. [92] presented their results on boat rotation for the single *scull* class with advanced to elite level athletes. The rotation was presented by means of vertical and horizontal displacement: 0.003 m horizontal displacement of the stern (yaw), 0.02 m vertical displacement of the bow (pitch) and 0.005 m vertical displacement of the oarlock pin (roll). Based on an average length of a single *scull* boat of 8.2 m and the estimated distance between the oar locks of 1.6 m, the literature values were transformed to ϕ_{sincl} = 0.04° (yaw), θ_{sincl} = 0.28° (pitch) and ψ_{sincl} = 0.36° (roll). Serveto et al. [90] compared their model-based calculations to actual accelerometer-based measurements of the pitch angle. Their measured pitch angle θ_{serv} ranges approximately from – 0.45° to + 0.28°. An overview of existing and suitable literature with the corresponding rotation ranges is provided in Tab. 5.

4.5 Results

4.5.1 Rowing stroke detection

Professional data

The resulting precision and recall for all evaluated template-signal combinations are provided in Tab. 6. The average over all combinations leads to an overall precision of 0.998 and recall of 0.997.

Table 6: Results of the stroke detection evaluation for professional data. One stroke was selected from each race and used for the subDTW-based detection of all other races. The results are presented by precision and recall.

		template									
	prec. recall	P1	P2	P3	P4	P5	P6	P7	P8	P9	P10
signal	P1	1 1	0.996 0.996	1 1	1 0.988	1 0.976	1 0.996	0.996 0.996	0.996 0.996	0.996 0.996	0.996 0.996
	P2	0.988 0.988	1 1	1 1	1 0.996	1 0.996	0.996 0.996	1 1	1 1	1 1	1 1
	P3	1 1	1 1	1 1	1 0.995	1 0.995	0.995 0.995	1 0.995	1 1	1 0.995	1 1
	P4	0.992 0.992	1 1	0.996 0.996	1 1	1 1	1 1	1 1	1 1	1 1	0.996 0.996
	P5	1 1	1 1	0.996 0.996	0.996 0.996	0.996 0.996	0.996 0.996	1 1	0.996 0.996	0.996 0.996	1 1
	P6	0.874 0.859	1 1	1 1	1 0.996	1 0.996	1 1	1 1	1 1	1 1	1 1
	P7	1 1	1 1	1 1	1 1	1 1	1 1	1 1	1 1	1 1	1 1
	P8	1 1	1 1	1 1	1 1	1 1	1 1	1 1	1 1	1 1	1 1
	P9	1 1	1 1	1 1	1 1	1 1	1 1	1 1	1 1	1 1	1 1
	P10	1 1	1 1	1 1	1 1	1 1	1 1	0.995 0.995	1 1	0.995 0.995	0.995 0.995

Amateur data

The resulting precision and recall for all evaluated combinations of templates from professional and signals from amateur data are provided in Tab. 7. The average over all combinations leads to an overall precision of 0.972 and recall of 0.904.

4.5.2 Rotation determination

The results for the in-stroke angular rotation range for yaw, pitch and roll angle are presented in Tab. 8. The average over all four data sets was calculated to the mean and standard deviation values of $0.92° \pm 0.92°$ (yaw), $0.48° \pm 0.11°$ (pitch) and $2.43° \pm 0.99°$ (roll).

Table 7: Results of the stroke detection evaluation for amateur data. One stroke was selected from each professional race and used for the subDTW-based detection of all amateur data. The results are presented by precision and recall.

		template									
	prec. recall	P1	P2	P3	P4	P5	P6	P7	P8	P9	P10
signal	A1	0.848 0.813	0.957 0.938	0.958 0.958	0.933 0.292	0.909 0.417	0.979 0.958	0.633 0.396	0.939 0.958	1 0.938	0.977 0.875
	A2	0.960 0.889	0.981 0.963	1 1	1 0.963	1 1	1 1	1 0.944	1 1	1 1	0.981 0.963
	A3	0.909 0.769	1 1	1 1	1 1	1 1	1 1	1 0.923	1 1	1 1	1 1
	A4	0.929 0.684	0.970 0.842	1 1	1 1	1 1	1 0.947	1 0.895	1 1	1 1	1 0.842

Table 8: Results of the rotation evaluation with the in-stroke ranges for yaw, pitch and roll angles for all four amateur data sets. © 2019 Springer, printed with permission, modified from [P3].

	yaw range (°)			**pitch range** (°)			**roll range** (°)		
ID	**min**	**max**	**mean ± std**	**min**	**max**	**mean ± std**	**min**	**max**	**mean ± std**
A1	0.22	7.17	0.97 ± 1.20	0.25	0.73	0.45 ± 0.12	1.06	4.41	2.31 ± 0.86
A2	0.15	5.04	0.80 ± 0.83	0.41	0.85	0.59 ± 0.09	1.38	7.40	2.79 ± 1.27
A3	0.16	2.89	0.92 ± 0.61	0.31	0.73	0.52 ± 0.10	0.91	4.40	2.22 ± 0.84
A4	0.18	5.00	1.00 ± 0.94	0.20	0.73	0.37 ± 0.14	0.94	4.51	2.39 ± 0.91
			0.92 ± 0.92			**0.48 ± 0.11**			**2.43 ± 0.99**

4.6 Discussion

4.6.1 Discussion of results

The subDTW-based stroke detection with templates from professional rowing data led to accurate detection results for both the professional and the amateur data sets. With an average of 99.8 % (precision) and 99.7 % (recall) for the professional data, the results allow for further processing of the detected strokes. Only in one template-signal-combination, the results were slightly worse with 87.4 % (precision) and 85.9 % (recall). Both the template (race P1: LW1x, *heat*) and the signal (race P6: M1x, final) were from single *scull* races and no clear reason for this worse performance could be found. However, in a final application, it would be

feasible to create specific templates per boat class in order to overcome this limitation. In the evaluation of this study, the stroke detection with the template of the same class led to 100.0 % precision and recall in eight of ten boat classes and only one false positive and one false negative in the remaining two boat classes. Hence, the proposed algorithm for stroke detection can be applied to competitions with highly accurate results.
The average results for precision and recall with 97.2 % and 90.4 % for amateur data show that the proposed algorithm even performs successfully with templates from professional race data applied to amateur data in a completely different scenario. Although in some cases the recall dropped below 50 %, the overall trend indicates the similarity of all rowing strokes and the comprehensive performance of the template-based matching method. Analog to the discussion of the results for professional data, also for the final application in amateur events, class-specific amateur stroke templates can be incorporated. The precision and recall can be expected to be considerable higher than the achieved results with professional stroke templates.
The rotation results show similar ranges between the four evaluated boat classes, which can be seen as first indicator for the robustness of the algorithm. Comparing these results to the literature values shows an increased yaw range, a comparable pitch range and a considerable higher roll range. The yaw angle range with an average of 0.92° exceeds the expected maximum value by 0.42°. The pitch angle range of 0.48° lies between the literature values of 0.2° and 0.73°. The roll angle with an average range of 2.43° exceeds the expected literature range by 0.73°. For the interpretation of the increased measurement ranges, it has to be considered that there was a difference in rowing level. Whereas the rotation calculation of this study was computed with data from amateur athletes, the literature values were mainly achieved with advanced/elite and elite level athletes (see Tab. 5). Although the measured angular rotation results exceed the available literature values, they can be assumed to still be in a reasonable range to be processed for supporting competitions, race broadcast and training scenarios.

4.6.2 Impact and application

The direct application of the stroke detection algorithm is the determination of the stroke rate. According to Kleshnev [178], the efficiency of the rowing performance depends, amongst others, on the stroke rate. Hence, a reliable stroke detection can be seen as the base for further sport

science-related analysis. One option of computing the continuous stroke rate from the proposed subDTW template matching method was established within the development of this algorithm and published in [P2]. Also, the stroke detection can be used for kinematic analysis, as presented in this thesis by the in-stroke rotation calculation. Further in-stroke analysis could be focused on the boat displacement during rowing strokes, the synchronicity between athletes or estimating the boat position based on the periodic rowing motion [P2].
The rotation calculation is first of all relevant for sport science research and training aspects, such as the motion asymmetry [81] and the boat's stability [91, 92]. Based on the proposed algorithm, already existing training methods could be automated and applied in real-time. With IMU-based measurements, supervised training scenarios are not limited to any camera-covered area or to direct visual contact between rowing coach and athletes.

4.6.3 Possible improvements

The subDTW-based algorithm was applied with randomly selected templates. It can be expected that a template that was generated from multiple strokes and possibly multiple crews would even lead to more robust results. Another influencing factor for the subDTW performance could be the motion velocity. Both in the professional race data and in the amateur data, the goal was to move in or at least close to maximum speed. In rowing training however, athletes could perform parts of the covered distance with slower rowing cycles. It can be assumed that based on the time-independent character of DTW, the influence of the motion velocity only has minor influence but this assumption would still have to be evaluated before an application to extended training scenarios.
Although the rotation calculation showed plausible results, there are possible uncertainties in the proposed methods. Based on mostly temperature-dependent changes of the gyroscope output, there is a (small) drift to be expected for each gyroscope-based rotation calculation (see Sections 2.1.2 and 5.2.2). Although the drift during single strokes with a duration of approximately 1.0 s to 1.5 s was assumed to be negligible in this study, there is still a small influence to be considered in the resulting rotation and angle calculation. A continuous adaptation of calibration parameters could fix the temperature-related deviations.
Another limitation of the rotation calculation is the omitted sensor-boat alignment. The sensors were attached by aligning them to visible patterns

on the boat, following visual judgment. In an ideal scenario, the sensors would either be perfectly aligned to the boat with specific hardware tools or with subsequently applied alignment methods (see Section 2.1.3).
Finally, for a more accurate validation of the proposed algorithm, the evaluation could be performed with actual ground truth data instead of a literature comparison. One option for a ground truth system is given by using a highly accurate motion capture system [179]. However, it has to be considered that covering the rowing motion of multiple strokes requires a wide measurement volume. Hence, a multitude of cameras would have to be incorporated. As an alternative to building up a motion capture system in a fixed position, a rolling motion capture system could be incorporated as suggested in [180, 181] an evaluated for rowing in [182].

5 Ski Jumping: Automated Ski Velocity and Jump Length Determination

In this chapter, automated methods for kinematic analysis in ski jumping are proposed. Ski jumping kinematics is traditionally determined with manual or semi-automated visual measurement methods. Although the advancing development of wearable systems provides possibilities for automated analyses, the application to ski jumping training and competitions remains challenging. In order not to distract the athletes, unobtrusive measurement methods without any interference with the jump procedure are required. In state-of-the-art publications, there are approaches for estimating ski jumping kinematics with inertial- and inertial-magnetic sensors. However, most of them either focused on biomechanical research or on feedback systems and thereby require full body measurements. These cannot be incorporated in standard training sessions and competitions without limitations or even disturbances of the athletes' routine. In this thesis, unobtrusive kinematic analysis methods are presented. Measurements are obtained from IMMUs that are only attached to the athletes' skis. An automated jump phase segmentation is introduced and incorporated into the calculation of the ski orientation in all phases. The ski orientation is further processed in order to determine the continuous ski velocity and jump length. The jump phase segmentation and the calculation of the velocity and jump length are evaluated against multiple ground truth systems. The content of this chapter was published in [P4] and [P5].

5.1 Data acquisition

5.1.1 Hardware setup

The data acquisition was performed with two miPod sensor devices ([137], see Section 2.1.4) per athlete. The devices were used as IMMUs in order to provide accelerometer, gyroscope and magnetometer data. One IMMU was attached to the left and one to the right ski (see Fig. 20). All devices were configured to an accelerometer range of $\pm$ 16 g, a gyroscope range of $\pm$ 2000 $\frac{^\circ}{s}$ and a magnetometer range of $\pm$ 1200 μT. The sampling rate was set to 200 Hz.

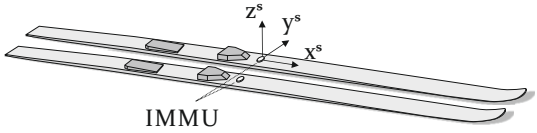

Figure 20: IMMU attachment to skis and the corresponding coordinate system. One IMMU was attached per ski in front of the binding. The illustrated coordinate system will be referred to as 'ski frame' $\boldsymbol{f}_s$. © 2017 ACM, printed with permission, modified from [P5].

For later evaluation, a multi-camera video system was set up stationary. It contained four synchronized cameras that were configured to record simultaneously. The cameras' positions were arranged to cover the start area at the top of the jumping hill (one camera), the take-off platform (one camera) and the landing area (two cameras). They were configured to a sampling rate of 100 fps with their maximum resolution of 640 × 480 pixels.

For synchronizing the IMMUs and the camera system, a specifically manufactured magnetic gate and a Cyclops light barrier pair [183] (response time: ± 0.5 ms) were included in the measurement setup. The magnetic gate contained four permanent magnets, which generated a magnetic field with an intensity significantly higher than the terrestrial magnetic field. The gate and the light barrier were both placed on the take-off platform, with a distance of 6 m to the end of the platform (see Fig. 21). Whenever an athlete passed that position, the magnetometer of the IMMU sensed a strong magnetic field that was represented by a distinct peak in the magnetometer signal. At the same time, the light barrier was triggered. The light barrier was connected to the multi-camera system and both were synchronized by the same time vector. Based on that, the IMMU measurement and the camera recording could be synchronized with the distinct peak in the magnetometer signal and the trigger time of the light barrier.

Furthermore, a second light barrier pair was built up at the end of the take-off platform, hence, with a distance of 6 m to the first one. The trigger times of both pairs were processed for each jump in order to calculate the take-off velocity. The resulting value was used as ground truth for later evaluation.

Figure 21: Take-off platform with magnetic gate and light barrier system. When an athlete passed the construction, four permanent magnets (two for the left, two for the right ski) produced a distinct peak in the magnetometer signal. Simultaneously, the light barrier was triggered. © 2017 ACM, printed with permission [P5].

5.1.2 Study design

The study was performed with 11 experienced athletes (all male, age (years): 16 ± 1, height (cm): 176 ± 9, weight (kg): 59 ± 6, jump experience (years): 10 ± 2). All subjects were aware of jump-related risks and the ski association gave written consent for the collected data to be published. The study contained two ski jumping training sessions, one in summer and one in winter season. Both sessions were performed in Oberwiesenthal, Germany, at the HS 106 Fichtelbergschanze [184].
Before attaching the IMMUs to the athletes' skis, both sessions were initiated with a preparation phase, in which a specified calibration procedure was performed. In this study, the calibration was necessary in particular due to possibly large temperature variations (see Section 2.1.3). The sensor hardware was placed in an outdoor environment in order to acclimatize to the outside temperature before starting the calibration process. Subsequently, the IMMUs were adjusted to the specifically manufactured calibration cube, which was put to a rotary table with adjustable stand (see Fig. 5). The cube was moved, following a predefined motion pattern, which contained static positions on each side and multiple rotations

about each sensor axis. Subsequently, one IMMU was attached to each ski, using VELCRO adhesive tape. The ski frame $\boldsymbol{f}_{\mathrm{s}}$ followed the definition of the sensor's x-axis representing the longitudinal, the y-axis the lateral and the z-axis the vertical axis of the skis (see Fig. 20).
After the sensors were attached to the skis, the training session started. The athletes were supposed to perform their training without any specific considerations of the sensors or the data acquisition. For a possible long-term application in training sessions or competitions, it was important that there was no involvement of the athletes necessary for the data acquisition.
Each training session contained two to six consecutive jumps. The exact number of jumps depended on the athlete and the training conditions. In total, the 11 athletes performed 34 jumps. However, due to IMMU device storage failures of two sensors of the left skis, some jumps could not be stored. As a result, data of all 34 jumps of the right but only data of 24 jumps of the left sensor were successfully stored. Without differentiation between left and right sensor, a total of 58 jump data sets were available for further processing. For later evaluation, all jumps were recorded with the multi-camera video system.

5.1.3 Definition of coordinate systems and jump phases

Two coordinate systems were defined: the previously described ski frame $\boldsymbol{f}_{\mathrm{s}}$ and the global frame $\boldsymbol{f}_{\mathrm{g}}$. Both frames are presented in Fig. 22. In the following, if not stated otherwise, all vectors and matrices refer to the global frame. If vectors $\boldsymbol{v}$ refer to the ski frame instead, they are marked with $\boldsymbol{v}^{\mathrm{s}}$. The rotation from the global to the ski frame $\boldsymbol{C}_{\mathrm{g}}^{\mathrm{s}}$ coincides with the orientation of the ski in the global system $\boldsymbol{C}_{\mathrm{ski},t}$ at time t.
For further processing, it was required to segment the jump scenario in several phases. Five phases were defined: rest (resting state before the start), straight inrun, radius, take-off preparation and flight. In between these phases, there were three relevant points of time: start of motion, take-off and landing. An overview of phases and times is provided in Fig. 22. It has to be pointed out that this phase segmentation does not follow the standard definition of the literature [96, 185], which would further subdivide the flight phase into e.g., early flight and stable flight. For the proposed pipeline of this study, it was not required to distinguish between these phases. Instead, a more detailed segmentation of the inrun (straight inrun, radius, take-off preparation) was considered. This

subdivision was necessary for a fully functional alignment between the ski and sensor frame, which was established to fulfill the requirement of unobtrusiveness of this work.

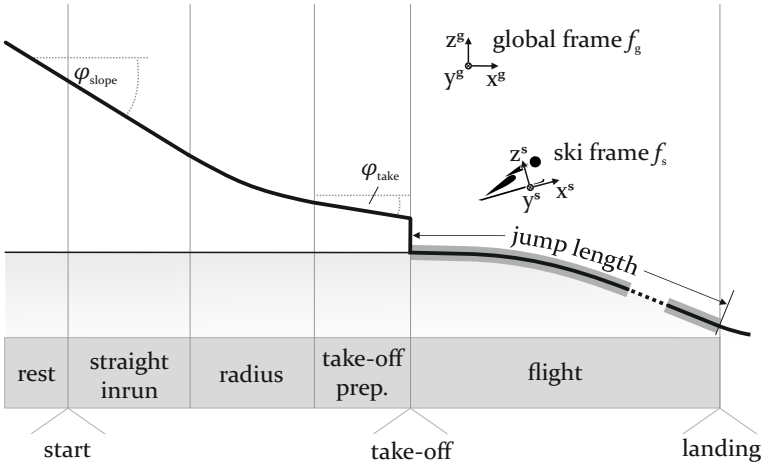

Figure 22: Jump phase overview. The vertical sections denote the jump phase definition of this study. The ski frame $\boldsymbol{f}_s$ and the global frame $\boldsymbol{f}_g$ are illustrated, as well as the employed jumping hill specifications for inclination angles and jump length. © 2017 ACM, printed with permission, modified from [P5].

5.2 Calibration

5.2.1 Standard calibration at application temperature

The calibration of accelerometer and gyroscope was based on the measurements of six static positions and rotations about all axes. With these data, both were calibrated following the algorithm of Ferraris et al. [40] (see Section 2.1.3). In contrast to the accelerometer and the gyroscope, the magnetometer was not used quantitatively but only for the synchronization with the light barrier and the camera system, respectively. Therefore, an accurate calibration was not necessary.

5.2.2 Analysis of temperature influence on calibration parameters

In this study, the hardware was acclimatized to the outdoor temperature, which was assumed to contain only little changes during the duration of the acquisition. However, in a final application of the proposed system, this acclimatization might not always be feasible or the outside temperature could change during the acquisition. To this end, an additional acquisition was performed with the aim of evaluating the temperature influence on the employed IMU devices. Similar to [127], multiple IMUs were set up in a climate chamber and calibrated with the previously described standardized calibration procedure with varying temperature. For reference, the complete calibration procedure was repeated with the same hardware but this time, in an environment with constant temperature. Hence, the calibration of the first acquisition part was influenced by variable temperature and time and the second part was only influenced by the time. Further possibly influencing factors were not considered in this study.

Data acquisition

Six miPod sensor systems ([137], see Section 2.1.4) were fixed to the calibration cube on the rotary table with adjustable stand (see Fig. 5).
In the first part, the calibration equipment was set up stationary in a climate chamber (see Fig. 23). The ambient temperature was initially set to 30 °C and incrementally decreased in 5 °C steps to a minimum temperature of – 25 °C. The calibration procedure with the sensor units in the cube was repeated for each temperature step, in total, 12 times. Due to the duration of cooling down the chamber, the time between subsequent calibration procedures was defined to 30 minutes, which led to a total acquisition duration of 5.5 hours.
In the second part, the influence of changing calibration parameters over temperature was supposed to be eliminated. Therefore, the calibration was repeated with identical hardware. However, in this part, the calibration equipment was set up stationary in a room with constant temperature between 18 °C and 19 °C. Analog to the first part, the calibration procedure was repeated 12 times with a pause of 30 minutes between consecutive repetitions.

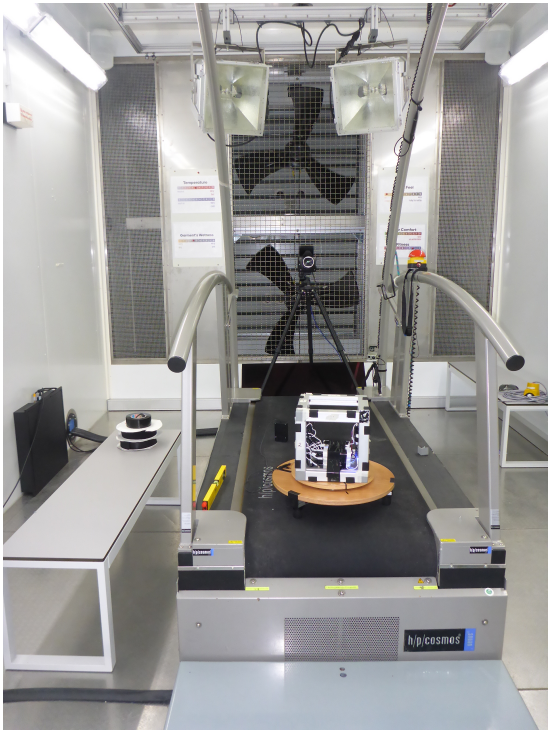

Figure 23: Calibration cube with IMU devices in climate chamber.

Evaluation and results

All relevant calibration parameters were calculated for all calibration runs. This includes the bias vector $\boldsymbol{b}$, the scale factor matrix $\boldsymbol{K}$ and the orientation matrix $\boldsymbol{R}$ (see Section 2.1.3) for both the accelerometer and the gyroscope. The bias values per sensor axis were directly obtained from the bias vector $\boldsymbol{b}$. The scale factors per axis were obtained from the principle diagonal of the scale factor matrix $\boldsymbol{K}$. The orientation matrix $\boldsymbol{R}$ was transformed to Euler angle representation in order to obtain rotation angles for all axes. In addition, the sampling frequency f was computed based on the device-internal temperature-compensated RTC.
All aforementioned parameters were visualized in a combined plot for both parts, i.e., for variable and for constant temperature. Example plots

Table 9: Influence of temperature and time on all evaluated calibration parameters. The provided values for the lowest and highest drift are visualized exemplarily in Fig. 24.

calibration parameter		drift with variable temperature		drift with constant temperature	
		lowest	highest	lowest	highest
$b_{a,x}$	$\left(10^{-3}\ \frac{\frac{m}{s^2}}{°C}\right)$	−6.273	−3.574	−0.044	0.331
$b_{a,y}$		−2.328	−1.498	−0.002	0.074
$b_{a,z}$		−16.779	0.429	−0.259	1.608
$b_{g,x}$	$\left(10^{-3}\ \frac{\frac{°}{s}}{°C}\right)$	−26.600	26.130	−1.278	1.507
$b_{g,y}$		−28.906	52.636	−1.209	1.575
$b_{g,z}$		−4.057	14.726	−0.928	6.711
$K_{a,x}$	$\left(10^{-5}\ \frac{1}{°C}\right)$	3.496	4.342	−0.511	0.579
$K_{a,y}$		3.409	3.905	−0.433	0.020
$K_{a,z}$		−1.279	4.495	−3.132	1.944
$K_{g,x}$	$\left(10^{-5}\ \frac{1}{°C}\right)$	−9.087	3.137	−2.055	2.237
$K_{g,y}$		−6.689	1.130	0.016	1.832
$K_{g,z}$		−9.385	1.096	−0.280	2.871
$R_{a,x}$	$\left(10^{-2}\ \frac{°}{°C}\right)$	−1.075	0.640	−3.036	3.314
$R_{a,y}$		−1.021	0.179	−3.229	2.931
$R_{a,z}$		−1.110	1.313	−9.412	7.146
$R_{g,x}$	$\left(10^{-2}\ \frac{°}{°C}\right)$	−1.198	0.590	−3.098	3.037
$R_{g,y}$		−1.078	0.112	−3.269	2.978
$R_{g,z}$		−0.957	1.498	−9.408	7.030
f	$\left(10^{-2}\ \frac{Hz}{°C}\right)$	−8.631	14.442	−0.433	0.222

for the calibration parameters $b_{g,x}$ (bias, gyroscope, x-axis) and $K_{a,y}$ (scale factor, accelerometer, y-axis) are provided in Fig. 24. The results for all calibration parameters are summarized in Tab. 9.
For the first part, the calibration parameters of all IMUs were plotted with their corresponding temperatures. The lowest temperature was considered as point of reference, i.e., although the lowest temperature in the climate chamber was −25 °C, the corresponding parameter value is visualized at ΔT = 0 °C. For simplified comparison between all IMUs, all parameters were normalized relatively to the first value, i.e., bias, rotation and frequency initiate with a difference of 0 ($\frac{m}{s^2}$ / $\frac{°}{s}$ / ° / Hz) and

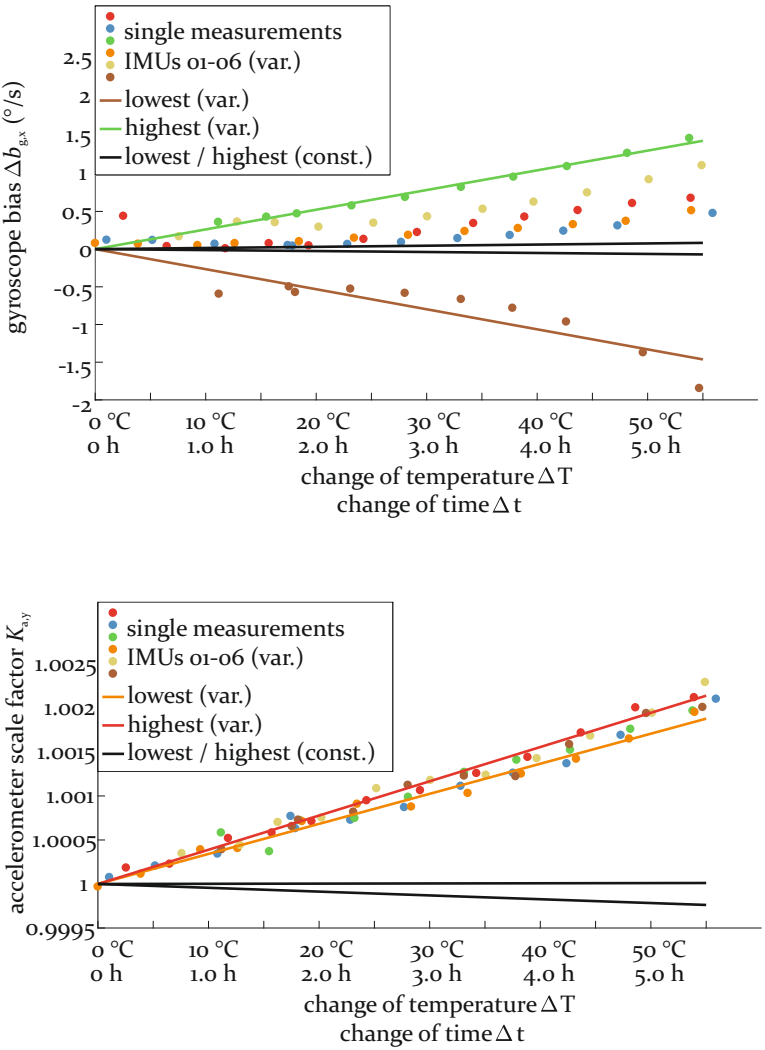

Figure 24: Influence of temperature and time on selected calibration parameters. All measurements over variable temperature (var.) are illustrated in the color of the corresponding IMU device. The colored lines show the lowest and highest drift. The black lines indicate the corresponding results for calibration with constant temperature (const.) over time.

the scale factor initiates with 1. Furthermore, the parameter values for each IMU were fitted linearly (least-square fit) to visualize the linearized drift. The resulting linear trends with the lowest and highest inclination are illustrated in the color of the corresponding IMU.
For the second part, the calibration parameters for constant temperature were processed in a similar way. Based on consistent duration between consecutive measurements in both parts, the resulting parameters could be processed for combined visualization with the change of time on the x-axis. For easier illustration, not all resulting parameters were plotted but only the fitted trends with the lowest and highest inclination. As a result, the highest influence of the variable temperature over time is shown by the colored lines and can be compared to the highest influence in the same period of time with constant ambient temperature by the black lines.

5.3 Phase segmentation

5.3.1 HMM-based segmentation

In order to automatically determine the defined jump phases, a segmentation algorithm was implemented. In consideration of possibly extending and adapting the algorithm with data of future acquisitions, a model-based approach, such as a hidden Markov model (HMM) [186], was preferred rather than a template-based approach, such as subDTW [174, 175].
Based on the hierarchical nature of the data, a hierarchical hidden Markov model (HHMM) [187] segmentation was implemented. The top hierarchical level consisted of the five defined jump phases (see Fig. 22). Each of them was designed to contain a further HMM with h hidden states. The top level jump phases were trained fully supervised, whereas the hidden states of the lower level HMMs were trained unsupervised. In order to represent the continuous nature of an actual ski jump sequence, all transitions were defined as forced left-to-right transitions [188]. This definition prevented the model to return to a previous state that was just left and forced the model to move to the next state of the sequence. In addition, forced alignment was implemented in order to start each sequence with the first state of the rest phase and end each sequence with the last state of the flight phase. In a previous study, an optimal number of hidden states h was empirically analyzed to be $h = 3$. Furthermore, suitable features were defined. These were the acceleration measure-

ments of the x- and z-axes, the gyroscope measurements of the y-axis, the gyroscope-integrated angle about the y-axis and the variances of all aforementioned features. The model was implemented with a Gaussian mixture model in order to represent the continuous data input. It was initialized with ten centers.
The supervised training of the top level phases was performed by simultaneous multi-camera video and manual sensor data analysis. However, for the transition between the inrun phases (straight inrun, radius, take-off preparation), there was no video recording available, so that these transitions were only trained with the manual sensor data analysis.

5.3.2 Evaluation

The most critical transitions for later processing of jump parameters were the ones with camera coverage: the start of the motion, take-off and landing. These video labeled transitions were used for the evaluation of the segmentation algorithm. The evaluation was performed with all 58 available data sets of the 11 athletes, without differentiation if the sensor was attached to the left or the right ski. The accuracy of the segmentation algorithm was determined by comparing the HHMM phase transition times $t_{\text{phase,HHMM}}$ to the video labeled ground truth $t_{\text{phase,gt}}$. The error was calculated by the mean and standard deviation of $(t_{\text{phase,HHMM}} - t_{\text{phase,gt}})$. For the evaluation, a LOSO-CV was performed, in which one subject represented one athlete.

5.4 Functional alignment

For accurately processing the acquired measurements, it was required that the sensor's measurement frame $\boldsymbol{f}_{\text{m}}$ was aligned with the ski frame $\boldsymbol{f}_{\text{s}}$. Due to the manual attachment of the sensors, a possible misalignment had to be assumed. To meet the requirement of unobtrusiveness, complex methods of alignment correction, containing one or more static positions, were not feasible. Hence, as an extension to the partially functional alignment of Chardonnens et al. [50], a completely functional alignment calibration was implemented.
In order to establish the 3D-rotation between the incorrect and corrected alignment, two known states were required (see Section 2.1.3). The two states incorporated in this study were the resting state before the start of the motion and the radius of the inrun. In the resting state, only the gravity components were measured with the accelerometer. The corre-

sponding vector is denoted by $\boldsymbol{a}^{s}_{\text{meas,rest}}$. In a correctly aligned sensor-ski system, the accelerometer measurements would exactly represent the orientation of the ski and hence, the inclination of the jumping hill φ_{slope} at the starting position (in this work: $\varphi_{\text{slope}} = 37.0°$ [184]). The corresponding expected acceleration vector is denoted by $\boldsymbol{a}^{s}_{\text{exp,rest}}$, with

$$\boldsymbol{a}^{s}_{\text{exp,rest}} = \begin{pmatrix} \sin(\varphi_{\text{slope}}) \\ 0 \\ \cos(\varphi_{\text{slope}}) \end{pmatrix}. \tag{24}$$

For the radius, the rotation per axis was calculated by integration of the gyroscope measurements. The corresponding vector of rotation angles was denoted by $\boldsymbol{\Omega}^{s}_{\text{meas,radius}}$. In a correctly aligned sensor-ski system, the complete rotation would be measured on the sensor's y-axis, which represents the ski's lateral axis. Hence, the overall measured rotation during the radius was projected to only the y-axis, resulting in the expected vector of rotation angles $\boldsymbol{\Omega}^{s}_{\text{exp,radius}}$, with

$$\boldsymbol{\Omega}^{s}_{\text{exp,radius}} = \begin{pmatrix} 0 \\ \left|\left|\boldsymbol{\Omega}^{s}_{\text{meas,radius}}\right|\right|_2 \\ 0 \end{pmatrix}. \tag{25}$$

The rotation between both measured and expected states was computed with a SVD, as described in Section 2.1.3. Subsequently, the established alignment rotation was applied to all corresponding data sets. Thus, all sensor measurements were represented in the ski frame $\boldsymbol{f}_{s}$, following the definition of Fig. 22.
The implemented algorithm was verified with simulated data in previous work and showed reliable results. The evaluation of the proposed alignment method with actual ski jumping data was not in the scope of this work. However, the alignment was indirectly verified by the evaluation of further processing steps that were based on the proposed alignment method.

5.5 Ski orientation

The ski orientation $\boldsymbol{C}_{\text{ski},t}$ at time t was calculated by integrating the gyroscope signal over time. As initial state, the ski orientation $\boldsymbol{C}_{\text{ski,init}}$ was

defined. This state was assumed to represent the orientation in the rest phase, with the slope inclination φ_{slope}. Subsequent rotations were calculated by a quaternion-based integration of the gyroscope measurements (see Section 2.2.2). The rotation of the ski system from t_{init} to t was represented by the quaternion $\boldsymbol{q}^{t}_{\text{init}}$. In order to establish the current ski orientation $\boldsymbol{C}_{\text{ski},t}$, the quaternion $\boldsymbol{q}^{t}_{\text{init}}$ was multiplied with the initial ski orientation:

$$\boldsymbol{C}_{\text{ski},t} = \boldsymbol{q}^{t}_{\text{init}} \cdot \boldsymbol{C}_{\text{ski,init}}. \tag{26}$$

Due to sensor noise, vibrations during the inrun and possible sensor drift, the accuracy could be assumed to decrease over time. In order to improve the accuracy, the known take-off platform inclination φ_{take} (in this work: $\varphi_{\text{take}} = 10.5^{\circ}$ [184]) was used to update the orientation at take-off. Hence, the ski orientation was calculated based on the slope inclination from start to take-off and based on the take-off platform inclination from take-off to landing:

$$\boldsymbol{C}_{\text{ski},t} = \begin{cases} \boldsymbol{q}^{t}_{\text{init}} \cdot \boldsymbol{C}_{\text{ski,init}} & \text{for } t \in [t_{\text{init}}, t_{\text{take}}) \\ \\ \boldsymbol{q}^{t}_{\text{take}} \cdot \boldsymbol{C}_{\text{ski,take}} & \text{for } t \in [t_{\text{take}}, t_{\text{land}}]. \end{cases} \tag{27}$$

5.6 Ski velocity

The ski velocity at time t was computed by integration of the accelerometer signal as proposed for strapdown inertial navigation in [189]. However, only the actual motion component of the accelerometer measurements $\boldsymbol{a}^{\text{s}}_{\text{motion},t}$ had to be considered and the gravity component $\boldsymbol{a}^{\text{s}}_{\text{grav},t}$ had to be eliminated. Based on the current ski orientation $\boldsymbol{C}_{\text{ski},t}$, the gravity component was calculated by rotating the earth gravity vector $\boldsymbol{a}_{\text{grav}} = [0, 0, g]^{\mathsf{T}}$ to the ski coordinate system at each time step t:

$$\boldsymbol{a}^{\text{s}}_{\text{grav},t} = \boldsymbol{C}_{ski,t} \cdot \boldsymbol{a}_{\text{grav}}. \tag{28}$$

The relevant motion component of the accelerometer measurement $\boldsymbol{a}^{\text{s}}_{\text{motion},t}$ was obtained by subtracting the gravity component from corresponding acceleration measurements. It was assumed that the resulting vector only contained relevant measurements that influence the velocity

of the ski. The ski velocity was computed by integration of $\boldsymbol{a}^{\mathrm{s}}_{\mathrm{motion},t}$ over time, including a possible prior velocity $\boldsymbol{v}^{\mathrm{s}}_{0}$:

$$\boldsymbol{v}^{\mathrm{s}}_{\mathrm{motion},t} = \boldsymbol{v}^{\mathrm{s}}_{0} + \int \boldsymbol{a}^{\mathrm{s}}_{\mathrm{motion},t}\, dt. \tag{29}$$

The absolute ski velocity v^{s}_{t} was obtained by the norm of the established velocity vector:

$$v^{\mathrm{s}}_{t} = \left|\left|\boldsymbol{v}^{\mathrm{s}}_{\mathrm{motion},t}\right|\right|_{2}. \tag{30}$$

Due to varying conditions during the inrun and the flight phase, Eq. 30 was further adapted and separated for the inrun phase from start to take-off and for the flight phase from take-off to landing. At the take-off platform, the velocity was updated with the light barrier measured velocity v_{lb}.

5.6.1 Ski velocity from start to take-off

The acceleration measurements during the inrun contained considerable high noise which can be explained by vibrations on the slope due to an uneven (snow-covered) surface. In order to reduce this influence, only the relevant component of the acceleration measurement was computed. Based on the known inrun orientation of the skis due to the constant contact between the skis and the track, it was assumed that only the acceleration vector component in motion direction (x-direction of the ski system, see Fig. 22) was relevant for the velocity development. As a result, only the x-component was processed and the y- and z-components were ignored for further computation:

$$\boldsymbol{v}^{\mathrm{s}}_{\mathrm{motion},t} = \int \begin{pmatrix} a^{\mathrm{s}}_{\mathrm{x,motion},t} \\ 0 \\ 0 \end{pmatrix} dt \quad \text{for } t \in [t_{\mathrm{init}}, t_{\mathrm{take}}). \tag{31}$$

5.6.2 Ski velocity from take-off to landing

After the take-off, no slope-related noise was measured. However, the path of the skis was not predetermined and hence, all acceleration components had to be processed. Furthermore, the velocity was updated based on the light barrier measured velocity v_{lb} in order to avoid the influence of possibly erroneous measurements of the inrun. Based on

the 1D-movement of the skis before the take-off, the velocity measured by the light barrier was considered to represent the velocity in the skis' x-direction only:

$$\boldsymbol{v}^{\mathrm{s}}_{\mathrm{motion},t} = \begin{pmatrix} v_{\mathrm{lb}} \\ 0 \\ 0 \end{pmatrix} + \int \boldsymbol{a}^{\mathrm{s}}_{\mathrm{motion},t}\, dt \quad \text{for } t \in [t_{\mathrm{take}}, t_{\mathrm{land}}]. \tag{32}$$

5.6.3 Evaluation

The computed ski velocity was evaluated in two ways: absolutely (in comparison to the light barrier measurement) and relatively (comparing left and right ski velocity during the flight phase of the same jump).
The absolute evaluation was performed by comparing the absolute velocity $v^{\mathrm{s}}_{t=t_{\mathrm{take}}}$ at take-off to the light barrier-based measurement v_{lb} with $(v^{\mathrm{s}}_{t=t_{\mathrm{take}}} - v_{\mathrm{lb}})$. The mean and standard deviation of the resulting error were calculated as average over all jumps. In addition, the error was set in relation to the average take-off velocity of all jumps (in this work: 25.0 $\frac{\mathrm{m}}{\mathrm{s}}$).
The relative evaluation considered the continuous velocity during the flight phase. The velocity development was evaluated over all jumps by obtaining the mean and standard deviation of the difference between the two ski measurements $(v^{\mathrm{s}}_{t,\mathrm{left}} - v^{\mathrm{s}}_{t,\mathrm{right}})$.
For the absolute comparison to the light barrier, all 58 jump data sets were evaluated without distinguishing between left and right ski. For the relative comparison between left and right ski, the 24 combined data sets with data from both skis were analyzed.

5.7 Jump length

5.7.1 Ski position in global system

The jump length determination was processed with previously obtained parameters: the exact time for take-off and landing, the ski orientation, the ski motion acceleration and the ski velocity. Based on these parameters, the ski's global position $\boldsymbol{x}_t$ at each time t could be calculated by applying the motion model of accelerated movements:

$$\boldsymbol{x}_t = \boldsymbol{x}_{t-1} + \boldsymbol{C}_{\mathrm{ski},t}{}^{-1} \cdot \left[\boldsymbol{v}^{\mathrm{s}}_{\mathrm{motion},t-1} \cdot dt + \frac{1}{2} \cdot \boldsymbol{a}^{\mathrm{s}}_{\mathrm{motion},t-1} \cdot dt^2\right]. \tag{33}$$

5.7.2 Transformation to jumping hill-specific jump length

The jump length in ski jumping is defined by the Standards for the Construction of Jumping Hills [190] as the distance on the ground w from the end of the take-off platform to the landing position (see Fig. 22). For later evaluation, the ski's landing position in the global frame $\boldsymbol{x}_t$ with $t = t_{\text{land}}$ was processed for the determination of the actual jump length w_{land}. A mathematical model was derived in order to relate the horizontal component (in direction of the global x-axis) of the calculated landing position $x_{\text{x},t=t_{\text{land}}}$ to the jump length w_{land}.
The points P, K and L define the landing slope of each jumping hill. Depending on the specific jumping hill layout, their positions vary but are always located on the landing slope. For these points, the jump lengths $w(\text{P})$, $w(\text{K})$ and $w(\text{L})$ are known based on the hill certificate [184]. In addition, their horizontal positions in the global system $x_{\text{x}}(\text{P})$, $x_{\text{x}}(\text{K})$, $x_{\text{x}}(\text{L})$ can be established by Eq. 34 [190] with the jumping hill specific parameters n, r_{L}, β_{P}, β and β_{L}.

$$\begin{aligned} x_{\text{x}}(\text{P}) &= n - r_{\text{L}} \cdot (\sin\beta_{\text{P}} - \sin\beta) \\ x_{\text{x}}(\text{K}) &= n \\ x_{\text{x}}(\text{L}) &= n + r_{\text{L}} \cdot (\sin\beta - \sin\beta_{\text{L}}) \end{aligned} \tag{34}$$

With the relation between the known horizontal positions x_{x} and the corresponding distances on the ground w for P, K and L, a mathematical model for the jump length transformation was established. The required jump length w_{land} was then computed for all evaluated jumps based on linear interpolation between the known jump length values for the positions of P, K and L.

5.7.3 Evaluation

The evaluation was performed with all 58 available data sets of the 11 athletes, without differentiation if the sensor was attached to the left or the right ski. For the establishment of ground truth data, the two cameras in the landing area were incorporated. The camera frames were analyzed manually with Kinovea video software [173]. The frame at the landing instant was overlaid with a measurement grid to support the video-based jump length determination (see Fig. 25).

The calculated jump length w_{land} was compared to the manually established labeled ground truth jump length w_{gt} with ($w_{land} - w_{gt}$). The mean and standard deviation of the error were calculated for all jumps. Furthermore, the resulting error was set in relation to the average jump length of all jumps (in this work: 84.5 m).

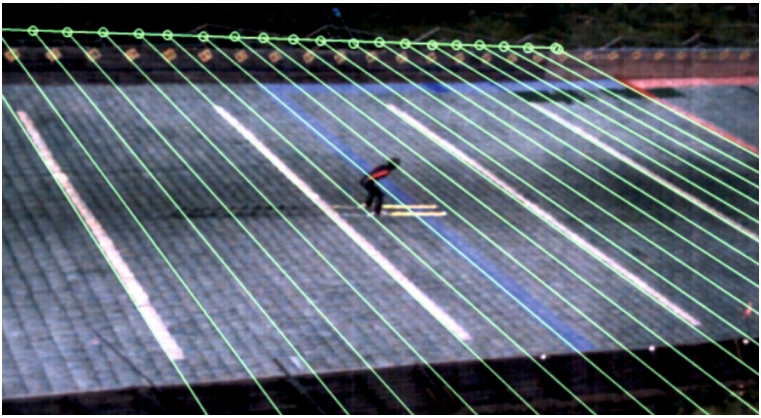

Figure 25: Ground truth jump length determination based on manual video analysis with Kinovea video software. © 2017 ACM, printed with permission [P5].

5.8 Results

Due to device failures during the data acquisition, not all recorded data could be used for all parts of the evaluation. The number and type of data are stated in each corresponding evaluation section and summarized in Tab. 10. Furthermore, the table contains a short description of the evaluation procedure and the corresponding results.

5.8.1 Phase segmentation

The deviation of the HHMM-based phase segmentation to the video-labeled ground truth is provided in Tab. 11.

Table 10: Overview of evaluation procedure, corresponding data sets and results. © 2017 ACM, printed with permission, modified from [P5].

content	procedure	data sets	result
phase segmentation	validation of HHMM-segmented jump phases against video labeled data	24 left 34 right	see Tab. 11
ski velocity (absolute)	validation against ground truth data of light barrier system at take-off platform	24 left 34 right	$-0.78\,\frac{\mathrm{m}}{\mathrm{s}} \pm 1.18\,\frac{\mathrm{m}}{\mathrm{s}}$ $(-3.0\,\% \pm 4.7\,\%)$
ski velocity (relative)	comparison of left and right ski sensor during flight phase	24 both	$0.40\,\frac{\mathrm{m}}{\mathrm{s}} \pm 0.96\,\frac{\mathrm{m}}{\mathrm{s}}$
jump length	validation against ground truth data of camera system at landing instant	24 left 34 right	$0.8\,\mathrm{m} \pm 2.9\,\mathrm{m}$ $(0.9\,\% \pm 3.4\,\%)$

Table 11: Results of the jump phase segmentation evaluation. The calculated transition times were analyzed in comparison to the video labeled ground truth. © 2017 ACM, printed with permission, modified from [P5].

	start of motion	take-off	landing
mean (s)	0.01	−0.01	0.00
std (s)	0.83	0.08	0.05

5.8.2 Ski velocity

The mean and standard deviation of the absolute error in comparison to the light barrier system were calculated to be $-0.78\,\frac{\mathrm{m}}{\mathrm{s}} \pm 1.18\,\frac{\mathrm{m}}{\mathrm{s}}$. This error can be interpreted as $-3.0\,\% \pm 4.7\,\%$ regarding the calculated average take-off velocity of this work ($25.0\,\frac{\mathrm{m}}{\mathrm{s}}$). The comparison of the relative velocity for left and right ski is provided in Fig. 26. The averaged difference during the flight phase was determined to be $0.40\,\frac{\mathrm{m}}{\mathrm{s}} \pm 0.96\,\frac{\mathrm{m}}{\mathrm{s}}$.

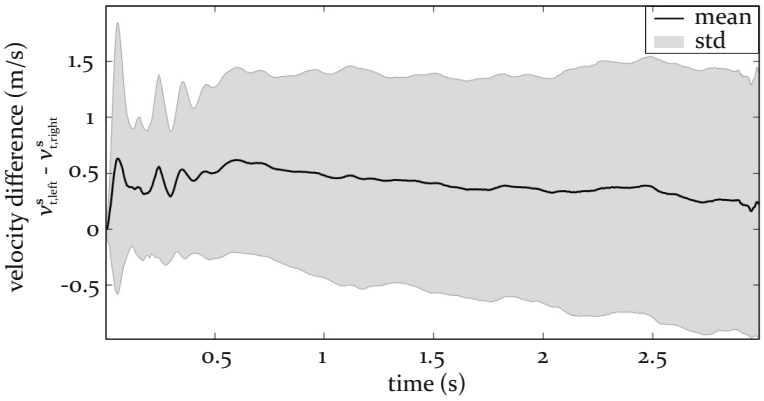

Figure 26: Results of the relative velocity comparison between left and right ski during the flight phase, showing the mean error and the standard deviation. The plot starts with the take-off and ends with the landing instant of the jump with the shortest flight time. © 2017 ACM, printed with permission, modified from [P5].

5.8.3 Jump length

The mean and standard deviation of the jump length calculation error in comparison to the video-based ground truth were established to be 0.8 m ± 2.9 m. This equals a percentage of 0.9 % ± 3.4 % in reference to the average jump length of this work (84.5 m).

5.9 Discussion

5.9.1 Discussion of results

The evaluation of the HHMM-based phase segmentation showed a mean error within the sampling accuracy of the camera hardware (up to 0.01 s) and acceptable results for the standard deviation for take-off (± 0.08 s) and landing (± 0.05 s). With the calculated average take-off velocity of 25.0 $\frac{\text{m}}{\text{s}}$, this equals distance standard deviations of ± 2.00 m and ± 1.25 m. However, the error for the start of the motion was evaluated to be considerable high with a standard deviation of ± 0.83 s. The major impact factor for this behavior was assumed to be the varying techniques for initializing the motion. Some athletes move their skis in the track back and forth before jumping into the track to start the inrun motion, wheres others

remain static until they start accelerating. The algorithm was trained with data of all athletes and hence, with both types of motion behavior. Based on the limited amount of data, it can be assumed that the algorithm could not distinguish whether an athlete actually started the motion or simply moved the skis in the track. With more data sets, the HHMM training could be enhanced for an improved performance.
The velocity evaluation showed an absolute error of $-0.78\,\frac{\mathrm{m}}{\mathrm{s}} \pm 1.18\,\frac{\mathrm{m}}{\mathrm{s}}$ against the light barrier system at take-off and a relative difference of $0.40\,\frac{\mathrm{m}}{\mathrm{s}} \pm 0.96\,\frac{\mathrm{m}}{\mathrm{s}}$ between both skis during the flight phase. With an average velocity of $25.0\,\frac{\mathrm{m}}{\mathrm{s}}$, these results are in a range of under 5 % deviation. Although this error does not allow for the current approach to be incorporated in official judgements at competitions, it can be used for competition support. A direct application would be the visualization of the continuous velocity from start to landing or the comparison of the velocity during various flight phases and in between athletes. A continuous velocity analysis could furthermore be processed for a training support system for athletes and coaches.
The quantitative error of the jump length calculation was evaluated to $0.8\,\mathrm{m} \pm 2.9\,\mathrm{m}$, which equals $0.9\,\% \pm 3.4\,\%$ of the average jump length of this work. The interpretation of this error can be analyzed similarly to the velocity evaluation. The official video-based jump length measurement at competitions provides the jump distance with an accuracy of $\pm 0.5\,\mathrm{m}$ [191]. Hence, the proposed methods do not outperform existing measurement methods considering their accuracy and cannot be incorporated as official judgement tool. Still, competitions and training sessions could be supported by the IMMU-based system. Whereas in this work only the overall jump length was evaluated, the proposed wearable system can monitor the jump continuously and thus, provide not only the jump length but the complete flight path. Analyzing and visualizing the flight path could lead to new training methods and enhance the jump presentation for spectators. In addition, wearable systems are more affordable and if automated, do not require further human interaction. Although the evaluation of the complete flight path was not in the scope of this work, it can be assumed that the proposed methods contain a certain accuracy due to the results of the jump length evaluation with the aforementioned error of only $0.9\,\% \pm 3.4\,\%$.

5.9.2 Impact and application

Consequently, the proposed system could be applied to training sessions as an indicator of the performance and skills of an athlete. Possible ways for training support include the analysis and visualization of jump angles, the athletes jump altitude in reference to the covered distance and the analysis of horizontal and vertical velocities. Based on aforementioned parameters, also the flight style can be established and analyzed by separating flat but fast as well as high but slow jump performances. Furthermore, the velocity development could be monitored during all phases and compared to the overall jump performance.
In competitions, the possible fields of application are similar. Although the camera-based jump length measurement cannot be outperformed by the proposed method, competitions could be supported. Spectators could benefit from innovative ways of jump analysis and visualization, including vertical and horizontal take-off and landing velocities, the ski orientation in various flight phases and finally, the flight path. The athletes' performances could be compared based on their flight style and possibly corresponding success.
For both training and competition support, two major factors are required: an unobtrusive system that does not interfere with the training or competition procedure and an extendable system that can be applied to various jumping hill constructions. In this study, the requirement of unobtrusiveness was fulfilled. Although the sensors have to be charged and calibrated manually, human interaction is not required after the sensor attachment and all processing steps of the algorithms have the potential to run automated. Concerning the requirement of extendability, most parts of the implemented algorithms are based on physical motion models that are not influenced by varying environmental parameters. The only critical part is the HHMM-based phase segmentation. For this study, the model was trained by data of only one jumping hill. A direct application to a different jumping hill can be assumed to lead to inaccurate or even unsuccessful segmentation. However, the model-based approach was chosen on purpose for its ability to be easily trained and to be adaptable to various environments. Consequently, by training the corresponding algorithm with jump data of different hills, it can easily be applied to further jumping hills.
As additional outcome of the proposed system, the ground reaction force of the landing impact could be computed. The continuous velocity can be separated in components parallel and perpendicular to the jumping

hill. Based on the perpendicular component during the landing impact, the landing momentum can be computed. In an initial follow-up study, the algorithms of this work were extended to the described computation of the landing momentum. The resulting momentum was compared to a mobile force plate [192]. The evaluation showed an accuracy of more than 90 % for three out of the four jumps for the landing momentum comparison. By including the weight of the athlete and the landing time duration, the proposed methods could be modified to an IMU-based landing force computation. Although a detailed presentation of the respective study is beyond the kinematic scope of this work, its findings were published and can be found in [193].

5.9.3 Possible improvements

In order to reveal possible improvements of the algorithm, its components have to be analyzed in detail. First, the HHMM-based segmentation was only evaluated for three transitions. Although these are of main interest for this study, a more detailed analysis and possible adaptation of all transitions could improve the overall segmentation accuracy. Second, the orientation calculation was already focus of several publications [49, 50, 95] but in none of them, the 3D-orientation was evaluated against a valid ground truth system. Instead, the orientation was either assumed to be correct as part of the pipeline or was compared to literature values. Third, the flight path could not be validated. Although it can be assumed that due to the plausible jump length calculation, the flight path must contain a certain accuracy, this fact could not be supported by validated facts. In future work, a detailed analysis of aforementioned processing steps could lead to new insight and possible improvements of the overall accuracy.
For a more detailed analysis, also the ground truth measurement process, which contains the light barrier and the multi-camera system, has to be analyzed and possibly improved. The light barrier was aimed on being installed in a standardized way of being triggered by the athletes' shanks, directly above the bindings of the skis (see Fig. 21). However, the installation and the true trigger instant were not validated. Further inaccuracies could be incorporated by the camera system. These include the limited resolution, the camera's perspective and possible uncertainties in the manual labeling process. An improvement, which would also overcome the missing flight path evaluation, lies in a 3D-motion capture system that covers the complete jumping hill area. With markers attached to both skis, all components of this study, including the jump phases, the ski

orientation, the continuous speed and the flight path could be evaluated reliably.
One aspect which should be considered in future studies is the influence of changing temperature on the measurements. In the data acquisitions of this study, the sensors were calibrated at the beginning of each day and it was assumed that the temperature would not change significantly during the training session. However, large diurnal temperature changes might occur. These can be expected to reach ranges of 20 °C (as measured during the Olympic Winter Games 2010 [194]) or more. The conducted climate chamber study of Section 5.2.2 showed the influence of temperature changes on most of the calibration parameters for the sensor hardware of this work. With accurate temperature-depending results for the corresponding measurement hardware of future acquisitions, compensation methods can be applied as suggested in multiple publications [195, 196, 197].

Part III

Performance Interpretation with Kinematic Features

In the third part of this thesis, kinematic features are processed with machine learning methods in order to establish automated performance interpretation. In the application examples of snowboarding in Chapter 6 and skateboarding in Chapter 7, sensor data of board sport trick performances are recorded and processed by automated trick detection and classification algorithms. In skateboarding, the trick performance is additionally visualized in a real-time prototype system. Finally, the community perception on the developed system and on technology in sports in general is analyzed with a survey.

6 Snowboarding: Classification of Slopestyle Tricks

In this chapter, the performance of slopestyle snowboard tricks is analyzed. In standard snowboard training sessions, the performance of athletes is monitored directly by a coach or is video recorded for manual analysis. Employing wearables could simplify the performance analysis and potentially improve the training quality for amateur and professional athletes. An automated wearable system could furthermore be incorporated into the broadcast of snowboard events. The literature covers wearable sensor-based data processing approaches for the analysis of the biomechanics in snowboarding, algorithms for rotation and riding style classification and their application towards feedback systems. However, none of the existing approaches contains an actual trick classification that is applicable to a variety of movements of multiple tricks categories. Furthermore, previously published classification algorithms mostly relied on simple decision-making based on single assumptions instead of considering multiple features and advanced machine learning algorithms. In this thesis, machine learning algorithms are employed for the classification of snowboard tricks of different slopestyle trick categories. IMU data from one sensor per board are obtained and processed. The data are analyzed for trick events and further processed for kinematic feature extraction. Based on calculated orientation features, automatically detected trick events are classified into the corresponding trick category and subsequently into the actual trick class. Multiple classifiers are first used to establish suitable classification models and then evaluated for both the category and the trick classification. The content of this chapter was published in [P6].

6.1 Data acquisition

6.1.1 Hardware setup

The data acquisition was performed with the miPod sensor system ([137], see Section 2.1.4). Accelerometer, gyroscope and magnetometer data were obtained and stored on the device for later processing. Hence, the miPod system will also be referred to as 'inertial-magnetic sensor' or 'IMMU' in this chapter. The IMMU was configured to an accelerometer range

of ± 16 g, a gyroscope range of $\pm 2000 \frac{°}{s}$ and a magnetometer range of $\pm 1200\,\mu$T. The sampling rate was set to 200 Hz. One IMMU was attached to the board of each athlete. The attachment position was chosen to be behind the front binding. Therefore, a protected position could be ensured even when placing the rear foot between the bindings for using a ski lift. The IMMU was attached to the board and additionally secured with duct tape for protection against water and snow. The sensor's attachment and coordinate system were chosen in a way that its x-, y- and z-axes represented the board's longitudinal, lateral and vertical axes (see Fig. 27).
The data acquisition procedure was recorded with two hand-held GoPro HERO2 cameras, which were operated in close proximity to the athletes and focused on the performed tricks. Their resolution was set to 848×480 pixels with a frame rate of 50 fps.

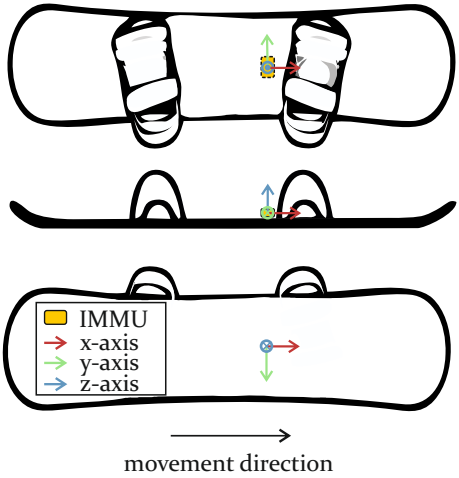

Figure 27: IMMU attachment to a snowboard and the corresponding coordinate system. © 2016 IEEE, printed with permission [P6].

6.1.2 Study design

The data collection was performed in two parts: acquisition A for the differentiation between two trick categories (I: *grind*, II: *air*) and acquisition B for the actual classification of tricks in both categories. An overview of

Table 12: Overview of data acquisitions A and B, including a short description of the performed tricks and the number of repetitions. All stated rotation axes refer to *regular stance direction* and refer to the coordinate system definition of Fig. 27. BS: backside, FS: frontside © 2016 IEEE, printed with permission, modified from [P6].

acquisition	trick	description / rotation	repetitions
A: Hintertux	*grinds* (category I)	riding on obstacle	12
	airs (category II)	jump over a kicker	62
B: Bispingen	*grinds* (category I)		
	- 50-50	straight slide, no rotation	38
	- BS-Boardslide	90° + z, slide, 90° – z	37
	- FS-Boardslide	90° – z, slide, 90° + z	32
	airs (category II)		
	- Method	straight jump, no rotation	37
	- BS-180	180° – z	32
	- FS-360	360° + z	25

both acquisitions with a description of performed tricks and the number of executions is provided in Tab. 12. An example trick of both categories is illustrated in Fig. 28.

grind

air

Figure 28: Example tricks of both trick categories. *Grind*: sliding over objects, such as boxes or rails. *Air*: Jumps over a kicker with optional performance of various rotations and further movements during the *air time*. © 2016 IEEE, printed with permission [P6].

The data collection of acquisition A was performed in Hintertux, Austria. Four experienced athletes (age (years): 18 ± 9, height (cm): 167 ± 13, all male, *stance direction*: two *regular* and two *goofy*) participated in the study. They performed freestyle tricks of both categories: *grinds* and

airs. Due to a large variety of trick performances, there was no further differentiation between single tricks. Instead, the data were used for classification of the trick category. In total, data of 12 *grind* and 62 *air* tricks were recorded with the IMMU and the external camera hardware.
The data collection of acquisition B was performed on an indoor ski slope in Bispingen, Germany. Seven further athletes (age (years): 15 ± 8, size (cm): 156 ± 13, all male, *stance direction*: four *regular* and three *goofy*) performed both *grind* and *air* tricks. These tricks were not only recorded for trick category differentiation but in contrast to acquisition A, also for reasons of actual trick classification. Three different *grind* and three different *air* tricks were executed multiple times. In total, data of 201 tricks were recorded and stored for further processing.
In both acquisitions, a specified calibration procedure was performed. The sensor devices were set in six static positions and rotated about each of the three sensor axes.

6.2 Calibration and standardization of stance direction

The calibration of the accelerometer and gyroscope data was based on the algorithm of Ferraris et al. [40] (see Section 2.1.3). The magnetometer data were only processed for relative changes in the measurements and not for absolute data of single axes. Hence, a magnetometer calibration was not necessary.
In addition, the influence of the *stance direction* on the measured signal was standardized. *Regular* snowboarders lead with the left foot in movement direction, *goofy* snowboarders lead with the right foot. Whereas rotations about the lateral axis (y-axis) do not differ for both stance types, the signals of rotations about the longitudinal and vertical axes show mirrored behavior. In order to combine tricks of both types and to allow for a consistent analysis, all data of *goofy*-riding athletes were modified by inverting the signals of the x- and z-axes.

6.3 Event detection

The main part of the processing chain was initiated by an event detection in order to extract intervals with possible trick events. This event detection was implemented with a threshold-based analysis of the acceleration signal.

6.3.1 Threshold-based analysis

Each trick was finalized by the snowboard landing back on the slope. The corresponding landing impact induced a distinct peak in the acceleration signal, which was used for event detection. For reasons of a consistent analysis that is independent of the exact orientation of the board, the L^1-norm (sum of the absolute values of all axes) of the acceleration signal $s_{a,t}$ was computed for further processing (see Fig. 29).
The landing peaks in $s_{a,t}$ were detected with a moving-window approach in order to minimize the influence of sensor noise. The signal was segmented into windows with the length of 50 samples (0.25 s) and an overlap of 49 samples. The corresponding values of $s_{a,t}$ were summed up for each window and compared to a predefined threshold ϵ. When the summed up values exceeded ϵ, the corresponding window was further processed for containing a possible landing impact. For a robust detection, the parameter ϵ was defined with a LOSO-CV. It was chosen by means of detecting all trick events of the corresponding subjects in the training data set of each LOSO-CV iteration.
The possible trick event itself was defined by the relevant time interval Δt_{rel} before a detected landing impact. Δt_{rel} was defined by manual analysis of trick duration with data of both acquisitions. It was differentiated between $\Delta t_{\text{rel,categ}}$ for the classification of trick category and $\Delta t_{\text{rel,class}}$ for the subsequent classification of the actual trick class.

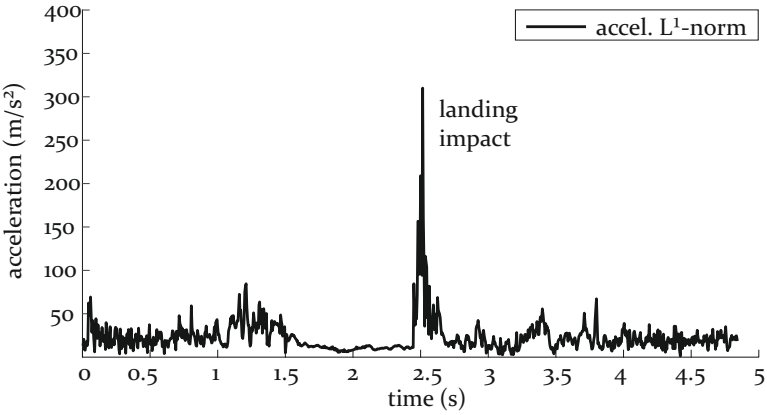

Figure 29: Example signal for the event detection. Trick events were detected with the acceleration signal's L^1-norm $s_{a,t}$ at the landing impact after a trick performance. © 2016 IEEE, printed with permission, modified from [P6].

6.3.2 Evaluation

The evaluation was based on data of both acquisition: 119 *grind* events and 156 *air* events, which results in a total of 275 tricks events. All events were analyzed and labeled in combination with the video recording. All tricks were labeled with a trick category. The tricks of acquisition B were additionally labeled with a trick class. The event detection was evaluated for detecting trick events, without any differentiation of trick category or class. The evaluation was based on a LOSO-CV. Its results were computed to the precision and recall of the algorithm's performance.

6.4 Classification of trick category

The extracted intervals for possible trick events were further analyzed for the corresponding trick category. For this purpose, the analyzed time interval before the landing impact was set to $\Delta t_{\text{rel,categ}} = 1\,\text{s}$, based on previous analysis of the trick duration. The events were classified into three categories: category I (*grind* tricks), category II (*air* tricks), category III (incorrectly detected no-trick events). *Grind* events show high variance in the magnetometer signal due to the proximity to metal rails or boxes (see Fig. 30). In contrast, *air* events contain low variance in the acceleration signal due to only little friction during the *air time* (see Fig. 31).
The classification was performed in a two-step approach. First, the detected events were analyzed for being a *grind* event. Second, all events that were not identified as *grinds* were further processed for being an *air* event or a no-trick event. The procedure is explained in detail in the following sections.

6.4.1 Grind trick classification

In this study, all *grinds* were performed on a metallic rail or box (see Fig. 28), which is often the case in official slopestyle events. These metallic objects can be detected by a high signal variance in the magnetometer measurements. The L^1-norm of the magnetometer signal $s_{\boldsymbol{m},t}$ was computed for each detected event. The corresponding signal variance was calculated with a moving-window approach with a window size of ten samples. From the resulting variance sequence, one feature was extracted per detected event: the number of samples exceeding a specifically defined

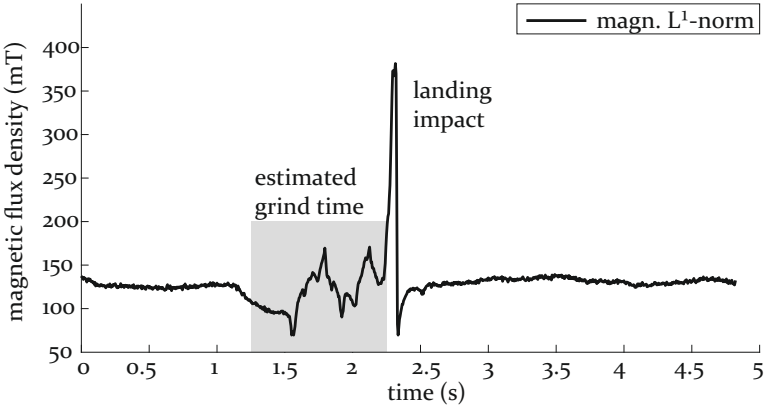

Figure 30: Example signal for the classification of *grinds*. *Grind* events were classified based on a high magnetometer variance during the *grind* time on a metallic surface. © 2016 IEEE, printed with permission, modified from [P6].

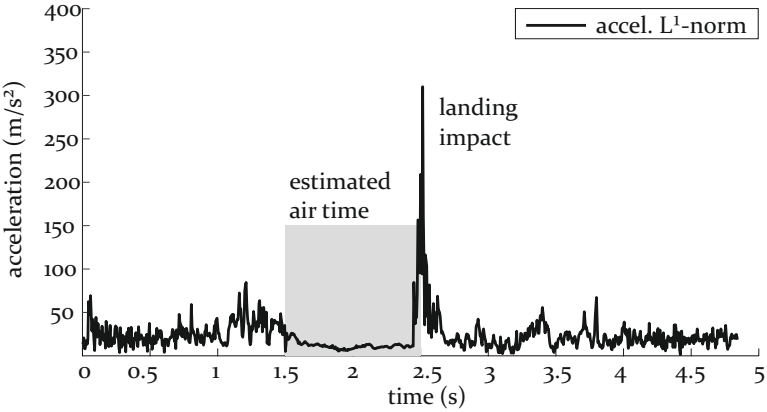

Figure 31: Example signal for the classification of *airs*. *Air* events were classified based on a low acceleration variance during the *air time* of a jump. © 2016 IEEE, printed with permission, modified from [P6].

threshold $\eta_{\text{var,mag}}$. This number was an indicator whether the corresponding event was executed on a metallic surface and hence, possibly represented a *grind* trick.

The classification itself was performed by a NB classifier (see Section 2.3.1). Its goal was to distinguish between the two classes: *grind* events (category I) and all other event (categories II or III). For the purpose of detecting as many *grinds* as possible, the recall of the classification result was weighted higher than the precision. This was implemented by an adapted cost sensitivity matrix [198]. The corresponding proportion of the false negative cost to the false positive cost was set by the weight factor $f_{\text{w,grind}}$.

6.4.2 Air trick classification

After the classification and separation of *grind* events, all other events were divided into *air* events (category II) and incorrectly detected no-trick events (category III). Considering the practical case of performing snowboard tricks, a dead time Δt_{pause} before two subsequent tricks can be assumed. Hence, all detected events that have not been classified as *grind* events but were within the defined dead time interval of a *grind* event, were removed from further processing. In the case of this study, tricks of both acquisitions were analyzed manually and the dead time was defined to be $\Delta t_{\text{pause}} = 2$ s.
The *air* event classification was performed analog to the *grind* event classification. However, the accelerometer signal instead of the magnetometer signal was analyzed. During the *air time*, there is only little noise in the signal and hence, a low signal variance was assumed. With a moving-window approach (same specifications as in the *grind* classification), the variance of $s_{a,t}$ was calculated for all detected events. A threshold $\eta_{\text{var,acc}}$ was defined and the one extracted feature was the number of samples below this threshold. With a NB classifier, the events were classified into *air* and no-trick events. The cost sensitivity matrix was adapted with the weight factor $f_{\text{w,air}}$, respectively.

6.4.3 Parameter definition

For both the *grind* and the *air* classification, four parameters had to be defined: the thresholds for the magnetometer and the accelerometer variance ($\eta_{\text{var,mag}}$, $\eta_{\text{var,acc}}$) and the classification weight factors ($f_{\text{w,grind}}$, $f_{\text{w,air}}$). These were determined by a grid search during the classification. The parameter selection was performed with the criteria of maximizing the F-measure [199].

6.4.4 Evaluation

The evaluation was based on all detected trick events, containing *grind* events, *air* events and no-trick events. For the *grind* category classification and the *air* category classification, the subsequent use of the two NB classifiers in combination with the dead time approach were analyzed. The classifiers' performances were evaluated with a LOSO-CV.

6.5 Classification of trick class

6.5.1 Definition of relevant time interval

All previously detected *grind* and *air* events were further classified into the actual trick class. The relevant signal part was defined to be the interval of $\Delta t_{\mathrm{rel,class}}$ before the detected landing impact. In contrast to the category classification (analyzed signal duration: $\Delta t_{\mathrm{rel,categ}} = 1\,\mathrm{s}$), the trick classification required a longer time interval. For many tricks, the athlete initiates the trick motion before starting the *grind* or *air time*, e.g., by rotating the board. Hence, the time interval for further processing was defined to be $\Delta t_{\mathrm{rel,class}} = 2\,\mathrm{s}$ before the detected landing impact.

6.5.2 Features and classifiers

Although *grinds* and *airs* were classified separately, the classification procedure followed a similar approach. For the selected time interval, a feature extraction was performed. Only snowboard-specific rotation features that were obtained by gyroscope signal integration were extracted. These features were the total rotation during the extracted interval as well as the rotation during the first part and the rotation during the second part of the interval. Each calculation was performed for all three axes, which resulted in a total number of nine features. For feature selection, a best-first wrapper approach (see Section 2.3.1) was applied.
Four classifiers were compared: NB, C4.5, kNN and RB-SVM (see Section 2.3.1). A grid search with varying parameters was included for kNN and RB-SVM. kNN was evaluated for $k \in \{1, 3, 5\}$ and the best parameter setting for the RB-SVM was determined for $C \in \{10^{-6}, 10^{-5}, \ldots, 10^{5}, 10^{6}\}$ and $\gamma \in \{10^{-6}, 10^{-5}, \ldots, 10^{5}, 10^{6}\}$. The feature selection and classification were performed with the embedded classification software toolbox (ECST) [200]

Table 13: Performance comparison of all classifiers for *grind* and *air* trick classification. © 2016 IEEE, printed with permission, modified from [P6].

accuracy (%)	**NB**	**C4.5**	**kNN**	**RB-SVM**
grind classification	87.6	86.7	89.4	**90.3**
air classification	90.4	91.3	**93.3**	89.4

6.5.3 Evaluation

The trick class classification was evaluated with data of acquisition B and hence, was limited to a maximum of 201 actual trick performances. It has to be considered that the input data for the evaluation were directly obtained from the previous processing pipeline in order to evaluate the automated system completely instead of single components individually. As a result, only tricks that were detected by the event detection and subsequently classified into the correct trick category were included in the evaluation. In addition, all incorrectly detected events (false positives in the event detection) and incorrectly classified events in the category classification were included in the evaluation but labeled as no-trick events.
In total, this led to 103 *grinds* with ten no-trick events for the *grind* classification and 92 *airs* with 12 no-trick events for the *air* classification.

6.6 Results

6.6.1 Event detection

In the event detection, 274 of 275 were correctly detected (274 true positives, one false negative) and 471 events were falsely detected (471 false positives). This leads to a precision of 0.368 and a recall of 0.996. The one missed trick event was not considered anymore for the subsequent evaluation steps.

6.6.2 Classification of trick category

From the 745 detected events (274 true positives, 471 false positives), the *grind* category classification correctly categorized 115 out of 119 *grind* events (115 true positives, four false negatives) and incorrectly classified 15 no-trick events as *grind* events (15 false positives). The dead time implementation eliminated 113 no-trick events and no actual trick event.

Table 14: Confusion matrix of the best performing classifier (RB-SVM) for the *grind* trick classification (see trick description in Tab. 12). © 2016 IEEE, printed with permission, modified from [P6].

		true		
predicted	50-50	BS-Boardsl.	FS-Boardsl.	no-trick
50-50	38	3	0	1
BS-Boardsl.	0	33	0	1
FS-Boardsl.	0	0	28	5
no-trick	0	0	1	3

Table 15: Confusion matrix of the best performing classifier (kNN) for the *air* trick classification (see trick description in Tab. 12). © 2016 IEEE, printed with permission, modified from [P6].

		true		
predicted	Method	BS-180	FS-360	no-trick
Method	35	0	0	2
BS-180	1	32	0	2
FS-360	0	0	24	2
no-trick	0	0	0	6

The *air* category classification resulted in 151 true positive and 15 false positive events. Four *air* events were missed in the process (four false negatives). These numbers lead to a *grind* category classification with a precision of 0.885 and a recall of 0.966 and an *air* category classification with a precision of 0.910 and a recall of 0.974.

6.6.3 Classification of trick class

All categorized events (true and false positives) were processed by the trick classification. The classification of all *grind* events showed the best result for the RB-SVM classifier with an accuracy of 90.3 %. The best *air* trick classification performance was achieved by the kNN classifier with an accuracy of 93.3 %. The results of all classifiers and the confusion matrices of the best performing classifier of each class are presented in Tab. 13, Tab. 14 and Tab. 15.

6.7 Discussion

6.7.1 Discussion of results

The evaluation of the event detection showed a high recall of 0.996 but a low precision of 0.386 and hence, a high number of false positives. However, it has to be considered that the threshold parameter ϵ was intentionally chosen in a way to detect all trick events in the training data sets. The high number of false positives was decreased by the subsequent step of the category classification. By implementing the dead time after the *grind* category classification, 24.0 % of the false positives were removed. The NB classifiers for category classification eliminated further false positives and successfully classified the corresponding trick category with a recall of more than 0.95 in both cases. Most of the remaining erroneous detected no-trick events were finally recognized by the trick class classification, which led to the final classification results of 90.3 % for *grind* events and 93.3 % for *air* events. These results exceed the published accuracies of related work in [108] of 88.6 % for turn detection and 88.2 % for action detection.

6.7.2 Impact and application

The proposed algorithm provides a classification of slopestyle snowboard tricks in multiple trick categories. It is capable of distinguishing between the two slopestyle trick categories and three trick classes in each of the categories. Due to its general machine learning-based implementation, it can be extended for further categories (e.g., big air snowboarding) and trick classes. However, for the application of the algorithm to various training scenarios or competitions, more training data have to be collected. Whereas the trick category could already be classified without having further training data, the trick classification is based on extensive training data of the actual trick. Hence, before applying the algorithm to official competitions, training data of corresponding jumps have to be collected. With varying skill level and venue or kicker size, also the parameters have to be adjusted. However, most parameters of this study were chosen based on actual training data and hence, a straightforward adjustment based on additional training data can be assumed.
Another application might be a feedback system for snowboarders. The proposed algorithm could be combined with already existing approaches for weight distribution measurement and visualization [201]. The final system would analyze the pressure (distribution) of both feet and addi-

tionally interpret the measurements of the current trick performance. Hence, trick-specific feedback would be generated, which can be assumed to be more accurate than just analyzing the distribution without any context to the performance. The feedback could enhance the learning progress in snowboard training.

6.7.3 Possible improvements

Regarding the applicability to further venues, the grind category classification has to be adapted. In the current version, it relies on a high variance in the magnetometer signal due to metallic rails or boxes. However, not all obstacles are made of metallic material and hence, another detection method that does not depend on magnetic field variation has to be investigated.
Considering an application at competitions, the system has to be real-time capable. Although the applied machine learning components all have been implemented in real-time algorithms in the literature, the processing pipeline of this work still would have to be adapted for a final real-time application. In addition, data transmission and professional waterproof sensor hardware have to be considered.

7 Skateboarding: Real-Time Trick Classification and Visualization and the Corresponding Community Perception

In this chapter, the performance of skateboard tricks is analyzed. With the recent development of skateboarding becoming an Olympic sport, unobtrusive methods for automated trick classification and corresponding motion visualization can not only be used for daily training sessions of amateur athletes but also support professional competitions. The literature shows the research interest in both the classification and the visualization of skateboard tricks. Regarding the trick classification, several approaches were proposed but none of them included real skateboard data of a large variety of different tricks. The published visualization approaches represent the subjective and creative character of skateboarding but do not cover the actual 3D-trick motion. In this thesis, the processing pipeline contains both an automated trick classification and visualization. IMMU data from one sensor per skateboard are processed for kinematic feature extraction and trick classification. Based on mostly orientation features, detected trick actions are classified for the actual trick class. Multiple classifiers are first used to establish suitable classification models and then evaluated for their accuracy. In addition to the trick classification, the performed motion is visualized by means of a 3D-representation of the board rotation. The classification and visualization algorithms are implemented in a real-time prototype (see Fig. 32), which is then presented to the board sports community. The corresponding community perception on the prototype and the influence of technology in sports are analyzed with a specifically designed survey. The content of this chapter was published in [P7], [P8] and [P9].

Figure 32: Presentation of the developed real-time prototype. Tricks are detected, classified and visualized in real-time. © 2017 Elsevier, printed with permission [P9].

7.1 Data acquisition

This chapter contains multiple study components with different sensor hardware and varying aims. An overview of all components is provided in Table 16.

7.1.1 Hardware setup

The hardware setup contained two different sensor systems. The first system, containing lighter and smaller components, was used for the majority of acquisitions. Its data were processed for the analytical evaluation of the proposed pipeline. The limitation of this system was the missing real-time data transmission. Hence, for the prototype development, a second sensor system with real-time data streaming capability was integrated. Furthermore, several cameras were set up for reasons of general verification and algorithm evaluation.

Table 16: Overview of data acquisition components with the hardware setup and aim of each study part.

name	hardware	aim
trick analysis	miPod IMMU	analytic evaluation of proposed event detection and trick classification
trick visualization	miPod IMMU	analytic evaluation of proposed rotation calculation for trick visualization
real-time prototype	Shimmer IMMU	implementation of proposed algorithms for real-time capable prototype

First sensor system: analytical evaluation

The data acquisition of the analytical part of this chapter, leading to the presented results, was performed with the miPod sensor device ([137], see Section 2.1.4). It was configured to function as IMMU, i.e., including magnetometer sensing. The device was configured to the sensing ranges $\pm$ 16 g (accelerometer), $\pm$ 2000 $\frac{°}{s}$ (gyroscope) and $\pm$ 1200 μT (magnetometer). Its sampling rate was set to 200 Hz. The IMMU was attached to the skateboards of multiple athletes. For a stable and consistent mounting, a sensor-specific attachment frame was designed and manufactured with the requirement of a fast mounting to all commonly used board types (see Fig. 33). Its position on the board was at the right side of the front axis. The coordinate system of the board was defined to align the sensor's x-, y- and z-axes with the board's lateral, longitudinal and vertical axes (see Fig. 34).

Second sensor system: prototype development

For the real-time implementation of the proposed algorithm, a different IMMU device was used: the Shimmer3 ([139], see Section 2.1.4). In contrast to the first sensor system, the Shimmer3 could establish a Bluetooth connection in addition to the internal data storage and hence, allow for a real-time processing of the collected data. The device was configured to the sensing ranges $\pm$ 16 g (accelerometer), $\pm$ 2000 $\frac{°}{s}$ (gyroscope) and $\pm$ 190 μT (magnetometer) with a sampling rate of 102.4 Hz. The coordinate system was defined to match the previously described attachment in Fig. 34.

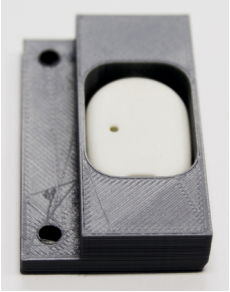

Figure 33: Attachment frame with one miPod IMMU device. The frame was designed for a stable and consistent mounting of the sensor device to all commonly used board types. © 2017 Elsevier, printed with permission, modified from [P9].

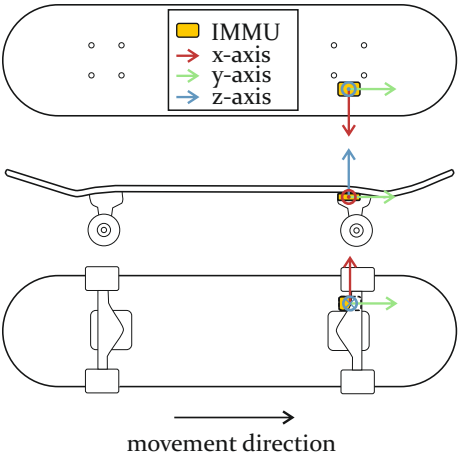

Figure 34: IMMU attachment to a skateboard and the corresponding coordinate system. The attachment frame was positioned at the right side of the front axis. © 2016 IEEE, printed with permission, modified from [P8].

Camera hardware

For trick labeling and general verification of performed actions, all data acquisitions were recorded with a GoPro HERO2 video camera. The resolution was set to 848 × 480 pixels at a frame rate of 50 fps. For later evaluation, a Vicon MX motion capture system with a sampling rate of 200 Hz was integrated in this study. In total, 16 cameras (six MX T10, six

MX T10-S, four MX T20) were used to establish a reference for the 3D-orientation of the skateboard. For the motion capture-based orientation determination, the skateboard was equipped with six reflective markers. The IMMU and the Vicon system were synchronized with a light barrier-based trigger. When a skateboarder passed the light barrier, an indication flag was triggered in both the IMMU and the motion capture data.

7.1.2 Study design

The algorithms of this work were evaluated in a study with two parts: first, the trick analysis with trick event detection and classification and second, the trick visualization. Both contained a sensor calibration procedure and were documented with written notes and a video recording. Before starting the actual trick performances, the athletes were asked to perform three *Ollies* for an initial calibration. The *Ollie* was assumed to be the trick with both the lowest landing impact and the most relevance for all other skateboard tricks. This was used to obtain the individual impact intensity, which was influenced by a combination of the athlete's style, the board's suspension and the ground material.

Study part 1: trick analysis

For the trick analysis, 11 skateboarders (age (years): 23 ± 4, height (cm): 179 ± 5, all male, *stance direction*: six *regular*, five *goofy*) of three German cities (Bayreuth, Erlangen, Leipzig) participated in the data acquisition. Their task was to perform a skateboard training session of about 30 minutes that contained multiple repetitions of 11 predefined tricks. These tricks were chosen in agreement with an external skateboard consultant and combined the most relevant commonly known tricks with and without board rotation. If an athlete could not perform some of the predefined tricks, these could be skipped. The chosen tricks and a short description of their standard execution procedure are given in Table 17. For better understanding of the performed tricks and their specific nature, the gyroscope signals of representative tricks are visualized in Fig. 35.

Study part 2: trick visualization

The second part of the study contained the trick visualization, i.e., displaying the continuous orientation of the board during trick events. This process was assumed to be independent of the variety of athletes and hence, data of only two skateboarders (age (years): 20 and 31, height (cm):

Table 17: Overview of predefined skateboard tricks with a short description of the standard execution procedure and the number of repetitions. The rotation axes refer to *regular stance direction* with the coordinate system definition of Fig. 34. © 2017 Elsevier, printed with permission, modified from [P9].

trick (abbreviation) BS: backside FS: frontside	**description / rotation (angle, axis)** ccw: counter-clockwise cw: clockwise	**repetitions: correct** **incorrect**
Ollie (O)	nose liftoff, nose drop (approx. 45° + x, approx. 45° – x)	79 1
Nollie (N)	tail liftoff, tail drop (approx. 45° – x, approx. 45° + x)	52 1
Kickflip (K)	ccw about longitudinal axis (360° – y)	76 5
Heelflip (H)	cw about longitudinal axis (360° + y)	54 6
Pop Shove-it BS (P-BS)	cw about vertical axis (180° – z)	58 3
Pop Shove-it FS (P-FS)	ccw about vertical axis (180° + z)	64 10
360-Shove-it BS (360-BS)	cw about vertical axis (360° – z)	54 23
Varialflip (VF)	combination of (K) and (P-BS) (360° – y & 180° – z)	61 8
Hardflip (HF)	combination of (K) and (P-FS) (360° – y & 180° + z)	32 17
Double-Kickflip (DK)	ccw about longitudinal axis (720° – y)	35 5
360-Flip (360-F)	combination of (K) and (360-BS) (360° – y & 360° – z)	71 17
Bail	controlled or uncontrolled fall board does not land on wheels	140

both 178, both male, *stance direction*: both *regular*) were obtained. The athletes performed all defined tricks of Table 17 at least twice and it was not distinguished between correct and incorrect performance as both were required to be visualized accurately. Data were obtained with the

attached IMMU and the 16-cameras motion capture system and stored for further processing.

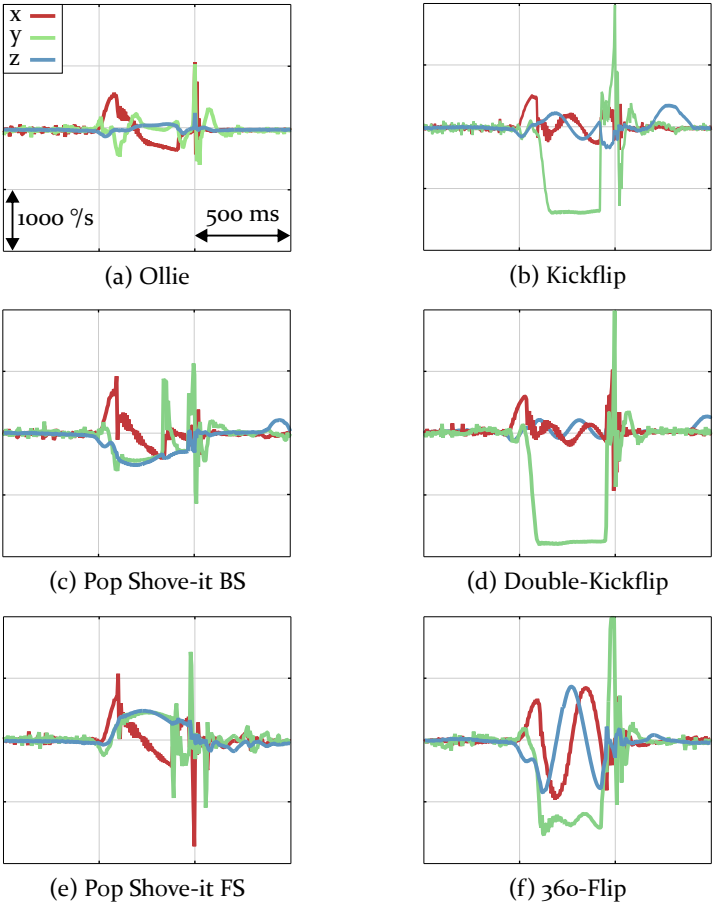

(a) Ollie (b) Kickflip

(c) Pop Shove-it BS (d) Double-Kickflip

(e) Pop Shove-it FS (f) 360-Flip

Figure 35: Gyroscope signals of representative tricks. The distinct signals show the unique rotation sequences of each trick (see trick description in Tab. 17). For tricks (b), (d) and (f), the maximum gyroscope range of $\pm$ 2000 $\frac{°}{s}$ was reached due to a strong landing impact. © 2016 IEEE, printed with permission, modified from [P8].

Calibration procedure

Before starting each acquisition, a specified calibration procedure was performed. The sensor devices were set in six static positions and rotated about each of the three sensor axes for the calibration of accelerometer and gyroscope. For the trick analysis part, no magnetometer data was necessary and hence, no calibration was performed. In contrast, the orientation visualization algorithm required the implementation of the magnetometer. Its calibration was performed by a rotation of the board, including the attached IMMU device, in as many spatial orientations as possible. This process was executed for approximately one minute.
For the first sensor system (miPod IMMU), all calibration data were stored internally for later processing. The second sensor system (Shimmer3 IMMU) was calibrated with a real-time connection to a device-specific calibration tool.

7.2 Calibration and standardization of stance direction

The obtained data of accelerometer and gyroscope were processed with the algorithm of Ferraris et al. [40] (see Section 2.1.3). The magnetometer data were normalized to a amplitude of ± 1, which, despite its simplicity, fulfilled the requirements of the later implementation.
Furthermore, a standardization of *stance direction* was performed in order to allow the algorithm to be applied for both stance types: *regular* and *goofy*. *regular* skaters lead in movement direction with the left foot, *goofy* skaters lead with the right foot. Whereas rotations about the lateral axis (x-axis) do not differ for both stance types, the signals of rotations about the longitudinal and vertical axes show mirrored behavior. Therefore, all signals of the y- and z-axes were inverted for a consistent analysis in the processing chain, without the need of further considering the *stance direction*.

7.3 Trick analysis

7.3.1 Event detection

The acquired data were analyzed in a continuous data stream for all time steps t. Trick events were detected in the data stream based on a strong impact enforced by the landing of the board after a trick performance.

This process contained three steps. First, areas of interest were located based on accelerometer peaks during the landing. Second, the exact landing time was found by gyroscope signal processing of previously located areas of interest. Third, the exact landing time was used to define the whole trick event interval. This process is explained in detail in the following paragraphs and is illustrated in Fig. 36.

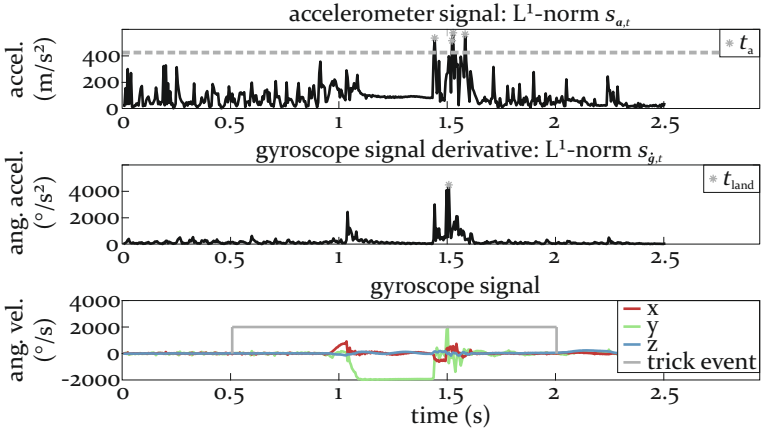

Figure 36: Signal processing for trick event detection. The accelerometer signal's L¹-norm $s_{a,t}$ was processed to indicate possible landing impacts at time t_a and corresponding areas of interest from $[t_a - 1\,s]$ to $[t_a + 1\,s]$ (upper plot). Possible areas of interest were further analyzed with the L¹-norm of the gyroscope signal's derivative $s_{\dot{g},t}$. Its maximum in consecutive or overlapping areas of interest defined the exact landing time t_{land} (middle plot). The trick event interval was defined from $[t_{land} - 1\,s]$ to $[t_{land} + 0.5\,s]$ (lower plot). © 2016 IEEE, printed with permission, modified from [P8].

Accelerometer-based areas of interest

Each landing of the board led to peaks in the acceleration signal $\boldsymbol{a}_t$, with $\boldsymbol{a}_t = [a_{x,t}, a_{y,t}, a_{z,t}]^T$. These peaks were detected by processing $s_{\boldsymbol{a},t}$, which denotes the L¹-norm (sum of the absolute values of all axes) of the acceleration signal. If $s_{\boldsymbol{a},t}$ exceeded a predefined threshold ϵ, the corresponding time t_a was marked in the continuous data stream (see Fig. 36, upper plot). Possible areas of interest were defined to the intervals from $[t_a - 1\,s]$ to $[t_a + 1\,s]$. The range of $\pm 1\,s$ around t_a was chosen based on the determined trick duration with a maximum of less than 1 s.

Gyroscope-based landing impact

Based on the accelerometer analysis, multiple areas of interest were found during each landing but possibly also by hard kicks during the *air time*. A further analysis of all areas of interest with the gyroscope signal $\boldsymbol{g}_t = [g_{x,t},\ g_{y,t},\ g_{z,t}]^T$ was necessary in order to detect the exact landing time t_{land}. The exact landing was defined to be the instant when all wheels touched the ground. This abrupt process caused a local peak in the derivative of the gyroscope signal $\dot{\boldsymbol{g}}_t$, which was analyzed by its L^1-norm $s_{\dot{\boldsymbol{g}},t}$. The landing time t_{land} was found by processing all subsequent or overlapping areas of interest for the maximum of $s_{\dot{\boldsymbol{g}},t}$ (see Fig. 36, middle plot).

Definition of trick event interval

With the determined maximum trick duration of less than 1 s, the beginning of the trick event was defined to be $[t_{\text{land}} - 1\,\text{s}]$. For a detailed analysis of the landing and subsequent actions (e.g., detection of possible failed tricks after the landing impact), the end of the interval was not set to the landing impact but to $[t_{\text{land}} + 0.5\,\text{s}]$. The complete trick event interval, containing the preparation, actual trick and post-trick phase, can be seen in Fig. 36 (lower plot).

Parameter setting

Apart from the predefined time interval settings (area of interest, trick event), which remained constant for all tricks and acquisitions, there is only one adaptable parameter in the trick event detection process: the threshold ϵ. The landing impact-induced peak in the acceleration signal varies with the athlete's specific riding style, the board's suspension and the ground material. Thus, ϵ had to be set individually for all athletes and acquisitions. Therefore, the three *Ollie* performances of the initial calibration phase before each acquisition were analyzed. The maximum of the continuous L^1-normed acceleration signal $s_{\text{a,max}}$ was calculated for all three executions and the lowest one was selected. Then, ϵ was defined to a value of 10 % below this lowest maximum.

7.3.2 Classification

The detected trick event intervals were further processed for classification.

Feature extraction

Most of the relevant information about a skateboard trick performance can be found in the board's rotation and hence, can be obtained with the gyroscope. Therefore, most of the selected features were extracted from the gyroscope signal. These included three correlation-based features (the correlation of the gyroscope's x-y-, x-z- and y-z-axes) and nine time-dependent orientation features (the overall rotation per axis during the trick event, the rotation per axis during the first part and the rotation per axis during the second part of the interval). For the specific differentiation of successful tricks and *bails*, one accelerometer-based orientation feature was added: the x-z-axes correlation after the landing impact. This feature revealed the rough orientation of the board after the landing occurred, i.e., whether the board landed on its wheels (correct performance) or its side or *deck* (*bail*).

Classes and classifiers

In total, 13 classes were defined: the 11 trick classes (see Table 17), one class for *bails* and one rest class for all other events that were marked by the event detection but did not contain a trick performance (e.g., hard drops of the board to the ground in between trick performances). All detected events (also the rest class) were labeled manually. Subsequently, a supervised classification was performed.
The following five classifiers were compared: NB, RF, kNN, LSVM and RB-SVM (see Section 2.3.1). For the kNN and the SVM-based approaches, varying parameters were applied. The best performing parameters were found with a grid search. The kNN approach was evaluated for $k \in \{1, 3, 5\}$, LSVM was optimized for $C \in \{2^{-5}, 2^{-4}, ..., 2^{4}, 2^{5}\}$ and RB-SVM for the parameters $C \in \{2^{-5}, 2^{-4}, ..., 2^{4}, 2^{5}\}$ and $\gamma \in \{2^{-5}, 2^{-4}, ..., 2^{4}, 2^{5}\}$. The Python-based classification environment scikit-learn [202] was used for classification. The library contained a toolbox for data processing and classification. The advantage of this toolbox was that the results could directly be stored and further processed for the later Python-based real-time implementation of the presented prototype.

7.3.3 Evaluation

The evaluation of the trick analysis contained the trick event detection and the trick classification. Both parts were evaluated with the manually analyzed video data and corresponding notes as ground truth reference.

Event detection

For the event detection, detected and missed trick events were categorized as follows: true positives (detected trick events), false positives (detected no-trick events), false negatives (missed trick events). With the corresponding values of all categories, the precision and recall of the proposed algorithm were determined. Failed tricks and *bails* were considered to be trick events as well. The separation of correctly and incorrectly performed tricks was part of the subsequent classification.

Classification

The classification algorithm was evaluated with two different class settings: once with correctly and incorrectly performed tricks (11 trick classes, *bails* and rest) and once with only correctly performed tricks (11 trick classes and rest). This was necessary in order to distinguish between the performance of low-level runs with many failed tricks (e.g., training scenarios) and high-level runs with mainly correctly executed tricks (e.g., application at competitions). The rest class was not affected by this separation and was included in both settings. All five classifiers were applied to both settings and evaluated separately. For the separation between training and validation data, a LOSO-CV was performed.

7.4 Trick visualization

The next step of the proposed pipeline was to visualize the skateboard motion by means of a 3D-representation of the board's rotation. In addition, the outcome of the trick analysis was used to segment the continuous 3D-visualization and to provide the names of performed tricks.

7.4.1 Data fusion for orientation determination

For a short period of time, the board's rotation could be visualized by a simple gyroscope signal integration. However, skateboard sessions usually contain multiple tricks during several minutes or hours. Even a well-calibrated gyroscope would suffer from drift effects when only integrating the angular rate signal. Hence, an advanced visualization was required and a sensor data fusion was performed. The implemented approach was based on the algorithm of Madgwick et al. [41] (see Section 2.2.3) and combined accelerometer, gyroscope and magnetometer data.

In the algorithm of Madgwick, the only adjustable parameter β describes the expected gyroscope measurement error. Increasing β equals a higher expected error and leads to lower influence of the gyroscope on the orientation output. However, for the dynamic application of skateboarding, one parameter setting was not sufficient to cover the full motion range. The skateboard motion can be quite linear and without impacts for some time but it can also contain hard impacts, which possibly lead to gyroscope misreadings (e.g., at hard landing impacts with sensor readings in saturation). Hence, two parameters β were defined in this study: a lower β_{std} for the standard motion and a higher β_{comp} for scenarios, when measurement errors needed to be compensated. Assuming the higher measurement error was only to be expected at and after the landing of the board, β_{comp} was activated for a short-period of time whenever landing impacts were detected. At all other times, the lower β_{std} was used. The duration of the activation time was defined by Δt_{act}.
Following the suggestions of Madgwick et al. in their open-source Matlab implementation [203], the parameter for standard motion β_{std} was set to $\beta_{\text{std}} = 0.1 \frac{\text{rad}}{\text{s}}$ ($5.7 \frac{^\circ}{\text{s}}$). For the compensating parameter setting β_{comp}, the expected measurement error and activation duration were empirically defined to $\beta_{\text{comp}} = 0.9 \frac{\text{rad}}{\text{s}}$ ($51.6 \frac{^\circ}{\text{s}}$) and $\Delta t_{\text{act}} = 1\,\text{s}$. During this compensation duration, the gyroscope had less influence in the orientation computation and the accelerometer and magnetometer signals compensated the expected deviation.

7.4.2 Rotation calculation during trick motion

The resulting output of the Madgwick-based algorithm was provided as quaternion, describing the current change of orientation, i.e., the rotation at time t. In order to obtain the rotation in relation to a specific previous state t_0, subsequent output quaternions from t_0 to t were multiplied (see Section 2.2.1). With this algorithm, two feasible rotation representation methods could be computed: continuously over a long period of time, including multiple tricks, or only for the time of exactly one trick performance, i.e., for exactly one trick interval.

7.4.3 Evaluation

The ground truth for the evaluation was the Vicon motion capture system. The motion capture orientation output was provided by means

of a rotation matrix and therefore, the quaternion-based output of the proposed algorithm was transformed to rotation matrix representation as well. Due to the limited measurement volume of the motion capture system, only the orientation during the trick performances was evaluated. Thus, the evaluation intervals were defined from 1 s before the detected landing impact to the landing impact. In order to achieve continuously comparable orientation estimates of both systems, the initial estimates of both systems were aligned.
For matters of easier comparison and visualization, the output values of both systems were transformed to Euler angles following the same procedure. Rotations about the x-, y- and z-axes of the defined coordinate system in Fig. 34 were denoted by the angles ψ, θ and ϕ. The difference between the motion capture ground truth and the IMMU-based computation was calculated and averaged over all performances with ($\text{angle}_{\text{gt}} - \text{angle}_{\text{IMMU}}$). It was analyzed for all axes over the whole trick interval. Analytically, the difference was evaluated in two ways: 1) the mean and standard deviation per axis and 2) the mean and standard deviation for the combined angular error by the root-mean-square error (RMSE) of all three angles.

7.5 Real-time prototype

The proposed algorithms for trick detection, classification and visualization were implemented in a real-time prototype.

7.5.1 Framework

The implementation was based on the Kivy programming framework of Virbel et al. [204]. It contains a Python-based open source library with a variety of scientific tools including scikit-learn and a GPU-accelerated OpenGL ES 2 graphics pipeline. Due to the Python-based implementation, the proposed trick analysis of Section 7.3 could directly be ported to the real-time prototype. For the proposed 3D-visualization of Section 7.4, the OpenGL graphics pipeline was incorporated.

7.5.2 App implementation

Graphical user interface (GUI)

The real-time application opens with a GUI, which asks the user for the specific *stance direction* and for the required connection to the sensor hardware (see Fig. 37), in the case of this work: the Shimmer3 IMMU. After connecting to the device, inertial-magnetic data are sent to the application.

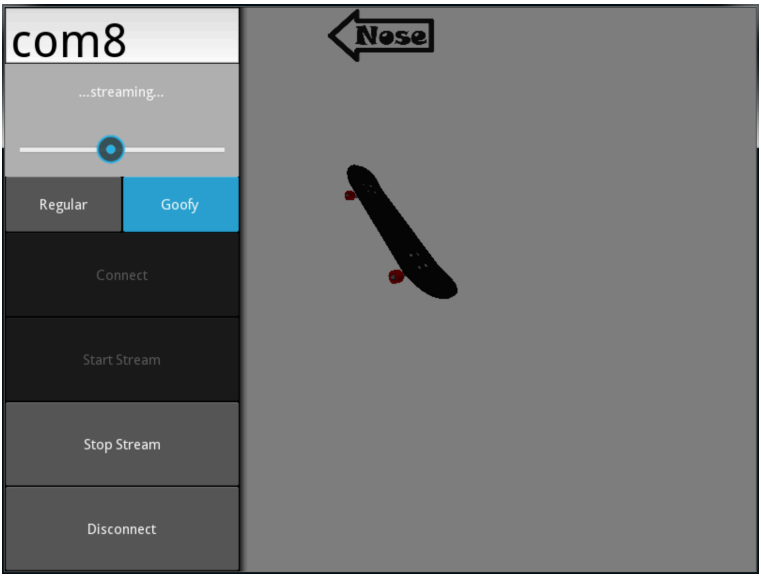

Figure 37: Start screen of the implemented GUI. It requests user input for the selection of *stance direction* and Bluetooth connection settings. © 2017 Elsevier, printed with permission [P9].

Classification pipeline

Initially, the threshold ϵ for the event detection has to be set. This can either be done by a graphical slider or the performance of three *Ollies*, as described in Section 7.3. The incoming data are continuously analyzed for possible trick events. All detected events are processed by the classification pipeline. In contrast to the analytics part of this chapter, there is only one classifier necessary for the real-time application. For this task, the

LSVM was chosen due to its high accuracy at low computational effort. The best performing parameters were obtained from the grid search of the previous analytics evaluation. After each landing impact, the trick classification provides the performed trick, which is visualized in the implemented GUI (see Fig. 38).

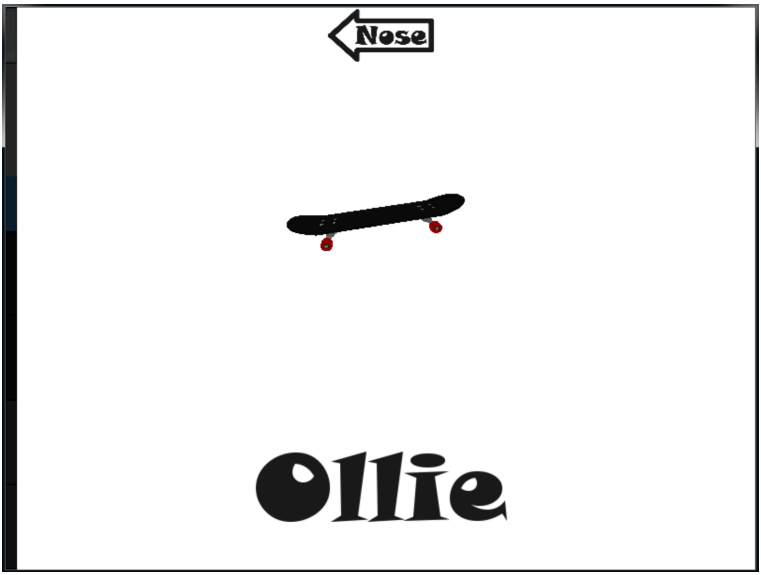

Figure 38: Main screen of the implemented GUI. The skateboard is continuously visualized in its current orientation by means of a 3D-animation. As soon the classification pipeline provides the detected trick, its name is visualized in addition. © 2017 Elsevier, printed with permission [P9].

Orientation visualization

In addition to the name of the trick, the current skateboard orientation is visualized. This visualization is based on an object renderer with a basic 3D-camera, which is provided by the OpenGL camera implementation of the Kivy programming framework. The board orientation is updated in every time step with the quaternion output of the proposed trick visualization algorithm (see Section 7.4).

7.5.3 Video demonstration

A video demonstration of the application is provided in [205]. It contains the performance of five skateboard tricks and one *bail*. The demonstration shows the video recording of the skateboard performance synchronized with the real-time application screen. It furthermore shows the necessity of the adaptive parameter setting for the gyroscope measurement error β. After a hard landing impact, the board orientation shows an offset to the video recorded skateboard and is subsequently corrected during the compensation phase of 1 s after the landing. An example sequence of a *Kickflip* performance is provided by multiple screenshots of the video in Fig. 39.

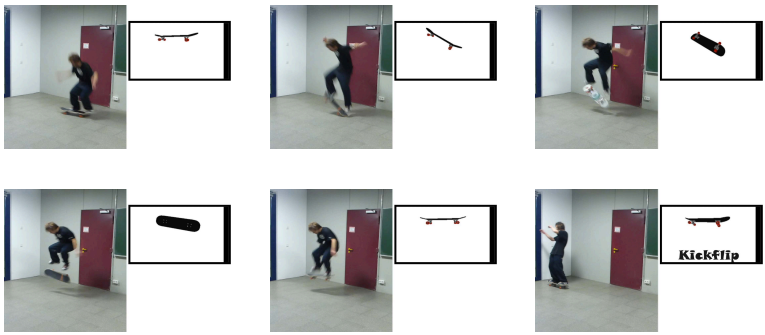

Figure 39: Screenshots of the video demonstration showing a *Kickflip* trick performance and the simultaneous app visualization. The visualization includes the 3D-rotation of the board and in addition, the name of the detected and classified trick. © 2016 IEEE, printed with permission, modified from [P8].

7.6 Community perception

In skateboarding, like many other action sports, the subjective perception of athletes has major impact and is traditionally more valuable than designed measures. The established video demonstration was shown to the skateboard community in order to analyze the community perception. A questionnaire was designed and distributed in the skateboard community. As a result, survey data were obtained from 27 participants

with active skateboarding background (age (years): 23.2 ± 4.4, skateboard experience (years): 10 ± 4.9).

7.6.1 Questionnaire

The topics of the designed questionnaire were divided into three categories: the proposed trick visualization of this study, feedback systems in skateboarding and the general acceptance of technical systems in sports.

Proposed real-time visualization

The first part of the survey covered questions regarding the proposed real-time visualization, which was provided to the participants by the video footage of [205]. The questions contained the issues of

- the likability of the proposed trick visualization,
- the usefulness of such a system and
- suggestions for possible improvements.

Skateboard feedback systems in general

The second survey part covered questions about the acceptance of feedback systems in skateboarding in general, i.e.,

- if athletes would like to know how to further improve their skills based on technical aid,
- if such information is required in real-time or after the training and
- if the feedback should be available with adaptive speed (e.g., in slow motion).

Technical systems in sports

The third survey part addressed the general discussion on technical systems in sports, containing questions regarding

- the fear of prevailing technical influence,
- application fields of technical systems in sports and
- multiplayer game options (e.g., online exchange and competitions of real sports performances).

7.6.2 Evaluation

The questionnaire was designed with a seven-point Likert-type scale [206, 207]. The answers were given in a range from (1): 'strongly disagree' to (7): 'strongly agree'. For the evaluation, the answers of all participants were combined per question. The median was established, as well as the 25th and 75th percentiles, and the maximum range of given answers. In addition, the overall agreement rate per question was established. A question was considered to be agreed with for the participant's selection of (5) or higher and was considered to be disagreed with for the selection of (3) or lower.

7.7 Results

7.7.1 Trick analysis

Event detection

A total number of 905 trick events was counted in the manual analysis. These contained correctly and incorrectly performed tricks as well as *bails*. The evaluated algorithm correctly identified 872 of these 905 events (true positives) and missed 33 events (false negatives). 431 sequences were mistakenly considered to be trick events (false positives). Consequently, the event detection algorithm performed with a precision of 0.669 and a recall of 0.964.
A more detailed analysis showed that the false negatives consisted of the following tricks: *Hardflip* (seven), *Ollie* (five), *Kickflip* (four), *Varialflip* (four), others (13). Furthermore, the false positives were mostly based on sequences during the jump preparation phase.

Classification

Both settings (all tricks and only correctly performed tricks) were evaluated with all five classifiers. The results of both are provided in Table 18. The classification of all tricks showed its best performance with the RF classifier, resulting in an accuracy of 79.8 %. Only correctly performed tricks were best classified with the RB-SVM and an accuracy of 89.1 %. The confusion matrices of both best performing classifiers are provided in Table 19 and Table 20.

Table 18: Performance comparison of all classifiers for all trick events and for only correctly performed tricks. © 2017 Elsevier, printed with permission, modified from [P9].

accuracy (%)	NB	RF	kNN	LSVM	RB-SVM
all trick events	57.1	**79.8**	76.3	70.8	78.1
correctly performed tricks	63.9	87.2	86.3	82.5	**89.1**

7.7.2 Trick visualization

In total, 53 trick events were included in the evaluation. The IMMU-based Euler angle calculation of the algorithm was compared to the motion capture ground truth. The difference is visualized in Fig. 40 for all three

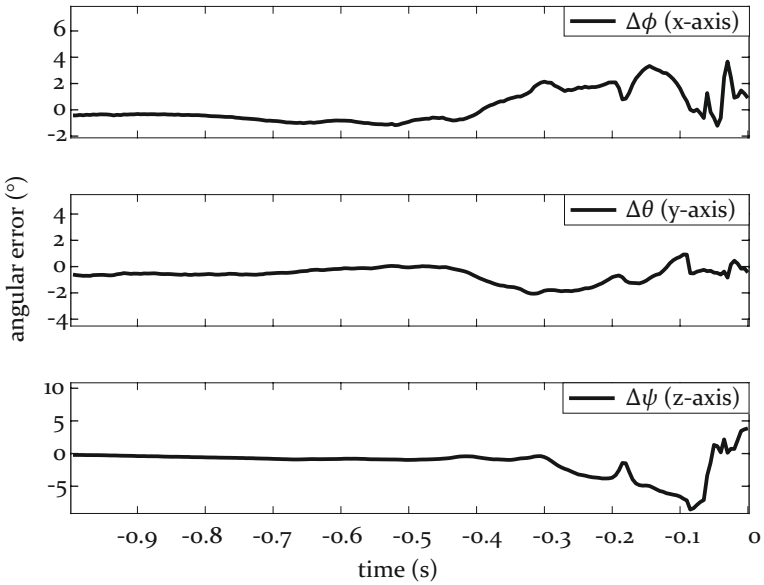

Figure 40: Trick visualization results. The plots show the angular difference between the motion capture system and the IMMU-based computation for all three spatial angles with (angle_{gt} – angle_{IMMU}). The error is averaged over all 53 evaluated tricks. The extracted time interval shows the orientation of the board from 1 s before the detected landing impact to the landing impact itself. © 2017 Elsevier, printed with permission, modified from [P9].

spatial angles ψ (x-axis), θ (y-axis) and ϕ (z-axis) and averaged over all tricks. The time $t = 0$ s was set to the landing impact of the tricks. The averaged error over the analyzed period of 1 s was determined per axis to $0.2° \pm 1.2°$ (x-axis), $-0.6° \pm 0.6°$ (y-axis) and $-1.4° \pm 2.0°$ (z-axis). The overall error that was calculated by the mean and standard deviation of the RMSE of all axes resulted in $2.2° \pm 1.9°$.

7.7.3 Community perception

The results are provided by selected questions and the corresponding answers in Fig. 41. The box plots indicate the median and the 25th and 75th percentiles of the selected answers. The dashed line displays the maximum range of given answers. The overall agreement rate per question is shown at the right side of the box plots. All votes of (5) or higher were considered as agreement, (3) or lower as disagreement.
In addition to the Likert-type scale survey, the following suggestions for improvements were provided by the participants:

- visualization of body and foot movement,
- determination of total rotation angle and *air time*,
- measurement of force applied to the board,
- incorporation of multiple perspectives and
- establishment of training application.

Table 19: Confusion matrix of the best performing classifier (RF) for all trick events (see trick description in Tab. 17). © 2017 Elsevier, printed with permission, modified from [P9].

		true												
predicted	O	N	K	H	P-BS	P-FS	360-BS	VF	HF	DK	360-F	bail	rest
O	69	5	0	0	1	0	0	0	0	0	0	2	7
N	1	46	3	0	0	5	0	0	4	0	0	2	5
K	0	0	62	1	0	0	0	0	4	5	0	8	0
H	0	0	1	48	0	1	0	0	0	0	11	5	2
P-BS	0	0	0	0	48	0	1	0	6	0	0	7	3
P-FS	0	0	0	0	0	62	0	0	0	0	0	5	1
360-BS	0	0	0	0	1	0	60	0	0	0	0	9	0
VF	0	0	1	1	0	0	0	44	0	4	2	9	2
HF	0	0	1	0	0	0	0	0	22	0	0	2	1
DK	0	0	1	0	0	0	0	0	0	15	0	3	0
360-F	0	0	0	2	0	0	0	9	0	0	69	7	0
bail	0	0	8	6	5	1	15	6	7	8	4	72	9
rest	10	2	4	2	6	5	1	10	6	8	2	9	401

Table 20: Confusion matrix of the best performing classifier (RB-SVM) for correctly performed trick events (see trick description in Tab. 17). © 2017 Elsevier, printed with permission, modified from [P9].

		true											
predicted	O	N	K	H	P-BS	P-FS	360-BS	VF	HF	DK	360-F	rest
O	70	5	0	0	0	0	0	0	0	0	0	6
N	1	45	1	0	0	0	0	0	2	0	0	4
K	0	0	67	0	0	0	0	0	0	1	0	1
H	0	0	1	44	0	0	0	10	0	6	10	0
P-BS	0	0	1	0	50	0	1	0	2	0	0	5
P-FS	0	0	0	0	0	57	0	0	0	0	0	2
360-BS	0	0	0	0	0	0	53	0	0	0	0	0
VF	0	0	0	1	0	0	0	49	0	4	0	0
HF	0	0	0	0	0	0	0	0	22	0	0	3
DK	0	0	1	0	0	0	0	0	0	24	0	0
360-F	0	0	0	0	0	0	0	2	0	0	60	0
rest	8	2	5	9	8	7	0	0	6	0	1	410

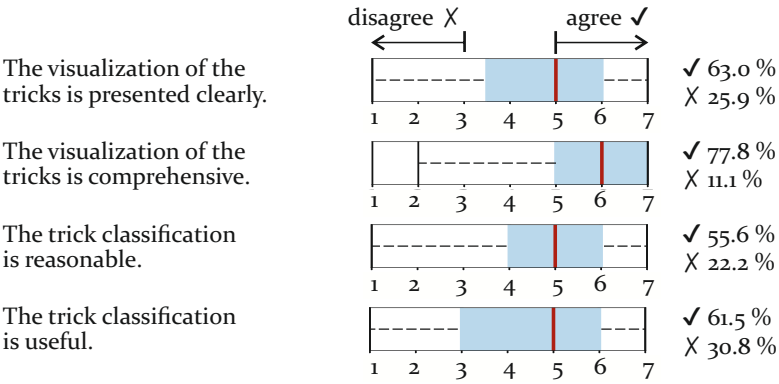

(a) Proposed real-time visualization.

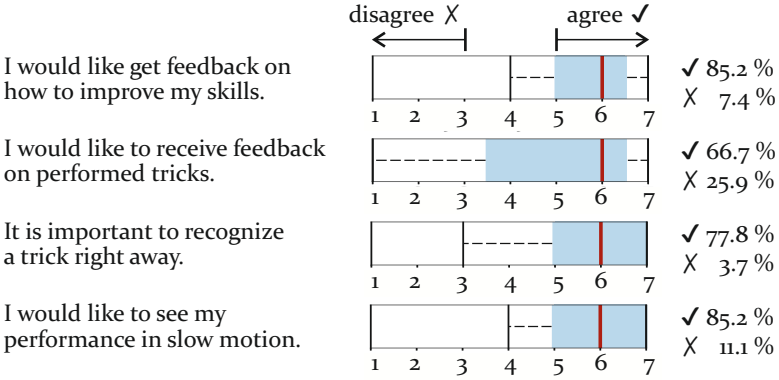

(b) Skateboard feedback systems in general.

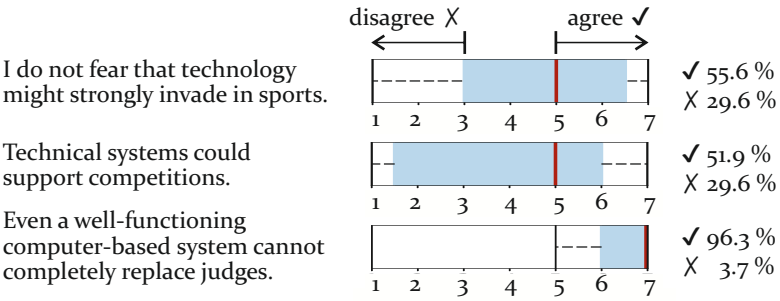

(c) Technical systems in sports.

Figure 41: Survey questions and answers. The box plots indicate the median, the 25th/75th percentiles and the maximum range of provided answers. The overall agreement rate per question is shown at the right side of the box plots. © 2016 IEEE, printed with permission, modified from [P8].

7.8 Discussion

7.8.1 Discussion of results

The event detection's low precision of 66.9 % shows that multiple no-trick events were incorrectly detected by the algorithm. The subsequent event classification could however overcome this limitation by separating tricks and rest class events. The considerable high recall of 96.4 % indicates that the algorithm successfully detected most actual events. The most frequently missed tricks were the *Hardflip*, *Ollie*, *Kickflip* and *Varialflip*. The fact that also the *Ollie* was not always detected shows that the threshold calibration process, which was based on *Ollie* performances, can still be further improved.

The classification algorithm was evaluated to an accuracy of 79.8 %, with RF as best performing classifier for all trick events and 89.1 %, with RB-SVM as best performing classifier for only correctly performed tricks. The lower accuracy for the case of all events indicates that incorrectly performed tricks mislead the classifier's decision. This is also noticeable in the confusion matrix in Table 19. Multiple *bails* were incorrectly classified as various correctly performed tricks. This limitation can be explained by the fact that incorrect performances can be more similar to other tricks than to previously seen *bail* scenarios. A solution for a more robust separation between correctly performed tricks and *bails* could

be a two-step classification. In a first classification step, the trick class would be identified. In a second step, it would be distinguished between successful and unsuccessful performances. Aside from the *bail* class confusion, the results show that most tricks could be classified reliably.
A comparison to related results from the literature shows that the best classifier's accuracy of this work (89.1 %) does not exceed the best accuracies of the publications of Corrêa et al. [119] (98.7 %) and Abdullah et al. [120] (95.0 %). However, it has to be considered that both publications only contained five instead of 11 trick classes. Furthermore, Corrêa et al. only analyzed artificial data and Abdullah et al. classified with data of only one athlete, which simplified the classification task due to the absence of athlete-dependent, individual motion behavior.
The evaluation of the orientation visualization showed promising results with only small deviations from the reference system and an overall error of $2.2^\circ \pm 1.9^\circ$. Regarding the real-time video example, the aforementioned measurement limitations can be seen by the orientation deviation after the landing impact. This behavior is partially influenced by reaching the gyroscope's saturation, as discussed in 7.5.3. In this work, the limitation was overcome by the adaptation of the parameter β after each detected landing impact. Future work could incorporate an advanced algorithm that already compensates the deviation before its occurrence and hence, could improve the visualization quality.
The community perception results in a similar indication. Although the visualization is presented clearly and comprehensive for the majority of participants, it can still be enhanced. Regarding the considerable high acceptance of feedback systems, this enhancement could set the focus on not only visualizing the trick but in addition, on providing direct visual assistance for improving the skill level. Furthermore, it can be seen that the topic of technical systems in sports reveals highly controversial views. Only a slim majority agrees with the statement that technical systems could support sports competitions and the given answers range from 'strongly disagree' to 'strongly agree'. In contrast, 96.3 % of all participants agree that a judge cannot be replaced even by a well-functioning computer-based system.

7.8.2 Impact and application

Due to the sensitive matter of introducing technical support to skateboarding, the application to training scenarios and competitions has to be realized thoroughly. A sudden computer-based interference in compe-

titions would most probably not be accepted by athletes and spectators. In contrast, technical support shows great potential for providing helpful feedback to athletes, which could also be seen as a first step towards introducing technical support in a wider range, including a detailed trick analysis, visualization and establishment of relevant information about a trick performance.
The proposed work provides a solid foundation for these possibilities. The real-time algorithms and established prototype already allow for a stable data processing, trick detection, analysis and visualization. A direct application of the proposed algorithms could be a visual comparison of performed tricks for hobby skateboarders or a visualization aid for competitions. Several measures that were obtained in the algorithm can further improve this visualization experience. Quantitative information, such as the overall rotation, the rotation in specific trick phases or the landing impact were already computed in the processing chain and can directly be provided. Further extensions could also include the *air time* of the board, which could be derived from the obtained jump data.
Although the algorithms are practically already applicable to aforementioned output, further hardware-related modifications would be necessary to establish a costumer product. The prototype used a Bluetooth connection between sensor and mobile processing device. With a range of approximately 15 m, this would be sufficient for applications with the athlete holding on to the mobile device, but not for cases with a central computing device collecting data of multiple athletes (e.g., training scenarios with one coach and multiple athletes). Furthermore, a customer product should be designed and produced with cheaper components than the established prototype. The incorporated sensor hardware of this study was selected for research purposes with the option of setting higher sampling rates and sensor ranges. With exception of the gyroscope, which needs to sense in a wide range, all other components could be assumed to be sufficient with a lower sampling rate, range and accuracy.

7.8.3 Possible improvements

Besides the necessary hardware-related modifications for a first application, there are further possible extensions and improvements. The algorithm of this study was designed for analyzing the data of one sensor attached to the skateboard. However, there are multiple commonly performed skateboard tricks that include not only a rotation of the board but a simultaneously rotation of the athlete's body (e.g., 180-Ollie: the

athlete performs an *Ollie* and additionally rotates the board and his own body about 180°). Hence, a second sensor attached to the athlete's body would be required to fully recognize the trick performance.
Another extension would be given by incorporating pressure sensing, as suggested by Park et al. [118], who proposed a 2D-visualization of the pressure distribution on the skateboard. A textile pressure sensing matrix could be integrated in the board below the grip tape and obtain the athlete's position on the *deck* in combination with the applied pressure. As combination with the proposed algorithms of this work, the pressure distribution could be visualized on a rotating skateboard in a 3D-visualization. A prototype of such a visualization was established in a student thesis [208] in the context of this work. Its results pointed out the feasibility and the potential of such a pressure and rotation visualization.

Part IV

Overall Discussion and Conclusion

The last part of this thesis contains an overall discussion and conclusion. In Chapter 8, the proposed methods, with special focus on orientation features, and the crucial topic of acceptance of technology in sports are discussed. Furthermore, the established and partially already implemented outcome of this thesis and possible future work is elaborated. In Chapter 9, the content of this thesis is summarized and a conclusion with regard to the application in sports analytics is given.

8 Discussion

The content of this thesis is discussed in this chapter. This includes a discussion of the applied methods with the special focus on orientation features, the topic of acceptance of technology in sports analytics with opportunities for application of the proposed methods and finally, an outlook regarding future work.

8.1 Methods of this thesis

In this section, the reasoning behind crucial methodological decisions is elaborated and possible alternatives are considered.

8.1.1 Data acquisition

Measurement methods

The measurement methods of this thesis were designed for data processing of IMUs and IMMUs. Although the advantages of these devices were demonstrated throughout several application fields, the replacement or extension by other measurement devices has to be discussed.
Within the requirements of unobtrusiveness, camera-based measurement methods provide an often used alternative to IMUs and IMMUs. In general, their advantages lie in the unobtrusiveness and the simplified interpretation. Camera-based methods either rely on video data processing or on markers attached to the object of interest [179]. For both, the required unobtrusiveness is fulfilled for most applications. Furthermore, the collected data can easily be interpreted by watching the recorded video, which is also often available for marker-based systems. The disadvantages of camera-based measurement methods are the limited observation area and the more complex setup in comparison to wearable IMMU hardware [60].
In the field of sports, Shih [209] published a survey on content-aware video analysis. The author showed the wide field of camera-based sports analytics and pointed out future trends. Amongst others trends, the topic of visual feature extraction for automated event detection and machine-based motion interpretation is discussed. Sarafianos et al. [210] provided a literature review on camera-based human pose estimation. In addition, they summarized related challenges, such as the variability of possible

shapes, the analysis of crowded scenes and changes in the outdoor environment that influence the video background.
For this thesis, the advantages of IMMUs outweighed those of camera based systems regarding the requirements of covering wide acquisition areas in most cases [35]. Whereas the IMMU-based solution could directly be applied to the investigated applications, an easy camera-based solution would not have been feasible. All sports either covered a wider distance than can be recorded with a simple camera-based system or, in the case of scuba diving, even took place under water. As a result, camera-based methods provide a valid alternative if the challenge of covering the relevant measurement area can be solved. For larger areas, this challenge leads to either a time-consuming and potentially costly measurement setup, as described in [180], or to limitations regarding the data quality. Hence, wearable IMU and IMMU devices might be preferred for large and hardly accessible acquisition areas.
Alternatively, a data fusion approach of IMMU- and camera-based methods could be considered [211]. Large areas could be covered by the wearable devices and for specific locations, camera-based measurement could improve the accuracy or even support the overall stability of the IMMU data by recalibration in camera-covered areas.

Calibration

Due to the small size of MEMS IMU devices, their accuracy is limited. Thus, sensor calibration has to be performed regularly (see Section 2.1.3). In the case of this work, a sophisticated and stable calibration procedure was applied to most of the collected data. For the winter sports applications of ski jumping (Chapter 5) and snowboarding (Chapter 6), the calibration was specifically executed with acclimatized sensor hardware in the outdoor measurement environment before starting the data acquisition. Still, the procedure could be improved by continuously adapting to the measurement environment with its corresponding temperature and the related change of calibration parameters over time.
The influence of both the temperature and the time was evaluated in Section 5.2.2. As a result, the necessity of calibrating in the measurement environment and temporal proximity to the acquisition was shown. However, these requirements could not be completely fulfilled for all applications of this work. For instance, in the presented scuba diving study (Chapter 3), the calibration was performed right before the acquisition but outside the pool and hence, not in the actual measurement

environment. It can be assumed that the water temperature varied from the air temperature and so did the calibration parameters in both environments. For long-term measurement, not only the changing temperature but also the changing calibration parameters over time have to be considered, e.g., for the application to ski jumping competitions that can last multiple hours. A solid solution and possible improvement to this thesis would be given by regular calibration executions (with a minimum requirement of regular ZVUs) in combination with automatically adapted calibration parameters in reference to the environmental temperature.

8.1.2 Kinematic analysis

Limitations of kinematics with regard to sports biomechanics

In this thesis, kinematic analysis methods are proposed. However, not all fields of sports analytics, especially in the field of sports biomechanics, can be covered with kinematic analysis. Whereas kinematics considers all aspects of motion, it does not include the forces causing the motion [37]. All force-related investigations of sports analytics are covered by the field of kinetics.
Therefore, further measurement and analysis methods would have to be considered, especially for research topics that focus on ground reaction forces [212]. Although these forces are traditionally determined with floor-mounted force plates, the progress in hardware miniaturization led to the development of portable force plates [192, 213] and shoe-integrated pressure sensors [214, 215]. Hence, one option to combine kinetic analysis with the methods of this work is given by the fusion of IMUs or IMMUs with additional force or pressure sensing hardware, as suggested in [214]. Another option is given by processing inertial sensor data for an estimation of applied forces, which often includes inverse dynamics calculations [31]. An initial approach for inverse dynamics calculations in ski jumping was presented as follow-up study of this thesis in [193] (see Section 5.9.2).
The outcome of kinetic sports analytics primarily has an impact on the determination of the forces and force-related measures. An application that benefits from force-related measurements is the landing analysis, which is of major interest for various sports [216]. Analyzing the landing procedure can either directly be used for training enhancements or be implemented for injury prevention. Although injury prevention can also be achieved with kinematic measures (e.g., by classifying and counting

specific sports actions in order to monitor an athlete's load), often occurring injuries can be avoided by sports science research with the focus on applied forces, e.g., during landing tasks [217].

8.1.3 Performance interpretation

Classification model

Regarding the topic of performance interpretation with machine learning, this thesis was focused on conventional classification methods, which were described in Section 2.3.1. These conventional methods follow the introduced pipeline by processing generic and expert (i.e., domain-specific) features with defined classifiers. However, in the state-of-the-art literature, there are further machine learning methods that were not applied in this thesis. One common and rapidly developing method is deep learning [218]. Input data are directly fed to the deep learning algorithm and hierarchically processed in multiple layers of representation, which allows for representation learning of the raw data. Features do not have to be defined beforehand but are learned automatically from the raw data input.
Deep learning approaches often outperform conventional classification methods. A direct comparison of their performances with regard to sports analytics was provided by Kautz et al. [15], who classified beach volleyball actions. Whereas the best performing conventional classifier (RF) only achieved an accuracy of 67.1 %, the implemented deep learning algorithm reached an accuracy of 83.2 %.
However, it also has to be considered that deep learning performs best with a high quantity of training samples and thus, is preferably used for cases with easy access for data acquisition. The results of Kautz et al. were based on more than 4000 samples for ten classes. Due to the (extreme) sports-specific nature of the classification topics of this thesis, a significant smaller number of training data was available for the classification in snowboarding (275 samples in six classes) and in skateboarding (905 samples in 12 classes). As a result, deep learning is not practicable in these cases but could possibly be applied in a later state with more training data.

Learning paradigms

In addition to the classification model, also the learning paradigm has to be discussed. The three mainly used paradigms are supervised, unsu-

pervised and reinforcement learning [219]. For supervised learning, the task of the classifier is to connect labeled input data to expected output data (classes). In contrast, unsupervised learning is applied with unlabeled data. The machine learning task is to find patterns in the unlabeled data without knowing the expected output. Reinforcement learning is applied in a similar way. However, the performance of the corresponding machine learning model is improved iteratively by including feedback on the consequences of the output.
In the field of machine learning in sports, mainly supervised and unsupervised learning are of interest [43]. Supervised learning is applied to known scenarios that allow for (manual) data annotation, whereas unsupervised learning can be applied to scenarios of data with (partially) unknown content. A combination of both is semi-supervised learning, which is applied for scenarios with only partially labeled data that could not be used with a solely supervised approach. Unsupervised and semi-supervised learning both have their advantage by less effort in the classifier training, in combination with a potential decrease of errors due to human influence in the annotation process. In combination with deep learning, new context can be explored by recognizing previously unknown patterns.
In the scope of this work, only supervised methods with manual labeling were considered. Based on the limited number of samples and the specific classification problems that the presented topics were based on, the application of semi-supervised or unsupervised learning did not provide constructive solutions. However, further evaluation of the analyzed motion could be built on the already established and evaluated models. These models would then be continuously enhanced with new training data but without the necessity of further annotation.

8.2 Application of orientation features

The presented algorithms all contained either the establishment or the processing of orientation features. As a part of the contributions of this thesis, the potential of orientation features was shown for both the kinematic analysis and the performance interpretation in sports.

8.2.1 Kinematic analysis

For the kinematic analysis, the current orientation or rotation of the body or sports-related object has major impact, as shown in Part II of this thesis. In scuba diving, both the upper body and the shank orientation

were obtained and could be further used for sports-science analysis. In rowing, the related literature stated the importance but also the lack of wearable measurement methods for a rotation analysis during rowing strokes. This thesis provides the required methods with the establishment of IMMU-based rotation calculation. In ski jumping, orientation and rotation calculations were included in the phase segmentation, the functional alignment, the ski velocity estimation and the jump length determination. Beyond that, the relevance of an accurate orientation estimate at all times was indicated by further processing of obtained kinematic features for kinetic analysis by the example of a landing momentum estimation.

8.2.2 Performance interpretation

For the performance interpretation of Part III of this thesis, the presented classification models were trained and evaluated with multiple features. Most of these features were related to the orientation of the analyzed objects. In the case of the trick classification in snowboarding, exclusively nine orientation features were processed by the machine learning pipeline (see Section 6.5.2). The corresponding algorithm in skateboarding was designed for classification with ten orientation features and three correlation-based features (see Section 7.3.2). With classification accuracies of about 90 % in both sports, the potential of orientation features was demonstrated.

8.3 Acceptance of technology in sports analytics

This thesis showed that kinematic features can be accurately established and further processed for sports-specific movement classification with high accuracies. Thus, from a technical point of view, the incorporation of (new) technology in sports can be seen as overall improvement for sports analytics. However, despite all positive enhancements of this and related research, the subjective character of certain sports must not be ignored. Many sports, and extreme sports in particular, contain subjective components that are of major importance for athletes and spectators. These components can be the coolness or risk propensity of an extreme sports performance (e.g., in big air snowboarding) or the overall perception of the spectator while watching an athlete's performance (e.g., the athlete's facial expression during performance).

On the one hand, state-of-the-art technology might already be able to assess these components, e.g., with an analysis of previous perception input or with facial recognition tools. In the example of ski jumping, a combination of the velocity and jump length determination of this thesis, with the research of Brock et al. [101, 220] on a machine learning-based motion evaluation system, could possibly already replace a human judge with an automated scoring system. However, on the other hand, it has to be considered that the society's trust in machine intelligence can (still) not compete with the trust in humans. The survey results of Section 7.6 clearly show that although most of the participants believe that technology can support competitions, one third of the interviewed persons fear a strong invasion of technology. Finally, almost all of them state that a human judge can never be completely replaced. Whether this statement can prevail in future or eventually gets revised, it is of great importance to proceed carefully by exploiting the full potential of current and upcoming technology. Batuev and Robinson [221] provided critical insight in the evolution of modern sports by the example of skateboarding becoming an Olympic sport in 2020 [222]. They discuss the controversy of the originally rebellious character of skateboarding and the recent decision to include the sport in major events such as the Olympics.
A related issue is given by the attachment of sensors to athletes or their equipment. For an overall analysis with wearable sensors, the athletes have to agree on continuously wearing the provided sensors, even in critical phases of a competition. The psychological stress that comes with additional items on the body, especially devices that measure and possibly broadcast ones every move, must be considered for a smooth introduction of wearables to sports. Hence, further work is necessary to bring technology closer to athletes but also to integrate technology in even more unobtrusive ways for the daily use in amateur training and the professional application in competitions.

8.4 Application of the proposed research

By the time of finishing this thesis, several of the proposed methods have been prepared and partially implemented for television broadcast.
During the Olympic Winter Games 2018 in Pyeongchang, South Korea, parts of the proposed algorithms for kinematic feature establishment were applied. For selected jumps of nordic combined and ski jumping, inertial data of the athletes' skis were obtained and processed for the calculation of the ski orientation. Specific ski angles were presented to

the spectators on the public score board at the jumping hill venue. Furthermore, the continuous velocity calculation was used for the television broadcast. Traditionally, only the take-off velocity is measured with light barriers and presented to spectators in the television broadcast. For the Olympics, this broadcast was extended by presenting the ski velocity in two additional instances: at the position of 20 m from the take-off platform and for the landing (see Fig. 42). Both the ski orientation and the velocity calculation were based on wearable sensors and the algorithms of this thesis. After the Olympics, the described innovation in television broadcast was repeatedly incorporated into further competitions, e.g., at the Four Hills Tournament (German: 'Vierschanzentournee') 2018/19, which combines four ski jumping World Cup events. A news article regarding the incorporated technology can be found in [223]. Furthermore, extended analyses based on the proposed methods, containing the continuous ski orientation, velocity and height over ground, were provided to participating athletes and coaches.

Figure 42: Screenshot of the application of kinematic feature establishment for the television broadcast of the Olympic Winter Games 2018 in Pyeongchang. Based on the algorithms of this thesis, the traditional velocity information at take-off was extended by the velocity at 20 m from the take-off platform and the landing velocity. © 2018 IOC, printed with permission [224].

In a similar field, innovations in the analysis methods for snowboarding are currently prepared for application in television broadcast. The state of ongoing development of the research of this thesis was topic of articles in

the IEEE Spectrum magazine [225] and the Royal Spanish Winter Sports Federation news [226]. The IEEE Spectrum article mainly focused on the presented study of Chapter 6 and illustrated the general research on wearables in snowboarding. The Royal Spanish Winter Sports Federation reported on a data acquisition during a snowboard competition in the ongoing investigation of this work. It can be speculated that current ways of motion visualization for television broadcast will be further extended by including wearable sensors.
Despite the controversial attitude of skateboarders and board sports enthusiasts, the International Olympic Committee decided to include skateboarding in the Olympic Games [222]. Due to the rather young history of technology in sports and visualization of skateboard performance for television broadcast, the research of this thesis would potentially provide the groundwork for an application to the Olympics. At the point of finishing this thesis, the decision whether or not skateboarding will be accompanied by wearable sensors in 2020 has not been finally published. In case of a decision for wearable sensors, the provided research can be applied to support the analysis, interpretation and broadcast of skateboard events.

8.5 Outlook

Open research questions that could not be addressed within the scope of this thesis can be separated in the following areas: the extension of the methods of this thesis, their transfer to sports science and their implementation for the use case in real-world applications.

8.5.1 Extensions of proposed methods

The proposed methods can be extended and possibly improved with regard to the following topics. The data acquisitions of this work can be improved by several modifications. One modification is to increase the number of participating subjects. In particular, for the proposed machine learning approaches, more training data potentially lead to higher classification accuracies and more robust algorithms. Another data-related modification is the improvement of the calibration procedure. In this thesis, it was shown that uncompensated temperature changes have major influence on the calibration parameters and hence, on the data quality. In particular for the establishment of kinematic features by single or double integration of IMU data, an improved calibration would potentially

lead to better results. Furthermore, for an optimized study design, the ground truth data quality for later evaluation can be enhanced. Whereas the requirements for the evaluation of the supervised machine learning tasks were met with corresponding manual data labels, the evaluation of the kinematic analysis could be improved by more sophisticated ground truth data. In particular, the applications to scuba diving (Chapter 3) and rowing (Chapter 4) would benefit from a highly accurate 3D-motion capture system. This would not only lead to more accurate evaluation results but at the same time also amplify the impact of the results.
The proposed algorithms for kinematic analysis could be extended by specifically designed filter approaches. In the application for ski jumping (Chapter 5), it was shown that the processing of inertial data in ideal environment (in this case: during the *air time* without any friction-related noise) can lead to very accurate results, even after double integration of the raw data. Considering the influence of friction-related noise for other cases, the data quality and hence, the overall results could be enhanced by advanced filtering to cancel out friction-related noise. For the machine learning tasks of this work, the incorporation of deep learning algorithms potentially further improves the classification accuracies. However, it has to be considered that a strongly increased number of training data would be required. In addition, the learning paradigms could be modified. Based on already labeled training data and corresponding classification models, future data acquisitions could be included in the classification process with semi-supervised learning. In case of the application of deep learning, also unsupervised learning methods could be considered.
Finally, the proposed algorithms could be extended to other sports. Kinematic features, possibly with the focus on orientation features, can provide relevant output for related sports, such as high diving, figure skating and gymnastics. Performance interpretation can be achieved by applying machine learning algorithms to further boards sports, such as big air snowboarding, halfpipe snow- and skateboarding, surfing and windsurfing.
In summary, possible future work based on the methods of this thesis contains improvements in the acquisition of measurement and ground truth data, the implementation of further filter methods, the extension of the methods with kinematic analysis and deep learning algorithms and the transfer of the proposed methods to further sports.

8.5.2 Transfer to sports science

The content of this thesis describes the technical potential of IMU- and IMMU-based data processing. Transferring the proposed methods to sports science can lead to new analysis methods and more insight in specific sports, which in turn may be used to develop improved training procedures.
With the chapters on kinematic analysis, this thesis provides methods for extracting kinematic features, which can be provided to athletes, coaches and spectators. By incorporating these features to sports science, existing training methods could be investigated with advanced input and possibly be enhanced by new kinematic insight. Also, a high number of measurements can be obtained based on the automated and unobtrusive methods of this thesis. Another impact on sports science could be achieved by the processing of kinematic features for kinetic analysis, e.g., for the analysis of landing procedures after athletic jumps. The analysis of landing tasks is of major interest for sports science investigation in training enhancement and injury avoidance. As briefly described in Section 5.9.2, the outcome of this thesis has the potential to simplify landing analysis by incorporating unobtrusive, wearable sensor hardware.
Besides the technological aspects, sports science-related research should also cover the social component of the topic of sports analytics. Even if analysis methods are well established, work robust and show great results from a technical and sports science perspective, the sports community might still disapprove of technical support and influence in sports. For most technological innovations and especially for extreme sports, a smooth introduction with well elaborated concepts is necessary. One future task of sports science could be the establishment of such concepts.
In summary, future work based on transferring the proposed algorithms to sports science contains the analysis of extracted features from a sports science perspective, the collection of a high number of measurement data, the investigation in landing analysis and the smooth introduction of established technology to the sports community.

8.5.3 Implementation for real-world applications

The subsequent implementation of the established methods can cover real-world applications for training scenarios and competitions. A major part of the proposed kinematic analyses could directly be implemented for the use case. Only environmental parameters, such as the jumping hill

specifications in ski jumping, would have to be adapted. The machine learning applications for performance interpretation are designed generically and only require new training data for the specific application. However, further issues have to be resolved before a frequent use in real-world scenarios. One of these issues is the real-time capability, which would be required for some applications. In this thesis, the prototype for skateboard trick analysis and visualization (see Section 7.5) was the only real-time implementation. Although all other algorithms were designed for a potential implementation in a real-time system, further work is necessary for the development of a system that can run reliably in a real training or competition environment. Another issue is the presentation of the generated output. Whereas the presentation of this thesis aimed at stating the scientific results, a presentation at competitions would require much more sophisticated visualization methods that draw the spectators' attention and present results in comprehensible ways.
Besides the implemented algorithms, the incorporated hardware components and their attachment to athletes and sports equipment have to be discussed. The hardware used for the analytics of this work was designed for scientific purposes. It contained state-of-the-art technology for accurate measurements and a variety of sensing possibilities, such as pressure and temperature sensing (see Section 2.1.4). As a result, in certain application scenarios, this state-of-the-art hardware would exceed the requirements for daily use, i.e., cheaper hardware with possibly less sensing components could be incorporated instead. In contrast, the sports-related sensor attachment in this thesis was often accomplished in a very simplified and pragmatic way that satisfied the purpose of the study. One example of such a simplified attachment is shown for scuba diving in Fig. 11. For an application of daily use, more unobtrusive and integrated attachment methods are required. Therefore, future work for the implementation for real-world applications would contain the revision of incorporated hardware and its attachment.
In summary, future work for training and competition support contains the adaptation to the corresponding environment, the acquisition of new training data for machine learning tasks, the establishment of advanced visualization methods and the revision and further development of the incorporated hardware and corresponding sensor attachment.

9 Conclusion

The aim of this thesis was to present methods for sports analytics using unobtrusive IMU and IMMU devices. The presented methods were divided into the extraction of sports-specific kinematic features and the subsequent interpretation of these features with machine learning algorithms. In addition, the potential of orientation features as major component for kinematic analysis and performance interpretation was elaborated. The presented methods covered topics of state-of-the-art sports analytics in five sports: scuba diving, rowing, ski jumping, snowboarding, skateboarding. The following sports-related contributions were achieved in this thesis.

Kinematic feature extraction with focus on orientation features was applied to scuba diving, rowing and ski jumping. In scuba diving, algorithms were presented for an automated fin kick detection and orientation determination for the upper body and shanks. The proposed methods could be applied to sports science for optimizing the fin swimming and scuba diving motion. In rowing, the motion pattern was analyzed for both amateur and professional athletes. Consecutive rowing strokes were automatically separated and the corresponding in-stroke boat rotation was calculated. The presented algorithms could directly be applied for training support and competition broadcast or transferred to sports science for further research on the rowing boat motion behavior. In ski jumping, HHMM-based jump phase segmentation was introduced. Based on the jump phases, the ski orientation was computed and further processed for the determination of the continuous ski velocity and jump length. Furthermore, the extracted kinematic features were used to estimate the landing impact. The proposed kinematic feature extraction was already incorporated for the broadcast of professional competitions and can further be extended in future work. The proposed follow-up work on landing impact analysis based on the established kinematic features could be the first step towards unobtrusive landing analysis without any external measurement equipment.

Further processing of orientation features for machine learning-based performance interpretation was presented for snowboarding and skateboarding. In snowboarding, orientation features were extracted from automatically detected slopestyle trick performances. These features were then processed by machine learning algorithms in order to classify

the performed tricks. The trick classification could be used by amateurs to enhance their slope experience or be incorporated into professional training and competition broadcast. In skateboarding, tricks were classified based on orientation and further features. The board rotation during performed tricks was visualized by means of a 3D-graphic. The combination of trick classification and visualization was implemented in a real-time prototype, which was demonstrated to the skateboard community. The corresponding community perception on the implemented algorithms and technology in sports analytics in general was analyzed with regard to future work on this topic.

Besides these sports-related contributions, the overall combined contributions to the field of sports analysis can be seen in the establishment of new metrics, the simplification of kinematic analysis with IMUs and IMMUs, the application of machine learning for action classification in sports and the potential of orientation features for both the kinematic analysis and related performance interpretation. New metrics were introduced for all kinematic analyses. It was shown that by focusing on the orientation of athletes or corresponding equipment, new kinematic insight can be achieved for athletes, coaches, sports scientists and spectators. New metrics could be based on the upper body or shank angles of divers, the in-stroke rotation of a rowing boat and the continuous ski orientation. Kinematic analyses can be simplified by applying unobtrusive measurement hardware. Wearable IMUs and IMMUs can be applied in the presented and further sports for kinematic analysis instead of incorporating costly and heavy measurement equipment, such as underwater cameras or stationary hardware in wide measurement areas. Finally, all presented algorithms were based on the extraction of orientation features, which shows their potential for kinematic analysis and subsequent performance interpretation.

Future work could relate the presented algorithms and corresponding new measurement metrics to sports science. Innovative sports science methods could be established and possibly lead to new insight in motion analysis. Besides further scientific investigation, the proposed algorithms can be implemented in real-work applications, such as the training of athletes and support for competitions and corresponding broadcast. With the incorporated professional data in this thesis and the partial realization of the proposed algorithms in competitions, the applicability of the proposed methods to sports events was demonstrated and can be expanded in the future.

Finally, the results of this thesis indicate that there are many ways to enhance sports analytics with state-of-the-art technology. However, a remaining challenge is how to realize this development in the most effective way while at the same time respecting the origins of the sports and the demands of the sports community.

Bibliography

[1] Fullerton, H. S.: The inside game: The science of baseball. In: *The American Magazine* 70.1 (1910), 2–13.

[2] Link, D.: Sports analytics. In: *German Journal of Exercise and Sport Research* 48.1 (2018), 13–25.

[3] Lindsey, G. R.: An investigation of strategies in baseball. In: *Operations Research* 11.4 (1963), 477–501.

[4] Streib, N.; Young, S. J.; Sokol, J.: A major league baseball team uses operations research to improve draft preparation. In: *Interfaces* 42.2 (2012), 119–130.

[5] Baker, R. E.; Kwartler, T.: Sport analytics: Using open source logistic regression software to classify upcoming play type in the NFL. In: *Journal of Applied Sport Management* 7.2 (2015), 43–58.

[6] Orchard, J. W.: On the value of team medical staff: Can the 'Moneyball' approach be applied to injuries in professional football? In: *British Journal of Sports Medicine* 43.13 (2009), 963–965.

[7] Rossi, A.; Pappalardo, L.; Cintia, P.; Fernandez, J.; Iaia, F. M.; Medina, D.: Who is going to get hurt? Predicting injuries in professional soccer. In: *ECML Workshop on Machine Learning and Data Mining for Sports Analytics workshop (MLSA)*. Springer. 2017, 1–10.

[8] Abrams, G. D.; Harris, A. H.; Andriacchi, T. P.; Safran, M. R.: Biomechanical analysis of three tennis serve types using a markerless system. In: *British Journal of Sports Medicine* 48.4 (2014), 339–342.

[9] Elliott, B.; Marsh, T.; Blanksby, B.: A three-dimensional cinematographic analysis of the tennis serve. In: *International Journal of Sport Biomechanics* 2.4 (1986), 260–271.

[10] Elliott, B. C.; Marshall, R. N.; Noffal, G. J.: Contributions of upper limb segment rotations during the power serve in tennis. In: *Journal of Applied Biomechanics* 11.4 (1995), 433–442.

[11] Fleisig, G.; Nicholls, R.; Elliott, B.; Escamilla, R.: Tennis: Kinematics used by world class tennis players to produce high-velocity serves. In: *Sports Biomechanics* 2.1 (2003), 51–64.

[12] Reid, M.; Giblin, G.; Whiteside, D.: A kinematic comparison of the overhand throw and tennis serve in tennis players: How similar are they really? In: *Journal of Sports Sciences* 33.7 (2015), 713–723.

[13] Tubez, F.; Schwartz, C.; Paulus, J.; Croisier, J.-L.; Brüls, O.; Denoël, V.; Forthomme, B.: Which tool for a tennis serve evaluation? A review. In: *International Journal of Performance Analysis in Sport* 17.6 (2017), 1007–1033.

[14] Woods, C. T.; Raynor, A. J.; Bruce, L.; McDonald, Z.; Robertson, S.: The application of a multi-dimensional assessment approach to talent identification in Australian football. In: *Journal of Sports Sciences* 34.14 (2016), 1340–1345.

[15] Kautz, T.; Groh, B. H.; Hannink, J.; Jensen, U.; Strubberg, H.; Eskofier, B. M.: Activity recognition in beach volleyball using a deep convolutional neural network. In: *Data Mining and Knowledge Discovery* 31.6 (2017), 1678–1705.

[16] Nicholls, S. B.; Worsfold, P. R.: The observational analysis of elite coaches within youth soccer: The importance of performance analysis. In: *International Journal of Sports Science & Coaching* 11.6 (2016), 825–831.

[17] Thomas, S. V.; Gilbert, J. E.: Integrating technology to enhance athlete development: A literature review. In: *Journal of Higher Education Athletics & Innovation* 1.1 (2016), 73–84.

[18] Billings, A. C.; Angelini, J. R.; MacArthur, P. J.: Olympic television: Broadcasting the biggest show on earth. Routledge, 2017.

[19] Basole, R. C.; Saupe, D.: Sports data visualization. In: *IEEE Computer Graphics and Applications* 36.5 (2016), 24–26.

[20] Wang, B.: Evaluation of sports visualization based on wearable devices. In: *International Journal of Emerging Technologies in Learning* 12.12 (2017), 119–126.

[21] Howard, R. M.; Conway, R.; Harrison, A. J.: A survey of sensor devices: Use in sports biomechanics. In: *Sports Biomechanics* 15.4 (2016), 450–461.

[22] Keogh, J.; Espinosa, H.; Grigg, J.: Evolution of smart devices and human movement apps: Recommendations for use in sports science education and practice. In: *Journal of Fitness Research* 5.Special Issue (2016), 14–15.

[23] Renò, V.; Mosca, N.; Nitti, M.; D'Orazio, T.; Guaragnella, C.; Campagnoli, D.; Prati, A.; Stella, E.: A technology platform for automatic high-level tennis game analysis. In: *Computer Vision and Image Understanding* 159.1 (2017), 164–175.

[24] Ghosh, A.; Singh, S.; Jawahar, C.: Towards Structured Analysis of Broadcast Badminton Videos. In: *Winter Conference on Applications of Computer Vision (WACV)*. IEEE. 2018, 296–304.

[25] Malone, J. J.; Lovell, R.; Varley, M. C.; Coutts, A. J.: Unpacking the black box: Applications and considerations for using GPS devices in sport. In: *International Journal of Sports Physiology and Performance* 12.S2 (2017), 18–26.

[26] Scott, M. T.; Scott, T. J.; Kelly, V. G.: The validity and reliability of global positioning systems in team sport: A brief review. In: *The Journal of Strength & Conditioning Research* 30.5 (2016), 1470–1490.

[27] Vickery, W. M.; Dascombe, B. J.; Baker, J. D.; Higham, D. G.; Spratford, W. A.; Duffield, R.: Accuracy and reliability of GPS devices for measurement of sports-specific movement patterns related to cricket, tennis, and field-based team sports. In: *The Journal of Strength & Conditioning Research* 28.6 (2014), 1697–1705.

[28] Hoppe, M. W.; Baumgart, C.; Polglaze, T.; Freiwald, J.: Validity and reliability of GPS and LPS for measuring distances covered and sprint mechanical properties in team sports. In: *PloS one* 13.2 (2018), 1–21.

[29] Leser, R.; Baca, A.; Ogris, G.: Local positioning systems in (game) sports. In: *Sensors* 11.10 (2011), 9778–9797.

[30] Kautz, T.: Acquisition, filtering and analysis of positional and inertial data in sports. FAU University Press, 2017.

[31] Camomilla, V.; Bergamini, E.; Fantozzi, S.; Vannozzi, G.: Trends supporting the in-field use of wearable inertial sensors for sport performance evaluation: A systematic review. In: *Sensors* 18.3 (2018), 1–50.

[32] Cardinale, M.; Varley, M. C.: Wearable training-monitoring technology: Applications, challenges, and opportunities. In: *International Journal of Sports Physiology and Performance* 12.S2 (2017), 55–62.

[33] Chambers, R.; Gabbett, T. J.; Cole, M. H.; Beard, A.: The use of wearable microsensors to quantify sport-specific movements. In: *Sports Medicine* 45.7 (2015), 1065–1081.

[34] Thompson, W. R.: Worldwide survey of fitness trends for 2016. In: *ACSM Health & Fitness Journal* 19.6 (2015), 9–18.

[35] Adesida, Y.; Papi, E.; McGregor, A. H.: Exploring the role of wearable technology in sport kinematics and kinetics: A systematic review. In: *Sensors* 19.7 (2019), 1–26.

[36] Kautz, T.; Groh, B. H.; Eskofier, B. M.: Sensor fusion for multiplayer activity recognition in game sports. In: *KDD Workshop on Large-Scale Sports Analytics*. ACM. 2015, 1–4.

[37] Kaufmann, K.; An, K.: Biomechanics. In: *Kelley and Firestein's Textbook of Rheumatology*. Vol. 10. Elsevier, 2017. Chap. 6, 78–89.

[38] Leick, A.; Rapoport, L.; Tatarnikov, D.: GPS satellite surveying. John Wiley & Sons, 2015.

[39] García, S.; Luengo, J.; Herrera, F.: Tutorial on practical tips of the most influential data preprocessing algorithms in data mining. In: *Knowledge-Based Systems* 98.1 (2016), 1–29.

[40] Ferraris, F.; Grimaldi, U.; Parvis, M.: Procedure for effortless in-field calibration of three-axial rate gyro and accelerometers. In: *Sensors and Materials* 7.5 (1995), 311–330.

[41] Madgwick, S. O.; Harrison, A. J.; Vaidyanathan, R.: Estimation of IMU and MARG orientation using a gradient descent algorithm. In: *12th International Conference on Rehabilitation Robotics (ICORR)*. IEEE. 2011, 1–7.

[42] Kautz, T.; Groh, B. H.; Eskofier, B. M.: Augmented motion models for constrained position tracking with Kalman filters. In: *19th International Conference on Information Fusion (FUSION)*. IEEE. 2016, 849–854.

[43] Cust, E. E.; Sweeting, A. J.; Ball, K.; Robertson, S.: Machine and deep learning for sport-specific movement recognition: A systematic review of model development and performance. In: *Journal of Sports Sciences* 37.5 (2018), 568–600.

[44] Wagner, J. F.: About motion measurement in sports based on gyroscopes and accelerometers - An engineering point of view. In: *Gyroscopy and Navigation* 9.1 (2018), 1–18.

[45] Attal, F.; Mohammed, S.; Dedabrishvili, M.; Chamroukhi, F.; Oukhellou, L.; Amirat, Y.: Physical human activity recognition using wearable sensors. In: *Sensors* 15.12 (2015), 31314–31338.

[46] Wouda, F. J.; Giuberti, M.; Bellusci, G.; Maartens, E.; Reenalda, J.; Van Beijnum, B.-J. F.; Veltink, P. H.: Estimation of vertical ground reaction forces and sagittal knee kinematics during running using three inertial sensors. In: *Frontiers in Physiology* 9.1 (2018), 1–14.

[47] Fasel, B.; Spörri, J.; Schütz, P.; Lorenzetti, S.; Aminian, K.: Validation of functional calibration and strap-down joint drift correction for computing 3D joint angles of knee, hip, and trunk in alpine skiing. In: *PloS one* 12.7 (2017), 1–17.

[48] Yu, G.; Jang, Y. J.; Kim, J.; Kim, J. H.; Kim, H. Y.; Kim, K.; Panday, S. B.: Potential of IMU sensors in performance analysis of professional alpine skiers. In: *Sensors* 16.4 (2016), 1–21.

[49] Brock, H.; Ohgi, Y.: Development of an inertial motion capture system for kinematic analysis of ski jumping. In: *Proceedings of the Institution of Mechanical Engineers, Part P: Journal of Sports Engineering and Technology* 231.4 (2017), 275–286.

[50] Chardonnens, J.; Favre, J.; Cuendet, F.; Gremion, G.; Aminian, K.: A system to measure the kinematics during the entire ski jump sequence using inertial sensors. In: *Journal of Biomechanics* 46.1 (2013), 56–62.

[51] Blank, P.; Groh, B. H.; Eskofier, B. M.: Ball speed and spin estimation in table tennis using a racket-mounted inertial sensor. In: *21st International Symposium on Wearable Computers (ISWC)*. ACM. 2017, 2–9.

[52] Zrenner, M.; Ullrich, M.; Zobel, P.; Jensen, U.; Laser, F.; Groh, B. H.; Duemler, B.; Eskofier, B. M.: Kinematic parameter evaluation for the purpose of a wearable running shoe recommendation. In: *15th International Conference on Wearable and Implantable Body Sensor Networks (BSN)*. IEEE. 2018, 106–109.

[53] Fantozzi, S.; Giovanardi, A.; Borra, D.; Gatta, G.: Gait kinematic analysis in water using wearable inertial magnetic sensors. In: *PloS one* 10.9 (2015), 1–12.

[54] Mangia, A. L.; Cortesi, M.; Fantozzi, S.; Giovanardi, A.; Borra, D.; Gatta, G.: The use of IMMUs in a water environment: Instrument validation and application of 3D multi-body kinematic analysis in medicine and sport. In: *Sensors* 17.4 (2017), 1–21.

[55] Ekanayake, S. W.; Morris, A. J.; Forrester, M.; Pathirana, P. N.: Biokin: An ambulatory platform for gait kinematic and feature assessment. In: *Healthcare Technology Letters* 2.1 (2015), 40–45.

[56] Strohrmann, C.; Harms, H.; Tröster, G.; Hensler, S.; Müller, R.: Out of the lab and into the woods: Kinematic analysis in running using wearable sensors. In: *13th International Conference on Ubiquitous Computing (UbiComp)*. ACM. 2011, 119–122.

[57] Struzik, A.; Konieczny, G.; Stawarz, M.; Grzesik, K.; Winiarski, S.; Rokita, A.: Relationship between lower limb angular kinematic variables and the effectiveness of sprinting during the acceleration phase. In: *Applied Bionics and Biomechanics* 2016.1 (2016), 1–9.

[58] McGinnis, R. S.; Cain, S. M.; Davidson, S. P.; Vitali, R. V.; Perkins, N. C.; McLean, S. G.: Quantifying the effects of load carriage and fatigue under load on sacral kinematics during countermovement vertical jump with IMU-based method. In: *Sports Engineering* 19.1 (2016), 21–34.

[59] Seuter, M.; Opitz, L.; Bauer, G.; Hochmann, D.: Live-feedback from the IMUs: Animated 3D visualization for everyday-exercising. In: *International Joint Conference on Pervasive and Ubiquitous Computing (UbiComp)*. ACM. 2016, 904–907.

[60] Sattar, F.; Azad, A. A. M.; Sikder, S.; Arefin, M. S.: Body sensor networks for monitoring performances in sports: A brief overview and some new thoughts. In: *Artificial Intelligence Research* 8.1 (2019), 25–40.

[61] Lee, J. B.; Mellifont, R. B.; Burkett, B. J.; James, D. A.: Detection of illegal race walking: A tool to assist coaching and judging. In: *Sensors* 13.12 (2013), 16065–16074.

[62] Schuldhaus, D.; Jakob, C.; Zwick, C.; Koerger, H.; Eskofier, B. M.: Your personal movie producer: Generating highlight videos in soccer using wearables. In: *20th International Symposium on Wearable Computers (ISWC)*. ACM. 2016, 80–83.

[63] Magalhães, F. A.; Vannozzi, G.; Gatta, G.; Fantozzi, S.: Wearable inertial sensors in swimming motion analysis: A systematic review. In: *Journal of Sports Sciences* 33.7 (2015), 732–745.

[64] Mooney, R.; Corley, G.; Godfrey, A.; Quinlan, L. R.; ÓLaighin, G.: Inertial sensor technology for elite swimming performance analysis: A systematic review. In: *Sensors* 16.1 (2016), 1–55.

[65] Guignard, B.; Rouard, A.; Chollet, D.; Seifert, L.: Behavioral dynamics in swimming: The appropriate use of inertial measurement units. In: *Frontiers in Psychology* 8.1 (2017), 1–16.

[66] Pansiot, J.; Lo, B.; Yang, G.-Z.: Swimming stroke kinematic analysis with BSN. In: *International Conference on Body Sensor Networks (BSN)*. IEEE. 2010, 153–158.

[67] Staniak, Z.; Buśko, K.; Górski, M.; Pastuszak, A.: Accelerometer profile of motion of the pelvic girdle in breaststroke swimming. In: *Journal of Human Kinetics* 52.1 (2016), 147–156.

[68] Daukantas, S.; Marozas, V.; Lukosevicius, A.; Jegelevicius, D.; Kybartas, D.: Video and inertial sensors based estimation of kinematical parameters in swimming sport. In: *6th International Conference on Intelligent Data Acquisition and Advanced Computing Systems (IDAACS)*. IEEE. 2011, 408–411.

[69] Dadashi, F.; Crettenand, F.; Millet, G. P.; Aminian, K.: Front-crawl instantaneous velocity estimation using a wearable inertial measurement unit. In: *Sensors* 12.10 (2012), 12927–12939.

[70] Dadashi, F.; Crettenand, F.; Millet, G. P.; Seifert, L.; Komar, J.; Aminian, K.: Automatic front-crawl temporal phase detection using adaptive filtering of inertial signals. In: *Journal of Sports Sciences* 31.11 (2013), 1251–1260.

[71] Dadashi, F.; Millet, G. P.; Aminian, K.: A Bayesian approach for pervasive estimation of breaststroke velocity using a wearable IMU. In: *Pervasive and Mobile Computing* 19.1 (2015), 37–46.

[72] Fantozzi, S.; Giovanardi, A.; Magalhães, F. A.; Di Michele, R.; Cortesi, M.; Gatta, G.: Assessment of three-dimensional joint kinematics of the upper limb during simulated swimming using wearable inertial-magnetic measurement units. In: *Journal of Sports Sciences* 34.11 (2016), 1073–1080.

[73] Magalhães, F. A.; Giovanardi, A.; Di Michele, R.; Cortesi, M.; Gatta, G.; Fantozzi, S.: Swimming motion analysis: 3D joints kinematics of the upper limb using wearable inertial and magnetic sensors. In: *13th International Symposium on 3D Analysis of Human Movement (3D-AHM)*. ISB. 2014, 180–183.

[74] Samimy, S.; Mollendorf, J. C.; Pendergast, D. R.: A theoretical and experimental analysis of diver technique in underwater fin swimming. In: *Sports Engineering* 8.1 (2005), 27–38.

[75] Steinberg, F.; Dräger, T.; Steegmanns, A.; Dalecki, M.; Röschmann, M.; Hoffmann, U.: fit2dive-A field test for assessing the specific capability of underwater fin swimming with SCUBA. In: *International Journal of Performance Analysis in Sport* 11.1 (2011), 197–208.

[76] Walker, C. R.; Anderson, I. A.: Monitoring diver kinematics with dielectric elastomer sensors. In: *Electroactive Polymer Actuators and Devices (EAPAD)*. SPIE. 2017, 1–11.

[77] Kuch, B.; Haasl, S.; Wagner, M.; Buttazzo, G.; Sieber, A.: Preliminary report: Embedded platform for inertial based underwater navigation. In: *9th Workshop on Intelligent Solutions in Embedded Systems (WISES)*. IEEE. 2011, 101–108.

[78] Goodfellow, G. M.; Neasham, J. A.; Rendulić, I.; Nađ, Đ.; Mišković, N.: DiverNet - A network of inertial sensors for real time diver visualization. In: *Sensors Applications Symposium (SAS)*. IEEE. 2015, 1–6.

[79] Soper, C.; Hume, P. A.: Towards an ideal rowing technique for performance. In: *Sports Medicine* 34.12 (2004), 825–848.

[80] Smith, R. M.; Loschner, C.: Biomechanics feedback for rowing. In: *Journal of Sports Sciences* 20.10 (2002), 783–791.

[81] Smith, R.; Draper, C.: Quantitative characteristics of coxless pair-oar rowing. In: *20th International Symposium on Biomechanics in Sports*. ISBS. 2002, 263–266.

[82] McGregor, A. H.; Bull, A. M.; Byng-Maddick, R.: A comparison of rowing technique at different stroke rates: A description of sequencing, force production and kinematics. In: *International Journal of Sports Medicine* 25.6 (2004), 465–470.

[83] Buckeridge, E. M.; Bull, A. M.; McGregor, A. H.: Biomechanical determinants of elite rowing technique and performance. In: *Scandinavian Journal of Medicine & Science in Sports* 25.2 (2015), 176–183.

[84] Kleshnev, V.: Boat acceleration, temporal structure of the stroke cycle, and effectiveness in rowing. In: *Proceedings of the Institution of Mechanical Engineers, Part P: Journal of Sports Engineering and Technology* 224.1 (2010), 63–74.

[85] Tessendorf, B.; Gravenhorst, F.; Arnrich, B.; Tröster, G.: An IMU-based sensor network to continuously monitor rowing technique on the water. In: *7th International Conference on Intelligent Sensors, Sensor Networks and Information Processing (ISSNIP)*. IEEE. 2011, 253–258.

[86] Bosch, S.; Shoaib, M.; Geerlings, S.; Buit, L.; Meratnia, N.; Havinga, P.: Analysis of indoor rowing motion using wearable inertial sensors. In: *10th International Conference on Body Area Networks (BodyNets)*. ICST. 2015, 233–239.

[87] King, R. C.; McIlwraith, D. G.; Lo, B.; Pansiot, J.; McGregor, A. H.; Yang, G.-Z.: Body sensor networks for monitoring rowing technique. In: *6th International Workshop on Wearable and Implantable Body Sensor Networks (BSN)*. IEEE. 2009, 251–255.

[88] Gravenhorst, F.; Turner, T.; Draper, C.; Smith, R. M.; Troester, G.: Validation of a rowing oar angle measurement system based on an inertial measurement unit. In: *12th IEEE International Conference on Trust, Security and Privacy in Computing and Communications (TrustCom)*. IEEE. 2013, 1412–1419.

[89] Gravenhorst, F.; Muaremi, A.; Kottmann, F.; Troster, G.; Sigrist, R.; Gerig, N.; Draper, C.: Strap and row: Rowing technique analysis based on inertial measurement units implemented in mobile phones. In: *9th International Conference on Intelligent Sensors, Sensor Networks and Information Processing (ISSNIP)*. IEEE. 2014, 1–6.

[90] Serveto, S.; Barré, S.; Kobus, J.-M.; Mariot, J.-P.: A three-dimensional model of the boat–oars–rower system using ADAMS and LifeMOD commercial software. In: *Proceedings of the Institution of Mechanical Engineers, Part P: Journal of Sports Engineering and Technology* 224.1 (2010), 75–88.

[91] Gravenhorst, F.; Tessendorf, B.; Arnrich, B.; Tröster, G.: Analyzing rowing crews in different rowing boats based on angular velocity measurements with gyroscopes. In: *8th International Symposium on Computer Science in Sport (IACSS)*. IACSS. 2011, 1–4.

[92] Sinclair, P. J.; Greene, A. J.; Smith, R.: The effects of horizontal and vertical forces on single scull boat orientation while rowing. In: *27th International Conference on Biomechanics in Sports*. ISBS. 2009, 1–4.

[93] Wagner, J.; Bartmus, U.; De Marees, H.: Three-axes gyro system quantifying the specific balance of rowing. In: *International Journal of Sports Medicine* 14.S1 (1993), 35–38.

[94] Loschner, C.; Smith, R.; Galloway, M.: Intra-stroke boat orientation during single sculling. In: *18th International Symposium on Biomechanics in Sports*. ISBS. 2000, 1–4.

[95] Chardonnens, J.; Favre, J.; Cuendet, F.; Gremion, G.; Aminian, K.: Analysis of stable flight in ski jumping based on parameters measured with a wearable system. In: *28th International Conference on Biomechanics in Sports*. ISBS. 2010, 273–276.

[96] Chardonnens, J.; Favre, J.; Le Callennec, B.; Cuendet, F.; Gremion, G.; Aminian, K.: Automatic measurement of key ski jumping phases and temporal events with a wearable system. In: *Journal of Sports Sciences* 30.1 (2012), 53–61.

[97] Chardonnens, J.; Favre, J.; Cuendet, F.; Gremion, G.; Aminian, K.: Measurement of the dynamics in ski jumping using a wearable inertial sensor-based system. In: *Journal of Sports Sciences* 32.6 (2014), 591–600.

[98] Bächlin, M.; Kusserow, M.; Tröster, G.; Gubelmann, H.: Ski jump analysis of an Olympic champion with wearable acceleration sensors. In: *14th International Symposium on Wearable Computers (ISWC)*. IEEE. 2010, 1–2.

[99] Logar, G.; Munih, M.: Estimation of joint forces and moments for the in-run and take-off in ski jumping based on measurements with wearable inertial sensors. In: *Sensors* 15.5 (2015), 11258–11276.

[100] Fang, X.; Göttlicher, C.; Holzapfel, F.: Attitude estimation of skis in ski jumping using low-cost inertial measurement units. In: *Proceedings* 2.6 (2018), 1–6.

[101] Brock, H.; Ohgi, Y.; Seo, K.: Development of an automated motion evaluation system from wearable sensor devices for ski jumping. In: *Procedia Engineering* 147.1 (2016), 694–699.

[102] Brock, H.; Ohgi, Y.: Assessing motion style errors in ski jumping using inertial sensor devices. In: *IEEE Sensors Journal* 17.12 (2017), 3794–3804.

[103] Harding, J. W.; Mackintosh, C. G.; Hahn, A. G.; James, D. A.: Classification of aerial acrobatics in elite half-pipe snowboarding using body mounted inertial sensors. In: *The Engineering of Sport 7*. Vol. 2. Springer, 2008. Chap. P237, 447–456.

[104] Harding, J. W.; Mackintosh, C. G.; Martin, D. T.; James, D. A.: Automated scoring for elite half-pipe snowboard competition: Important sporting development or techno distraction? In: *Sports Technology* 1.6 (2008), 277–290.

[105] Spelmezan, D.; Borchers, J.: Real-time snowboard training system. In: *Conference on Human Factors in Computing Systems (CHI)*. ACM. 2008, 3327–3332.

[106] Spelmezan, D.; Schanowski, A.; Borchers, J.: Wearable automatic feedback devices for physical activities. In: *4th International Conference on Body Area Networks (BodyNets)*. ICST. 2009, 1–8.

[107] Holleczek, T.; Zysset, C.; Arnrich, B.; Roggen, D.; Tröster, G.: Towards an interactive snowboarding assistance system. In: *13th International Symposium on Wearable Computers (ISWC)*. IEEE. 2009, 147–148.

[108] Holleczek, T.; Schoch, J.; Arnrich, B.; Tröster, G.: Recognizing turns and other snowboarding activities with a gyroscope. In: *14th International Symposium on Wearable Computers (ISWC)*. IEEE. 2010, 1–8.

[109] Holleczek, T.; Rüegg, A.; Harms, H.; Tröster, G.: Textile pressure sensors for sports applications. In: *9th Annual IEEE Conference on Sensors*. IEEE. 2010, 732–737.

[110] Krüger, A.; Edelmann-Nusser, J.: Biomechanical analysis in freestyle snowboarding: Application of a full-body inertial measurement system and a bilateral insole measurement system. In: *Sports Technology* 2.1-2 (2009), 17–23.

[111] Krüger, A.; McAlpine, P.; Borrani, F.; Edelmann-Nusser, J.: Determination of three-dimensional joint loading within the lower extremities in snowboarding. In: *Proceedings of the Institution of Mechanical Engineers, Part H: Journal of Engineering in Medicine* 226.2 (2012), 170–175.

[112] Lee, T. J.; Zihajehzadeh, S.; Loh, D.; Hoskinson, R.; Park, E. J.: Automatic jump detection in skiing/snowboarding using head-mounted MEMS inertial and pressure sensors. In: *Proceedings of the Institution of Mechanical Engineers, Part P: Journal of Sports Engineering and Technology* 229.4 (2015), 278–287.

[113] Moeyersons, B.; Fuss, F. K.; Tan, A. M.; Weizman, Y.: Biofeedback system for novice snowboarding. In: *Procedia Engineering* 147.1 (2016), 781–786.

[114] Anlauff, J.; Weitnauer, E.; Lehnhardt, A.; Schirmer, S.; Zehe, S.; Tonekaboni, K.: A method for outdoor skateboarding video games. In: *7th International Conference on Advances in Computer Entertainment Technology (ACE)*. ACM. 2010, 40–44.

[115] Reynell, E.; Thinyane, H.: Hardware and software for skateboard trick visualisation on a mobile phone. In: *South African Institute for Computer Scientists and Information Technologists Conference (SAICSIT)*. ACM. 2012, 253–261.

[116] Pijnappel, S.; Mueller, F.: Designing interactive technology for skateboarding. In: *8th International Conference on Tangible, Embedded and Embodied Interaction (TEI)*. ACM. 2014, 141–148.

[117] Ghosh, S.; Shah, P.; Navarro, L.; Chen, X.: MusiSkate: Enhancing the skateboarding experience through musical feedback. In: *18th International Conference on Human-Computer Interaction with Mobile Devices and Services Adjunct (MobileHCI)*. ACM. 2016, 753–759.

[118] Park, H. K.; Yi, H.; Lee, W.: Recording and sharing non-visible information on body movement while skateboarding. In: *Conference on Human Factors in Computing Systems (CHI)*. ACM. 2017, 2488–2492.

[119] Corrêa, N. K.; Lima, J. C. de; Russomano, T.; Santos, M. A. dos: Development of a skateboarding trick classifier using accelerometry and machine learning. In: *Research on Biomedical Engineering* 33.4 (2017), 362–369.

[120] Abdullah, M. A.; Ibrahim, M. A. R.; Shapiee, M. N. A. B.; Razman, M. A. M.; Musa, R. M.; Majeed, A. P. A.: The classification of skateboarding trick manoeuvres through the integration of IMU and machine learning. In: *2nd Symposium on Intelligent Manufacturing and Mechatronics (SympoSIMM)*. Springer. 2019, 67–74.

[121] Shaeffer, D. K.: MEMS inertial sensors: A tutorial overview. In: *IEEE Communications Magazine* 51.4 (2013), 100–109.

[122] Cai, Y.; Zhao, Y.; Ding, X.; Fennelly, J.: Magnetometer basics for mobile phone applications. Tech. rep. Electronic Products: Sensors and Transducers, 2012.

[123] Lenz, J.; Edelstein, S.: Magnetic sensors and their applications. In: *IEEE Sensors Journal* 6.3 (2006), 631–649.

[124] Ramsden, E.: Hall-effect sensors: Theory and application. Elsevier, 2011.

[125] Aggarwal, P.; Syed, Z.; Niu, X.; El-Sheimy, N.: A standard testing and calibration procedure for low cost MEMS inertial sensors and units. In: *The Journal of Navigation* 61.2 (2008), 323–336.

[126] Nassar, S.: Improving the inertial navigation system (INS) error model for INS and INS/DGPS applications. PhD thesis. Calgary, AB, Canada: University of Calgary, Department of Geomatics Engineering, 2003.

[127] Niu, X.; Li, Y.; Zhang, H.; Wang, Q.; Ban, Y.: Fast thermal calibration of low-grade inertial sensors and inertial measurement units. In: *Sensors* 13.9 (2013), 12192–12217.

[128] Gebre-Egziabher, D.; Elkaim, G. H.; David Powell, J.; Parkinson, B. W.: Calibration of strapdown magnetometers in magnetic field domain. In: *Journal of Aerospace Engineering* 19.2 (2006), 87–102.

[129] Skog, I.; Händel, P.; Nilsson, J.-O.; Rantakokko, J.: Zero-velocity detection - An algorithm evaluation. In: *IEEE Transactions on Biomedical Engineering* 57.11 (2010), 2657–2666.

[130] Bonnet, S.; Bassompierre, C.; Godin, C.; Lesecq, S.; Barraud, A.: Calibration methods for inertial and magnetic sensors. In: *Sensors and Actuators A: Physical* 156.2 (2009), 302–311.

[131] Renaudin, V.; Afzal, M. H.; Lachapelle, G.: Complete triaxis magnetometer calibration in the magnetic domain. In: *Journal of Sensors* 2010.1 (2010), 1–10.

[132] Shuster, M. D.: The generalized Wahba problem. In: *Journal of the Astronautical Sciences* 54.2 (2006), 245–259.

[133] Wahba, G.: A least squares estimate of satellite attitude. In: *SIAM Review* 7.3 (1965), 409–409.

[134] Markley, F. L.; Mortari, D.: Quaternion attitude estimation using vector observations. In: *Journal of the Astronautical Sciences* 48.2 (2000), 359–380.

[135] Davenport, P. B.: Attitude determination and sensor alignment via weighted least squares affine transformations. In: *AAS/AIAA Astrodynamics specialists conference*. AAS. 1971, 1–35.

[136] Markley, F. L.: Attitude determination using vector observations and the singular value decomposition. In: *Journal of the Astronautical Sciences* 36.3 (1988), 245–258.

[137] Blank, P.; Kugler, P.; Schlarb, H.; Eskofier, B.: A wearable sensor system for sports and fitness applications. In: *19th Annual Congress of the European College of Sport Science (ECSS)*. ECSS. 2014, 703.

[138] Invensense: MPU-9150 data sheet (Rev. 4.3). [Online]. https://www.invensense.com/wp-content/uploads/2015/02/MPU-9150-Datasheet.pdf [Accessed: August 31, 2019]. 2013.

[139] Shimmer: Shimmer3 data sheet (Rev 1.4). [Online]. http://www.shimmersensing.com/images/uploads/docs/Shimmer3_Spec_1.4.pdf [Accessed: August 31, 2019]. 2013.

[140] Analog Devices: ADXL330 data sheet (Rev. A). [Online]. http://www.analog.com/media/en/technical-documentation/data-sheets/ADXL330.pdf [Accessed: August 31, 2019]. 2007.

[141] Diebel, J.: Representing attitude: Euler angles, unit quaternions, and rotation vectors. In: *Matrix* 58.15-16 (2006), 1–35.

[142] Kuipers, J. B.: Quaternions and rotation sequences: A primer with applications to orbits, aerospace, and virtual reality. Princeton University Press, 1999.

[143] Pujol, J.: Hamilton, Rodrigues, Gauss, quaternions, and rotations: A historical reassessment. In: *Communications in Mathematical Analysis* 13.2 (2012), 1–14.

[144] Cirillo, A.; Cirillo, P.; De Maria, G.; Natale, C.; Pirozzi, S.: A comparison of multisensor attitude estimation algorithms. In: *Multisensor Attitude Estimation: Fundamental Concepts and Applications*. Vol. 1. Taylor & Francis, 2016. Chap. 29, 529–540.

[145] Chen, Z.: Bayesian filtering: From Kalman filters to particle filters, and beyond. Tech. rep. Communications Research Laboratory, McMaster University, Hamilton, ON, Canada, 2003.

[146] Kalman, R. E.: A new approach to linear filtering and prediction problems. In: *Journal of Basic Engineering* 82.1 (1960), 35–45.

[147] Welch, G.; Bishop, G.: An introduction to the Kalman filter. Tech. rep. Department of Computer Science, University of North Carolina, Chapel Hill, NC, USA, 1995.

[148] Julier, S. J.; Uhlmann, J. K.: New extension of the Kalman filter to nonlinear systems. In: *11th International Symposium on Aerospace/Defense Sensing, Simulation and Controls (AeroSense)*. SPIE. 1997, 182–194.

[149] Carpenter, J.; Clifford, P.; Fearnhead, P.: Improved particle filter for nonlinear problems. In: *IEE Proceedings - Radar, Sonar and Navigation* 146.1 (1999), 2–7.

[150] Kitagawa, G.: Monte Carlo filter and smoother for non-Gaussian nonlinear state space models. In: *Journal of Computational and Graphical Statistics* 5.1 (1996), 1–25.

[151] Jain, A. K.; Duin, R. P.; Mao, J.: Statistical pattern recognition: A review. In: *IEEE Transactions on Pattern Analysis and Machine Intelligence* 22.1 (2000), 4–37.

[152] Duda, R. O.; Hart, P. E.; Stork, D. G.: Pattern classification. John Wiley & Sons, 2012.

[153] Kotsiantis, S. B.; Zaharakis, I.; Pintelas, P.: Supervised machine learning: A review of classification techniques. In: *Informatica* 31.3 (2007), 249–268.

[154] Bruening, D. A.; Reynolds, R. E.; Adair, C. W.; Zapalo, P.; Ridge, S. T.: A sport-specific wearable jump monitor for figure skating. In: *PloS one* 13.11 (2018), 1–13.

[155] Kos, M.; Kramberger, I.: A wearable device and system for movement and biometric data acquisition for sports applications. In: *IEEE Access* 5.1 (2017), 6411–6420.

[156] Sadi, F.; Klukas, R.; Hoskinson, R.: Precise air time determination of athletic jumps with low-cost MEMS inertial sensors using multiple attribute decision making. In: *Sports Technology* 6.2 (2013), 63–77.

[157] Guyon, I.; Elisseeff, A.: An introduction to feature extraction. In: *Feature Extraction*. Vol. 1. Springer, 2006. Chap. 1, 1–25.

[158] Bengio, Y.; Courville, A.; Vincent, P.: Representation learning: A review and new perspectives. In: *IEEE Transactions on Pattern Analysis and Machine Intelligence* 35.8 (2013), 1798–1828.

[159] Avci, A.; Bosch, S.; Marin-Perianu, M.; Marin-Perianu, R.; Havinga, P.: Activity recognition using inertial sensing for healthcare, wellbeing and sports applications: A survey. In: *23rd International Conference on Architecture of Computing Systems (ARCS)*. VDE. 2010, 1–10.

[160] Tang, J.; Alelyani, S.; Liu, H.: Feature selection for classification: A review. In: *Data Classification: Algorithms and Applications*. Vol. 1. CRC Press, 2014. Chap. 2, 38–60.

[161] Saeys, Y.; Inza, I.; Larrañaga, P.: A review of feature selection techniques in bioinformatics. In: *Bioinformatics* 23.19 (2007), 2507–2517.

[162] Peng, H.; Long, F.; Ding, C.: Feature selection based on mutual information criteria of max-dependency, max-relevance, and min-redundancy. In: *IEEE Transactions on Pattern Analysis and Machine Intelligence* 27.8 (2005), 1226–1238.

[163] Robnik-Šikonja, M.; Kononenko, I.: Theoretical and empirical analysis of ReliefF and RReliefF. In: *Machine Learning* 53.1–2 (2003), 23–69.

[164] Guyon, I.; Elisseeff, A.: An introduction to variable and feature selection. In: *Journal of Machine Learning Research* 3.Mar (2003), 1157–1182.

[165] Guyon, I.; Weston, J.; Barnhill, S.; Vapnik, V.: Gene selection for cancer classification using support vector machines. In: *Machine Learning* 46.1-3 (2002), 389–422.

[166] Cover, T.; Hart, P.: Nearest neighbor pattern classification. In: *IEEE Transactions on Information Theory* 13.1 (1967), 21–27.

[167] Lewis, D. D.: Naive (Bayes) at forty: The independence assumption in information retrieval. In: *10th European Conference on Machine Learning (ECML)*. Springer. 1998, 4–15.

[168] Breiman, L.; Friedman, J. H.; Olshen, R. A.; Stone, C. J.: Classification and regression trees. CRC Press, 1984.

[169] Quinlan, J. R.: C4.5: Programs for machine learning. Morgan Kaufmann, 1992.

[170] Breiman, L.: Random forests. In: *Machine Learning* 45.1 (2001), 5–32.

[171] Cortes, C.; Vapnik, V.: Support-vector networks. In: *Machine Learning* 20.3 (1995), 273–297.

[172] Hsu, C.-W.; Chang, C.-C.; Lin, C.-J.: A practical guide to support vector classification. Tech. rep. Department of Computer Science, National Taiwan University, Taipei, Taiwan, 2003.

[173] Kinovea. [Online]. http://www.kinovea.org/ [Accessed: August 31, 2019]. 2019.

[174] Berndt, D. J.; Clifford, J.: Using dynamic time warping to find patterns in time series. In: *KDD Workshop on Knowledge Discovery in Databases*. AAAI. 1994, 359–370.

[175] Müller, M.: Dynamic time warping. In: *Information Retrieval for Music and Motion*. Vol. 1. Springer, 2007. Chap. 4, 69–84.

[176] Gradl, S.; Cibis, T.; Lauber, J.; Richer, R.; Rybalko, R.; Pfeiffer, N.; Leutheuser, H.; Wirth, M.; Tscharner, V. von; Eskofier, B. M.: Wearable current-based ECG monitoring system with non-insulated electrodes for underwater application. In: *Applied Sciences* 7.12 (2017), 1–15.

[177] Cibis, T.; Groh, B. H.; Gatermann, H.; Leutheuser, H.; Eskofier, B. M.: Wearable real-time ECG monitoring with emergency alert system for scuba diving. In: *37th Annual International Conference of the IEEE Engineering in Medicine and Biology Society (EMBC)*. IEEE. 2015, 6074–6077.

[178] Kleshnev, V.: Propulsive efficiency of rowing. In: *17th International Symposium on Biomechanics in Sports*. ISBS. 1999, 69–72.

[179] Kruk, E. van der; Reijne, M. M.: Accuracy of human motion capture systems for sport applications; state-of-the-art review. In: *European Journal of Sport Science* 18.6 (2018), 806–819.

[180] Begon, M.; Colloud, F.; Fohanno, V.; Bahuaud, P.; Monnet, T.: Computation of the 3D kinematics in a global frame over a 40 m-long pathway using a rolling motion analysis system. In: *Journal of Biomechanics* 42.16 (2009), 2649–2653.

[181] Colloud, F.; Chèze, L.; André, N.; Bahuaud, P.: An innovative solution for 3D kinematics measurement for large volumes. In: *Journal of Biomechanics* 41.S1 (2008), S57.

[182] Kersting, U. G.; Kurpiers, N.; Darlow, B. J. S.; Nolte, V. W.: Three-dimensional assessment of on water rowing technique: A methodological study. In: *26th International Conference on Biomechanics in Sports*. ISBS. 2008, 72.

[183] Swiss Timing: Timing & Scoring System. [Online]. https://www.swisstiming.com/fileadmin/Resources/Data/Datasheets/DOCM_BT_CC_Timing-Scoring_1215_EN.pdf [Accessed: August 31, 2019]. 2016.

[184] FIS: Certificate of jumping hill, no. 58 / GER 47, Oberwiesenthal. [Online]. http://medias4.fis-ski.com/pdf/homologations/JP/GER/58_GER_47_Oberwiesenthal_HS106.pdf [Accessed: August 31, 2019]. 2014.

[185] Schwameder, H.: Biomechanics research in ski jumping, 1991–2006. In: *Sports Biomechanics* 7.1 (2008), 114–136.

[186] Rabiner, L. R.: A tutorial on hidden Markov models and selected applications in speech recognition. In: *Proceedings of the IEEE* 77.2 (1989), 257–286.

[187] Fine, S.; Singer, Y.; Tishby, N.: The hierarchical hidden Markov model: Analysis and applications. In: *Machine Learning* 32.1 (1998), 41–62.

[188] Panahandeh, G.; Mohammadiha, N.; Leijon, A.; Händel, P.: Continuous hidden Markov model for pedestrian activity classification and gait analysis. In: *IEEE Transactions on Instrumentation and Measurement* 62.5 (2013), 1073–1083.

[189] Savage, P. G.: Strapdown inertial navigation integration algorithm design part 2: Velocity and position algorithms. In: *Journal of Guidance, Control, and Dynamics* 21.2 (1998), 208–221.

[190] FIS: Standards for the construction of jumping hills. [Online]. https://res.cloudinary.com/fis-production/image/upload/v1536927748/fis-prod/assets/Standards_for_the_Construction_of_Jumping_Hills.pdf [Accessed: August 31, 2019]. 2015.

[191] FIS: The International ski competition rules (ICR). [Online]. https://res.cloudinary.com/fis-production/image/upload/v1536927329/fis-prod/assets/International_Competition_Rules_ICR_Ski_Jumping.pdf [Accessed: August 31, 2019]. 2018.

[192] Fritz, J.; Kröll, J.; Jenny, H.; Schwameder, H.: In-field measurement of vertical and horizontal forces in ski-jumping: Evaluation of a portable two-dimensional force plate. In: *Proceedings of the Institution of Mechanical Engineers, Part P: Journal of Sports Engineering and Technology* 233.1 (2019), 126–134.

[193] Groh, B. H.; Fritz, J.; Deininger, M.; Schwameder, H.; Eskofier, B. M.: Unobtrusive and wearable landing momentum estimation in ski jumping with inertial-magnetic sensors. In: *15th International Conference on Wearable and Implantable Body Sensor Networks (BSN)*. IEEE. 2018, 102–105.

[194] Wagner, W.; Horel, J.: Observations and simulations of snow surface temperature on cross-country ski racing courses. In: *Cold Regions Science and Technology* 66.1 (2011), 1–11.

[195] Fontanella, R.; Accardo, D.; Moriello, R. S. L.; Angrisani, L.; Simone, D. D.: An innovative strategy for accurate thermal compensation of gyro bias in inertial units by exploiting a novel augmented Kalman filter. In: *Sensors* 18.5 (2018), 1–19.

[196] Prikhodko, I. P.; Trusov, A. A.; Shkel, A. M.: Compensation of drifts in high-Q MEMS gyroscopes using temperature self-sensing. In: *Sensors and Actuators A: Physical* 201.1 (2013), 517–524.

[197] Zhang, B.; Chu, H.; Sun, T.; Guo, L.: Thermal calibration of a tri-axial MEMS gyroscope based on parameter-interpolation method. In: *Sensors and Actuators A: Physical* 261.1 (2017), 103–116.

[198] Domingos, P.: Metacost: A general method for making classifiers cost-sensitive. In: *5th International Conference on Knowledge Discovery and Data Mining*. ACM. 1999, 155–164.

[199] Powers, D. M.: Evaluation: From precision, recall and F-measure to ROC, informedness, markedness and correlation. In: *Journal of Machine Learning Technologies* 2.1 (2011), 37–63.

[200] Ring, M.; Jensen, U.; Kugler, P.; Eskofier, B.: Software-based performance and complexity analysis for the design of embedded classification systems. In: *21st International Conference on Pattern Recognition*. IEEE. 2012, 2266–2269.

[201] Park, H. K.; Lee, W.: Motion echo snowboard: Visualizing weight distribution on snowboard. In: *Conference on Human Factors in Computing Systems (CHI)*. ACM. 2016, 3746–3749.

[202] Pedregosa, F. et al.: Scikit-learn: Machine learning in Python. In: *Journal of Machine Learning Research* 12.Oct (2011), 2825–2830.

[203] X-IO Technologies: Open source IMU and AHRS algorithms. [Online]. http://www.x-io.co.uk/open-source-imu-and-ahrs-algorithms/ [Accessed: August 31, 2019]. 2012.

[204] Virbel, M.; Hansen, T. E.; Lobunets, O.: Kivy - A framework for rapid creation of innovative user interfaces. In: *Workshop-Proceedings der Tagung Mensch & Computer*. Universitätsverlag Chemnitz. 2011, 69–73.

[205] Friedrich-Alexander-Universität Erlangen-Nürnberg: Skateboard trick classification & visualization. [Online]. https://www.mad.tf.fau.de/files/2019/08/skateboard-application.mp4 [Accessed: August 31, 2019] or http://www5.cs.fau.de/files/skateboard-application.mpg [Accessed: August 31, 2019]. 2019.

[206] Joshi, A.; Kale, S.; Chandel, S.; Pal, D.: Likert scale: Explored and explained. In: *British Journal of Applied Science & Technology* 7.4 (2015), 396–403.

[207] Likert, R.: A technique for the measurement of attitudes. In: *Archives of Psychology* 22.140 (1932), 1–55.

[208] Flaschka, J.: Estimation and visualization of skateboard pressure distribution. Bachelor's thesis. Erlangen, Germany: Friedrich-Alexander-Universität Erlangen-Nürnberg, Pattern Recognition Lab, 2017.

[209] Shih, H.-C.: A survey of content-aware video analysis for sports. In: *IEEE Transactions on Circuits and Systems for Video Technology* 28.5 (2018), 1212–1231.

[210] Sarafianos, N.; Boteanu, B.; Ionescu, B.; Kakadiaris, I. A.: 3D Human pose estimation: A review of the literature and analysis of covariates. In: *Computer Vision and Image Understanding* 152.1 (2016), 1–20.

[211] Trumble, M.; Gilbert, A.; Malleson, C.; Hilton, A.; Collomosse, J.: Total capture: 3D human pose estimation fusing video and inertial sensors. In: *28th British Machine Vision Conference (BMVC)*. BMVA. 2017, 1–13.

[212] Wong, C.; Zhang, Z.-Q.; Lo, B.; Yang, G.-Z.: Wearable sensing for solid biomechanics: A review. In: *IEEE Sensors Journal* 15.5 (2015), 2747–2760.

[213] Peterson Silveira, R.; Stergiou, P.; Carpes, F. P.; Castro, F. A. d. S.; Katz, L.; Stefanyshyn, D. J.: Validity of a portable force platform for assessing biomechanical parameters in three different tasks. In: *Sports Biomechanics* 16.2 (2017), 177–186.

[214] Tan, A. M.; Fuss, F. K.; Weizman, Y.; Troynikov, O.: Development of a smart insole for medical and sports purposes. In: *Procedia Engineering* 112.1 (2015), 152–156.

[215] Zhou, B.; Koerger, H.; Wirth, M.; Zwick, C.; Martindale, C.; Cruz, H.; Eskofier, B.; Lukowicz, P.: Smart soccer shoe: monitoring foot-ball interaction with shoe integrated textile pressure sensor matrix. In: *20th International Symposium on Wearable Computers (ISWC)*. ACM. 2016, 64–71.

[216] Dallinga, J.; Benjaminse, A.; Gokeler, A.; Cortes, N.; Otten, E.; Lemmink, K.: Innovative video feedback on jump landing improves landing technique in males. In: *International Journal of Sports Medicine* 38.2 (2017), 150–158.

[217] Lopes, T. J. A.; Simic, M.; Myer, G. D.; Ford, K. R.; Hewett, T. E.; Pappas, E.: The effects of injury prevention programs on the biomechanics of landing tasks: A systematic review with meta-analysis. In: *The American Journal of Sports Medicine* 46.6 (2018), 1492–1499.

[218] LeCun, Y.; Bengio, Y.; Hinton, G.: Deep learning. In: *Nature* 521.7553 (2015), 436–444.

[219] Jordan, M. I.; Mitchell, T. M.: Machine learning: Trends, perspectives, and prospects. In: *Science* 349.6245 (2015), 255–260.

[220] Brock, H.; Ohgi, Y.; Lee, J.: Learning to judge like a human: Convolutional networks for classification of ski jumping errors. In: *21st International Symposium on Wearable Computers (ISWC)*. ACM. 2017, 106–113.

[221] Batuev, M.; Robinson, L.: What influences organisational evolution of modern sport: The case of skateboarding. In: *Sport, Business and Management: An International Journal* 8.5 (2018), 492–510.

[222] IOC: IOC approves five new sports for Olympic Games Tokyo 2020. [Online]. https://www.olympic.org/news/ioc-approves-five-new-sports-for-olympic-games-tokyo-2020/ [Accessed: August 31, 2019]. 2016.

[223] Skispringen.com: Sensor-Technik soll das Skispringen revolutionieren. [Online]. https://www.skispringen.com/sensor-technik-soll-das-skispringen-revolutionieren/ [Accessed: August 31, 2019]. 2018.

[224] IOC: Nordic Combined - Individual Gundersen Normal Hill/10km - Ski Jumping - PyeongChang 2018 Winter Olympic Games. [Online]. https://www.olympic.org/videos/nordic-combined-individual-gundersen-normal-hill-10km-ski-jumping-pyeongchang-2018-winter-olympic-games/ [Accessed: August 31, 2019]. 2018.

[225] IEEE Spectrum: Wearable device tracks tricks in freestyle snowboarding. [Online]. https://spectrum.ieee.org/the-human-os/biomedical/devices/wearable-device-tracks-tricks-in-freestyle-snowboarding/ [Accessed: August 31, 2019]. 2016.

[226] Real Federación Española de Deportes de Invierno (RFEDI): Programa de alta tecnología para los riders españoles de snowboard que participarán en el big air SN2017. [Online]. http://rfedi.es/programa-alta-tecnologia-los-riders-espanoles-snowboard-participaran-big-air-sn2017/ [Accessed: August 31, 2019]. 2017.

Own publications referring to this work

[P1] Groh, B. H.; Cibis, T.; Schill, R. O.; Eskofier, B. M.: IMU-based pose determination of scuba divers' bodies and shanks. In: *12th International Conference on Wearable and Implantable Body Sensor Networks (BSN)*. IEEE. 2015, 1–6.

[P2] Groh, B. H.; Reinfelder, S. J.; Streicher, M. N.; Taraben, A.; Eskofier, B. M.: Movement prediction in rowing using a dynamic time warping based stroke detection. In: *9th International Conference on Intelligent Sensors, Sensor Networks and Information Processing (ISSNIP)*. IEEE. 2014, 1–6.

[P3] Groh, B. H.; Schottenhamml, J.; Eskofier, B. M.; Ami, D.: Unobtrusive estimation of in-stroke boat rotation in rowing using wearable sensors. In: *12th International Symposium on Computer Science in Sport (IACSS)*. Springer. 2019, 114–122.

[P4] Groh, B. H.; Weeger, N.; Warschun, F.; Eskofier, B. M.: Simplified orientation determination in ski jumping using inertial sensor data. In: *DGON Inertial Sensors and Systems Symposium (ISS)*. IEEE. 2014, 1–11.

[P5] Groh, B. H.; Warschun, F.; Deininger, M.; Kautz, T.; Martindale, C.; Eskofier, B. M.: Automated ski velocity and jump length determination in ski jumping based on unobtrusive and wearable sensors. In: *Proceedings of the ACM on Interactive, Mobile, Wearable and Ubiquitous Technologies (IMWUT)* 1.3 (2017), 53:1–53:17.

[P6] Groh, B. H.; Fleckenstein, M.; Eskofier, B. M.: Wearable trick classification in freestyle snowboarding. In: *13th International Conference on Wearable and Implantable Body Sensor Networks (BSN)*. IEEE. 2016, 89–93.

[P7] Groh, B. H.; Kautz, T.; Schuldhaus, D.; Eskofier, B. M.: IMU-based trick classification in skateboarding. In: *KDD Workshop on Large-Scale Sports Analytics*. ACM. 2015, 1–4.

[P8] Groh, B. H.; Flaschka, J.; Wirth, M.; Kautz, T.; Fleckenstein, M.; Eskofier, B. M.: Wearable real-time skateboard trick visualization and its community perception. In: *IEEE Computer Graphics and Applications* 36.5 (2016), 12–18.

[P9] Groh, B. H.; Fleckenstein, M.; Kautz, T.; Eskofier, B. M.: Classification and visualization of skateboard tricks using wearable sensors. In: *Pervasive and Mobile Computing* 40.1 (2017), 42–55.

Sports analytics research has major impact on the development of innovative training methods and the broadcast of sports events. This dissertation provides algorithms for both kinematic analysis and performance interpretation based on unobtrusively obtained measurements from wearable sensors. Its main focus is set on the processing of 3D-orientation features and the exploration of their potential for sports analytics. The proposed algorithms are described and evaluated in five exemplary sports. In scuba diving, rowing and ski jumping, the 3D-orientation of the body/boat/skis is determined and further processed to analyze and visualize the motion behavior. In snowboarding and skateboarding, the board orientation is calculated and processed for motion visualization and machine learning. Board sport tricks are automatically detected and subsequently classified for trick category and type. The methods of this work were already partially applied for TV broadcast of international competitions (e.g., Olympics 2018). Additionally, they can support sports science research for establishing thorough investigations and innovative training methods.

ISBN 978-3-96147-485-1

FAU UNIVERSITY PRESS 2021